CHAPTER 4
EXPERIMENTAL DESIGN

This chapter concentrates on procedures of SYSID, where, a fully instrumented natural gas test facility was designed and constructed. The test rig is designed that allows actual data of mass flowrate could be collected from actual coriolis flowmeter manufactured by Micro Motion based on three pressures of CNG filling banks: low pressure bank, medium pressure bank and high pressure bank. From these experimental data, the significant algorithm in this research would be clarified which is the inferential coriolis design.

4.1 Introduction

In general terms, an identification experiment is performed by exciting the Micro Motion coriolis flowmeter (using some sort of step signal such as valve opening) and observing its mass flowrate output over a time interval. These signals are recorded in a mass storage device such as FieldPoint for subsequent 'information processing'. The first step in parametric estimation method is to determine an appropriate discrete model of the coriolis (typically a linear difference equation) based on three approaches: non-recursive, recursive and state-space. As a second step, some statistically based method is used to estimate the unknown parameters of the coriolis model (the coefficients of the difference equation) by using three analyses: optimal order, prediction error and singular values. In practice, the estimation for structures and parameters of coriolis model are often done iteratively which cover three steps: determining coefficient, stability analysis and validation of power series expansion. This means that a tentative structure is chosen and the corresponding parameters are estimated. The coriolis model obtained is then tested to see whether it is an appropriate representation of the actual coriolis. If this is not the case, some more complex order of model structure would be considered i.e., a new structure and coefficient would be estimated and validated, until the estimated model corresponds to the actual coriolis. The SYSID procedure could be summarized as Figure 4.1.

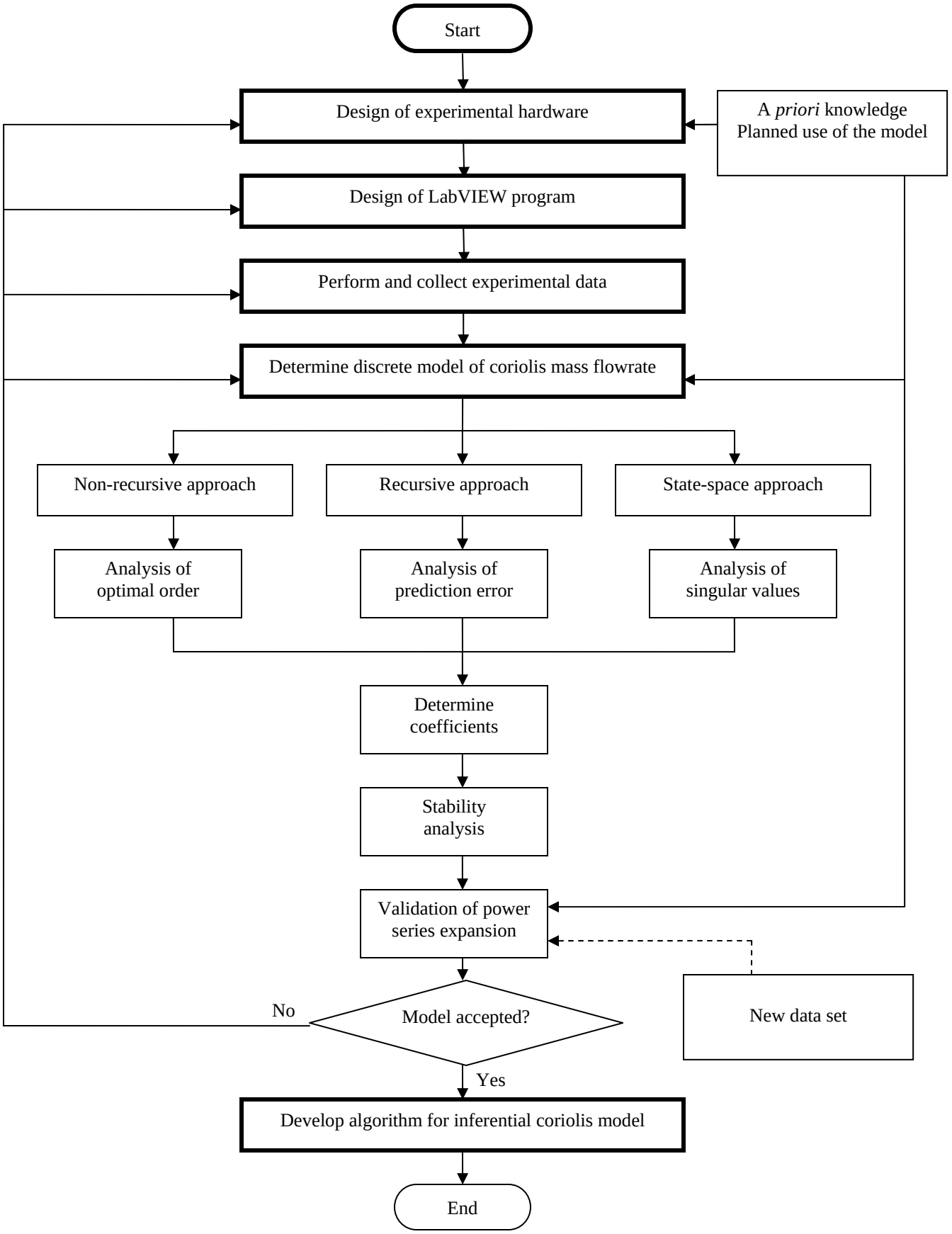

Figure 4.1: Flow chart of SYSID procedures

4.2 Design of experimental hardware

The following section discusses the first steps of SYSID methodology i.e., design of experimental hardware. Figure 4.2 shows the actual CNG test rig that has been designed for CNG metering analysis and refueling control system purposes. There are three main sections such as natural gas test rig, data acquisition & controller system using FieldPoint and graphical programming using LabVIEW, in which, the test rig itself consists of five sub systems such as cascaded storage system, flow metering system, receiver system, recycle system and sequencing system. These main components that are required in the test rig will be clearly explained to facilitate research work.

Figure 4.2: Natural gas test rig

4.2.1 Cascaded storage system

Figure 4.3 shows a three stage cascade storage system comprising of nine 5000 psig rated cylinders arranged in a 4-3-2 arrangement representing the low, medium and high pressure configurations. Each cylinder has a capacity of 55 liters at 5000 psig rated pressure. The cylinder cascade banks were assembled with motorized ball valves which were remotely activated during the testing from the laboratory computer control system.

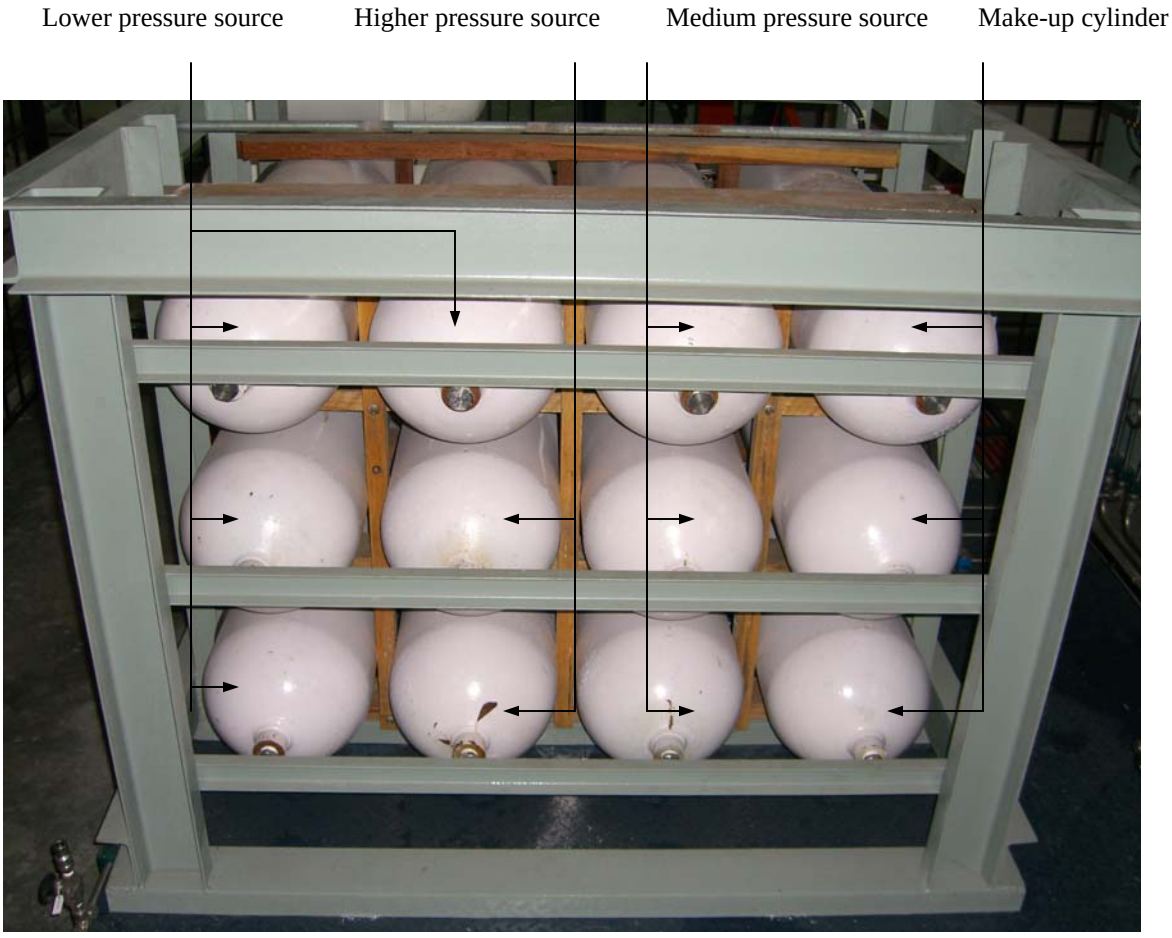

Figure 4.3: Cascaded storage system

4.2.2 Flow metering system

Figure 4.4 shows a coriolis flowmeter installed with three types of volumetric flowmeter: turbine, vortex and differential flowmeter to measure the flow of gas in the natural gas cylinder during the relatively high flow, rapid charging tests. The purpose is to compare coriolis metering performance and analyze the various types of natural gas flowmeters.

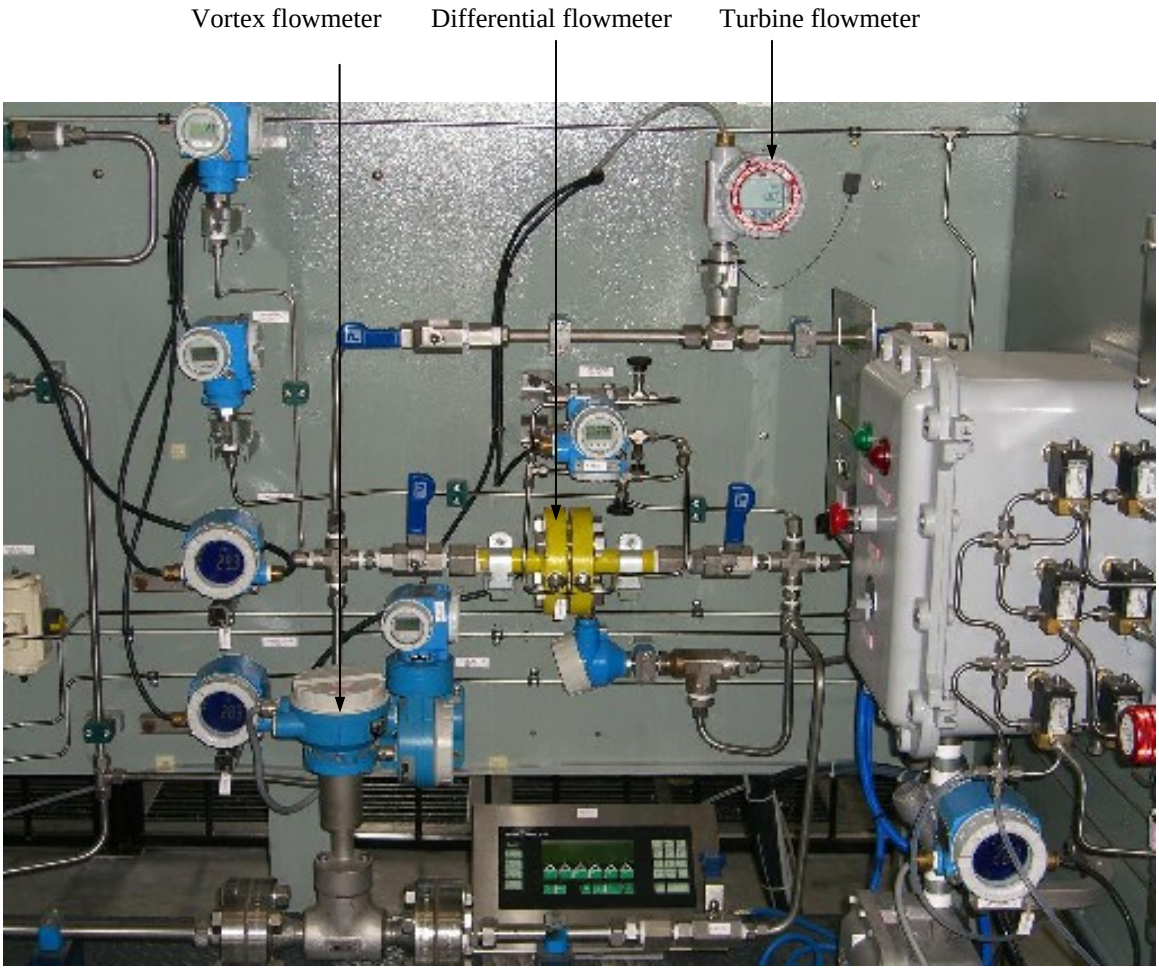

Figure 4.4: Flow metering system

4.2.3 Receiver system

Figure 4.5 shows a receiver system that replicates the actual car storage tank or receiver tank. It has one 55 liters cylinder tank at the 5000 psig rated pressure equipped with an embedded pressure sensor and a load cell to measure the actual filling weight.

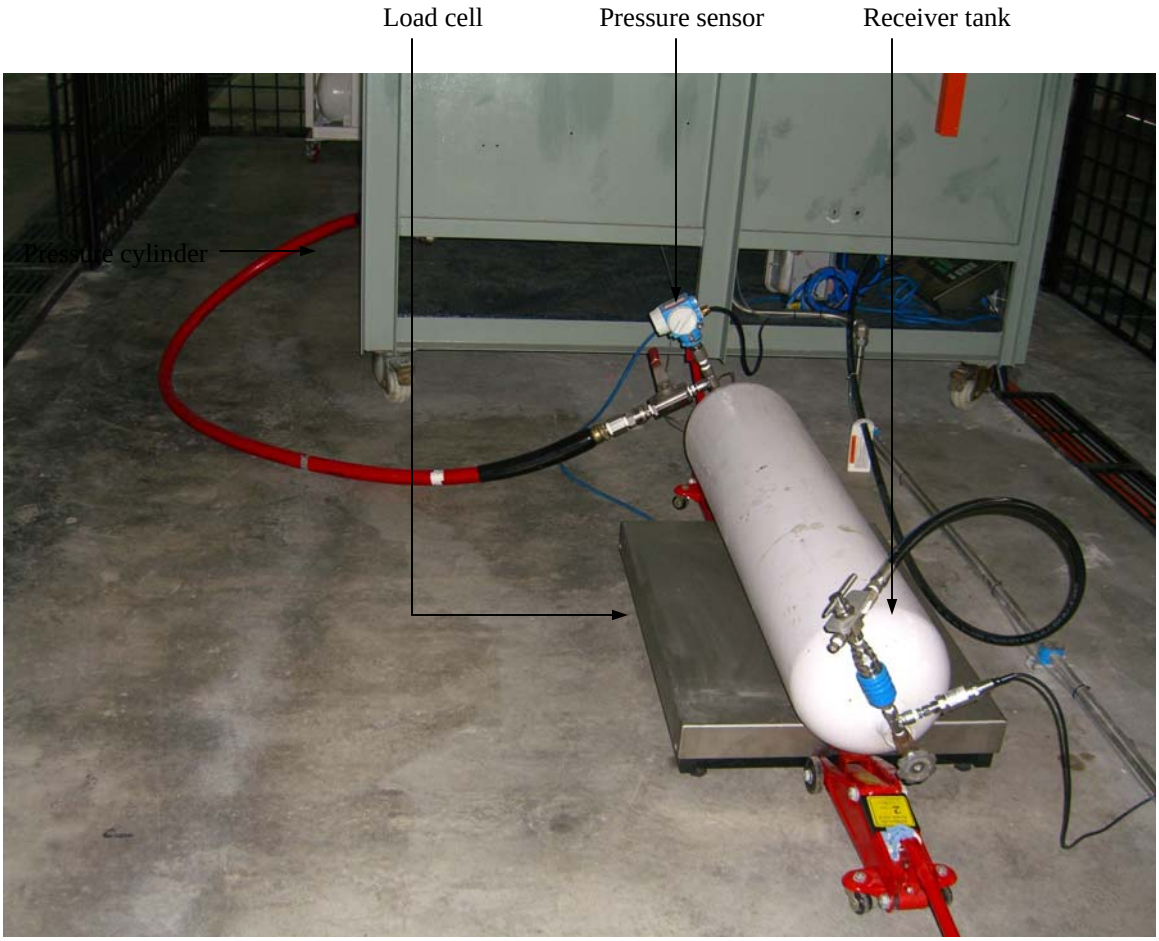

Figure 4.5: Receiver system

4.2.4 Recycle system

Figure 4.6 shows a recycle system consists of a recycling piping and two compressors which are used to recover and recycle the natural gas from the receiver to the cascaded storage system. Since a small amount of natural gas from the receiver system is expected to be lost during each experiment, the system is equipped with three 55 liters 'make-up' cylinders, see Figure 4.3, to compensate for the losses.

Figure 4.6: Recycle system

4.2.5 Sequencing system

The sequencing system sets the low, medium and high pressure at cascaded storage system using ball valves. A ball valve is a valve that opens by turning a handle attached to a ball inside the valve. The ball has a hole, through the middle, thus when the hole is in line with both ends of the valve, the gas flow will take place. When the valve is closed, the hole is perpendicular to the ends of the valve, and the gas flow is blocked. If the natural gas at the cascaded storage system has reached the set pressure, the balance is restored in the temporary cylinders. These arrangements are shown in Figure 4.7.

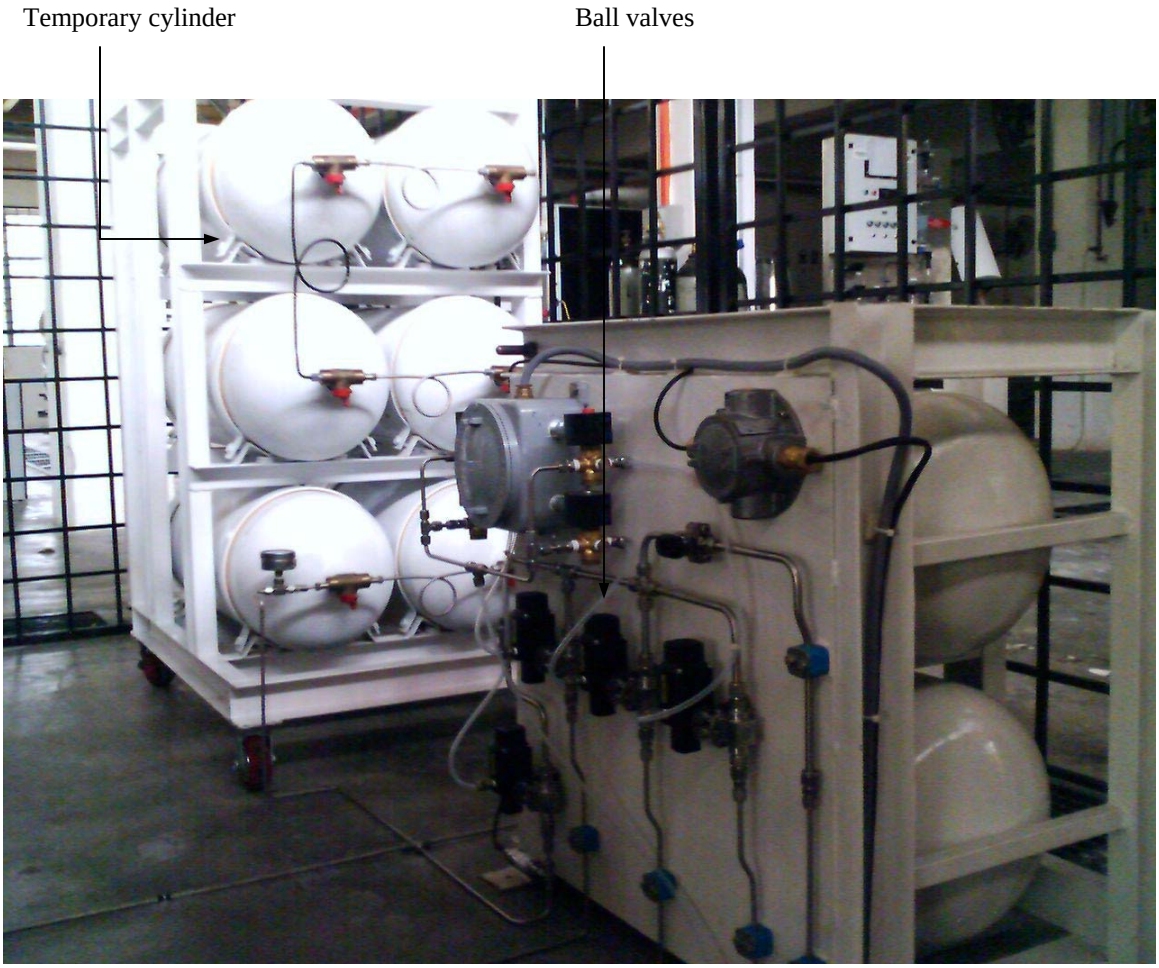

Figure 4.7: Sequencing system

4.2.6 DAQ & Control System

The data acquisition and control system for the test rig is designed using a hardware known as FieldPoint manufactured by National Instrument [249]. All the signals data sent by the sensors and other instrumentations in the test rig are monitored and collected remotely from a computer located in a control room via an ethernet connection to the FieldPoint. The control system to monitor and control the test rig has been programmed using software known as LabVIEW [249]. The program also has been embedded in the FieldPoint for reliable distribution and stand-alone deployment. As shown by Figure 4.8, there are seven modules used to monitor and control the test rig such as controller module, thermocouple module, counter module, digital input module, relay module, analog input module and analog output module.

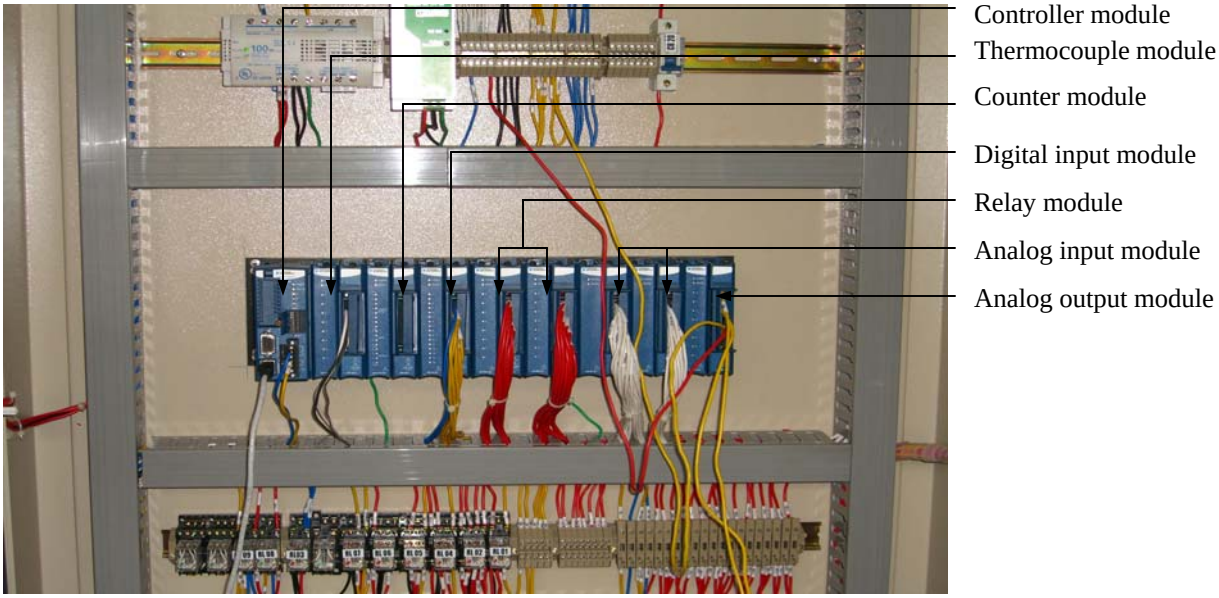

Figure 4.8: FieldPoint system

To simplify each module installation to the computer, FieldPoint uses automatically plug-and-play mechanism to detect and identify via ethernet and TCP/IP connection. Further references such as technical specifications, loop diagrams, operating instructions and safety guidelines for each module could be reviewed from [249]. Also, Figure 4.9 in following section shows the single line diagram to describe connections from sensors to channels of input and output (I/O) of the FieldPoint modules.

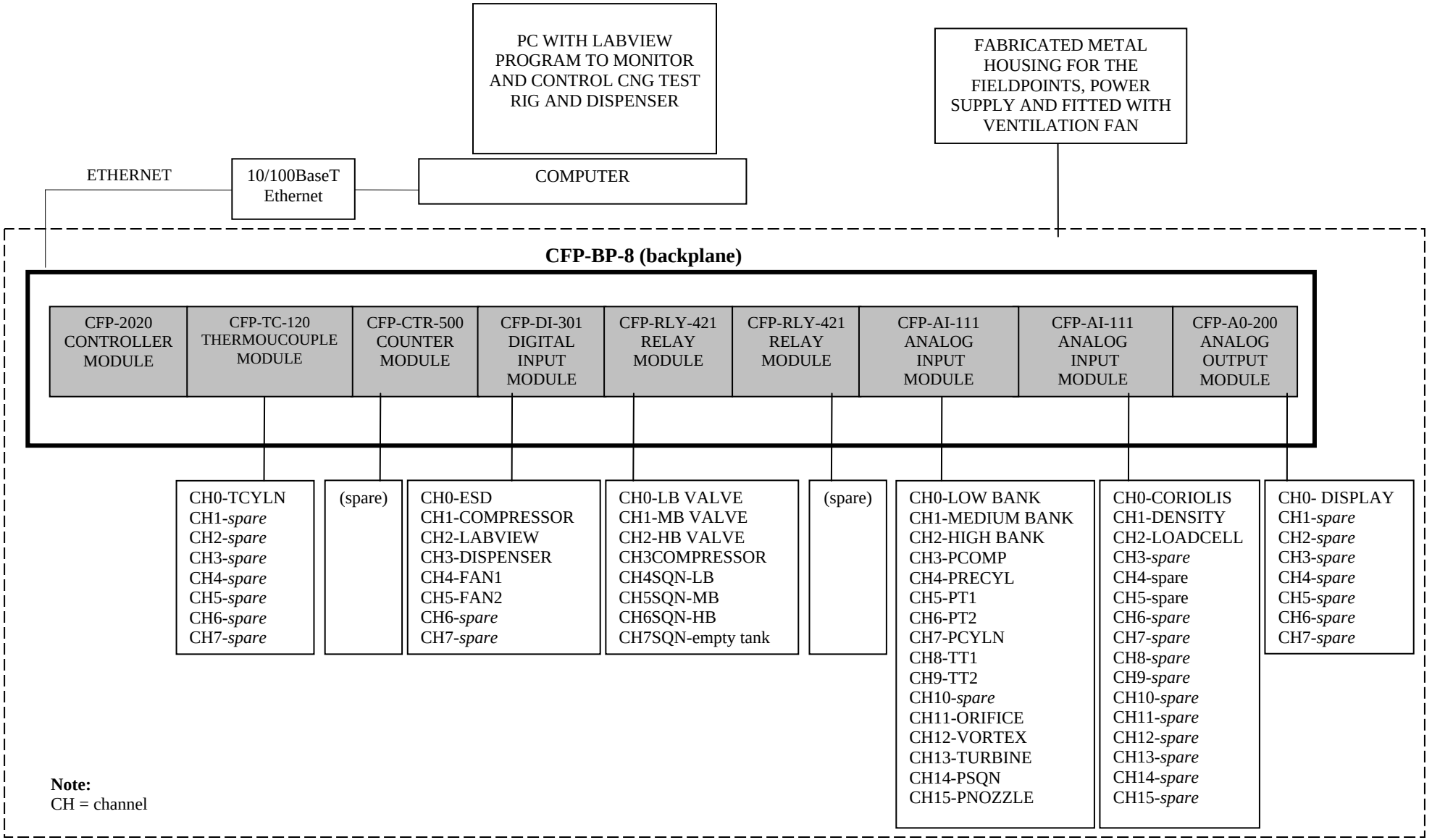

Figure 4.9: Single Line Diagram for natural gas test rig using FieldPoint

4.3 Design of LabVIEW program

The following section discusses the second steps of SYSID procedure i.e., design of LabVIEW program. Figure 4.3-Figure 4.7 in previous section has shown five sub systems for the test rig such as cascaded storage system, flow metering system, receiver system, recycle system and sequencing system, whilst Figure 4.10 in the following section shows LabVIEW front panel to monitor and control the natural gas test rig systems.

Since the test rig comprises of five sub systems, the program for LabVIEW front panel also would comprise with five other sub programs such as cascaded storage sub program, flow metering sub program, receiver sub program, recycle sub program and sequencing sub program. The following section provides detail descriptions for each of the sub programs.

4.3.1 Cascaded storage subprogram

As shown by Figure 4.10, the low, medium and high pressure configuration in the cascaded storage system is indicated by ‘LOW BANK’, ‘MEDIUM BANK’ and ‘HIGH BANK’, respectively. The flow of natural gas to the receiver system is activated by ‘LB’, ‘MB’ and ‘HB’ toggle switch buttons depending on the requirements. The indicators ‘LB VALVE’, ‘MB VALVE’ and ‘HB VALVE’ would change to green color indicating the respective valve is activated to allow flow. Please refer Figure 4.11 for LabVIEW program of cascaded storage system.

4.3.2 Flow metering subprogram

Based on Figure 4.10, the flowrate produced by flowmeters in the flow metering system is specified by ‘TURBINE’, ‘ORIFICE’, ‘VORTEX’ and ‘CORIOLIS’. The density from the actual coriolis flowmeter is shown by ‘DENSITY’, whilst pressure and temperature before and after the flow metering system are indicated by ‘PT1’, ‘TT1’ and ‘PT2’, ‘TT2’, respectively. Please refer Figure 4.12 for LabVIEW program of flow metering system.

4.3.3 Receiver subprogram

From Figure 4.10, the actual pressure, temperature, pressure inside the nozzle and actual filling weight of the receiver system are indicated by ‘PCYLN’, ‘TCLYN’, ‘PNOZZLE’ and ‘LOAD CELL’, respectively.

Whilst, values set at ‘OFFSET-PNOZZLE’ and ‘OFFSET-LOADCELL’ are used to compensate with the actual values of pressure inside nozzle and the filling weight of receiver cylinder, respectively. Please refer Figure 4.12 for LabVIEW program of receiver system.

4.3.4 Recycle subprogram

As shown by Figure 4.10, the compressors in the recycle system are specified by ‘FMQ-8-36’ and ‘FMQ-2-36’ which is activated by ‘COMPRESSOR’ toggle switch button, whilst the pressure during recycling process and pressure inside the ‘make-up’ cylinders is shown by ‘PCOMP’ and ‘PRECYL’, respectively. Notably, the recycling process would stop if the pressure inside the receiver tank reaches the ‘PCYLN SETPOINT’ value. Please refer Figure 4.13 for LabVIEW program of recycle system.

4.3.5 Sequencing subprogram

Based on Figure 4.10, the ‘temporary’ cylinders in the sequencing system are specified by ‘PSQN’. It is activated by ball valve represented by ‘SQN-EMPTY TANK’ toggle switch button. The toggle switch button i.e., ‘MODE’ would determine two types of recycling processes i.e., ‘MANUAL’ and ‘AUTO’ recycling.

If ‘MANUAL’ is chosen, pressure values at ‘LOW BANK’, ‘MEDIUM BANK’ and ‘HIGH BANK’ would be set manually using ‘SQN-LB’, ‘SQN-MB’ and ‘SQN-HB’ toggle switch buttons, respectively. Whilst, if ‘AUTO’ is chosen, pressure at ‘LOW BANK’, ‘MEDIUM BANK’ and ‘HIGH BANK’ would be activated automatically using reference values from ‘Low Bank Setpoint’, ‘Medium Bank Setpoint’ and ‘High Bank Setpoint’, respectively. Please refer Figure 4.14 for LabVIEW program of sequencing system.

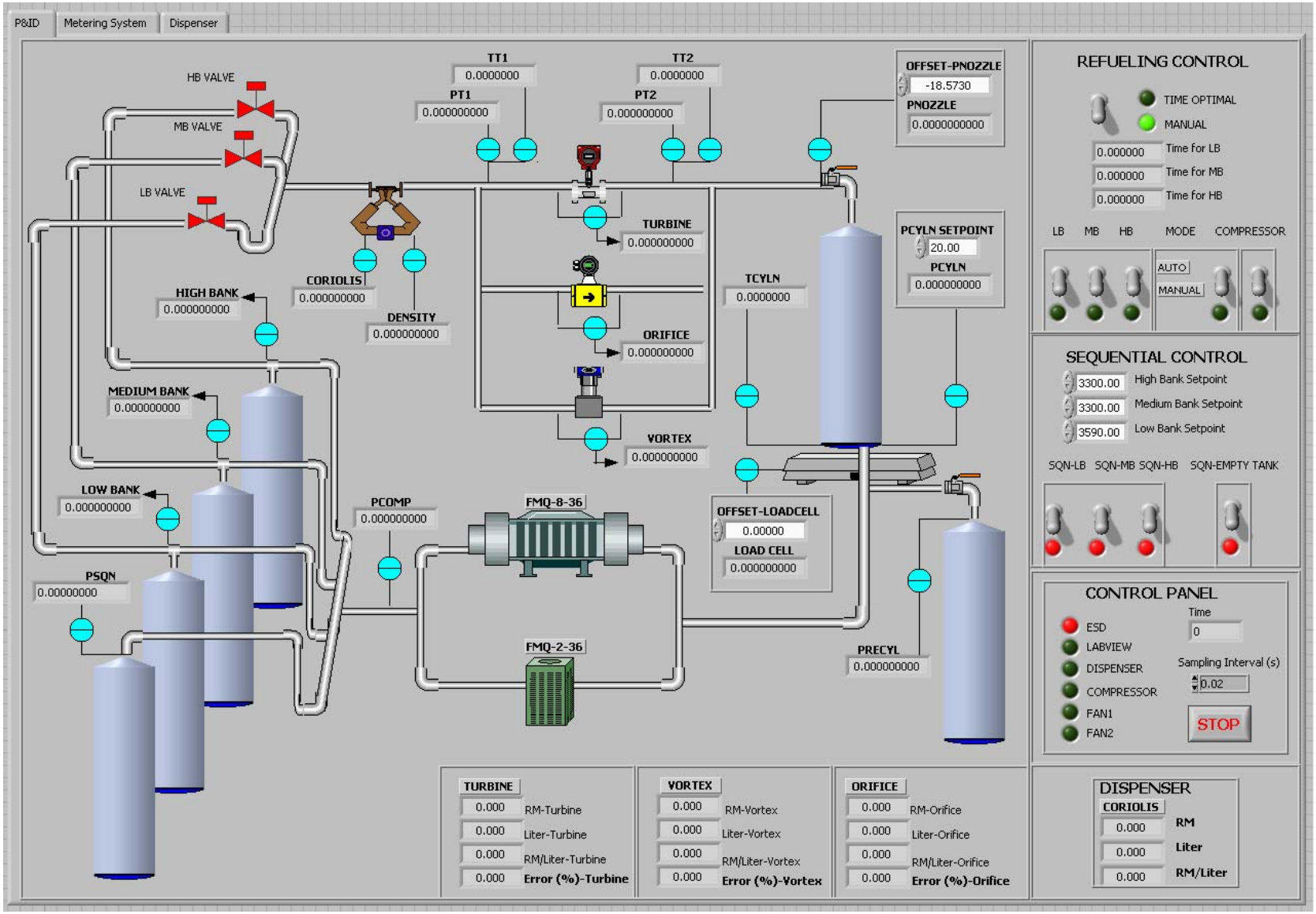

Figure 4.10: LabVIEW front panel to monitor and control the test rig

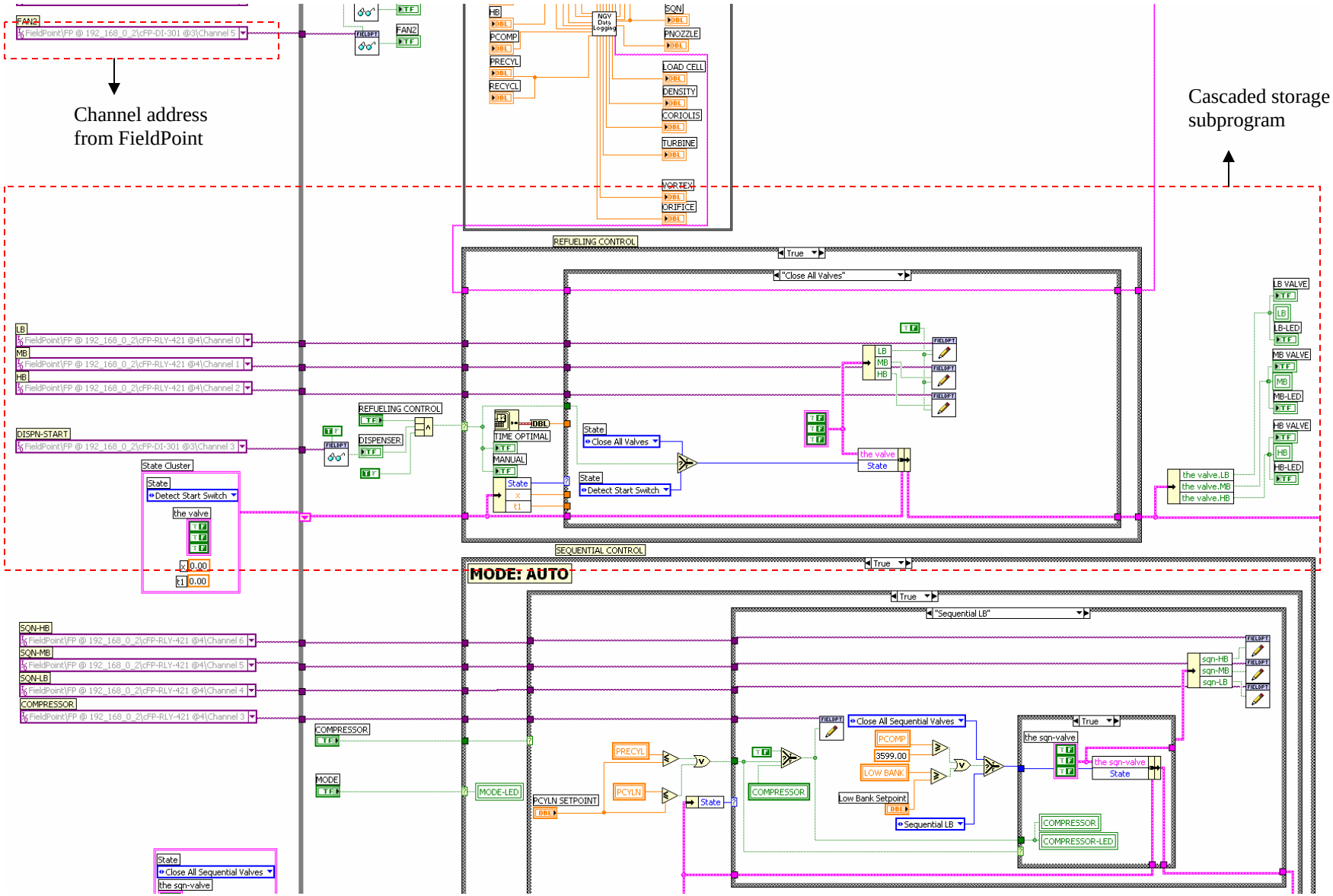

Figure 4.11: LabVIEW sub program for cascaded storage system

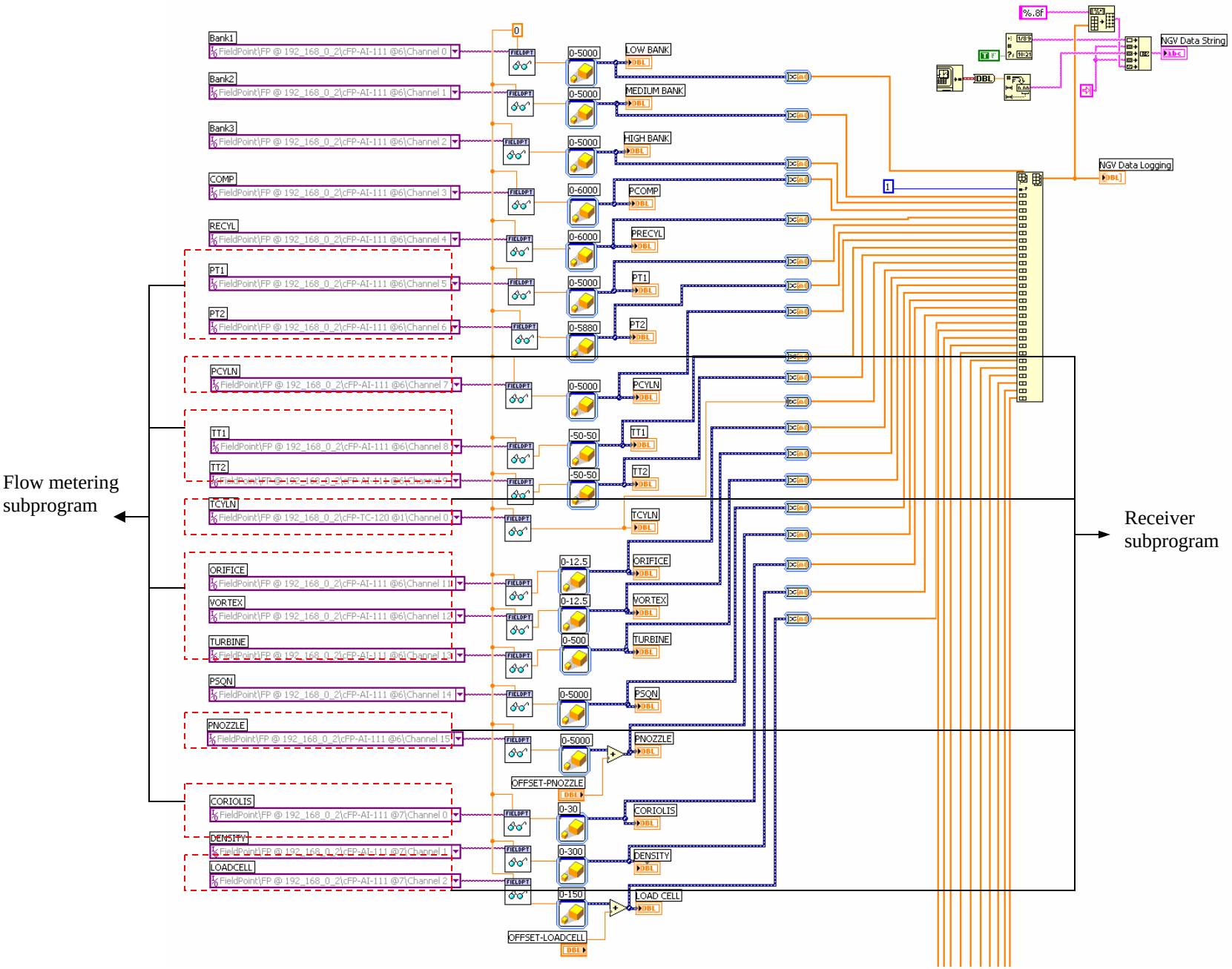

Figure 4.12: LabVIEW sub program for flow metering and receiver system

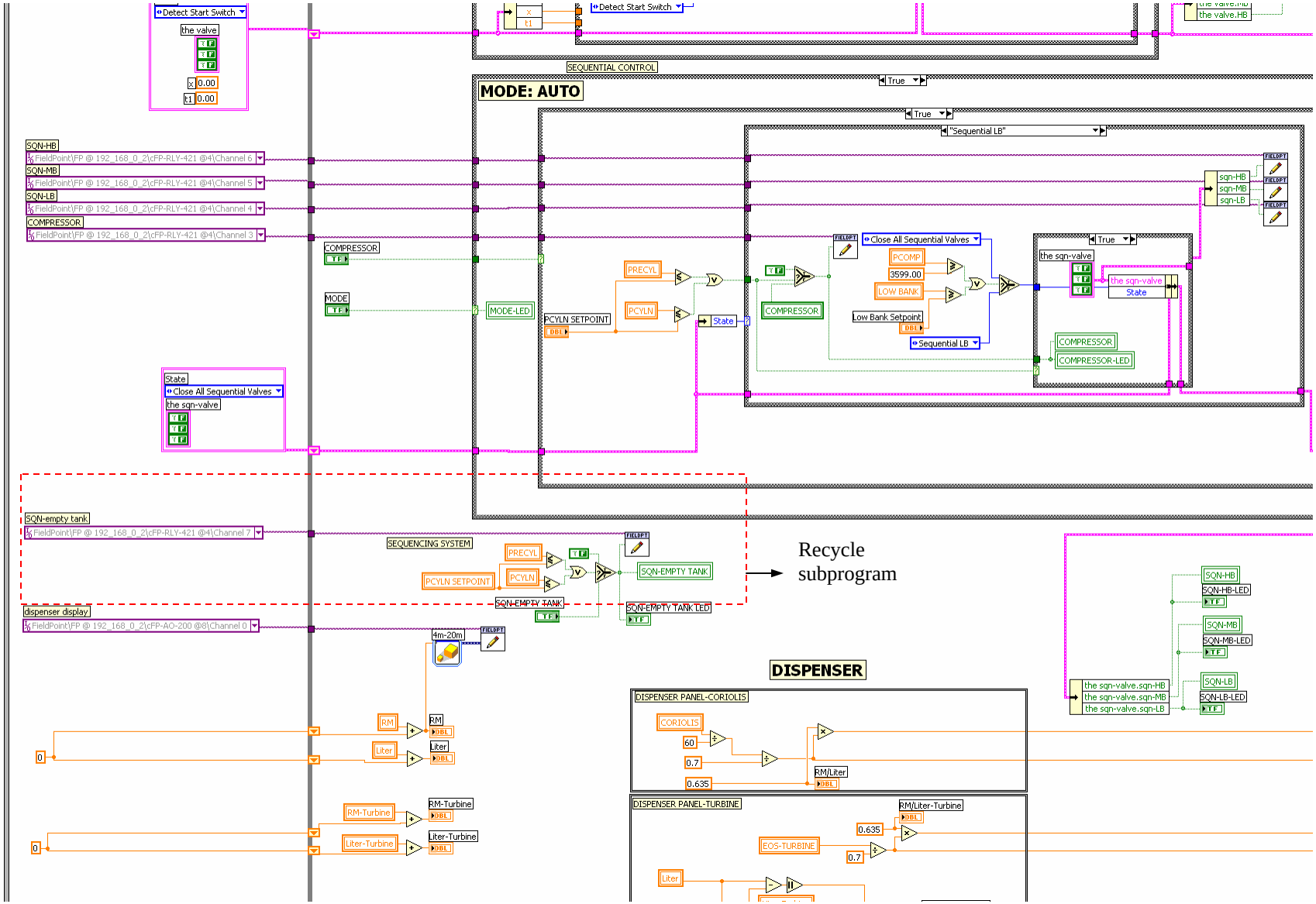

Figure 4.13: LabVIEW sub program for recycle system

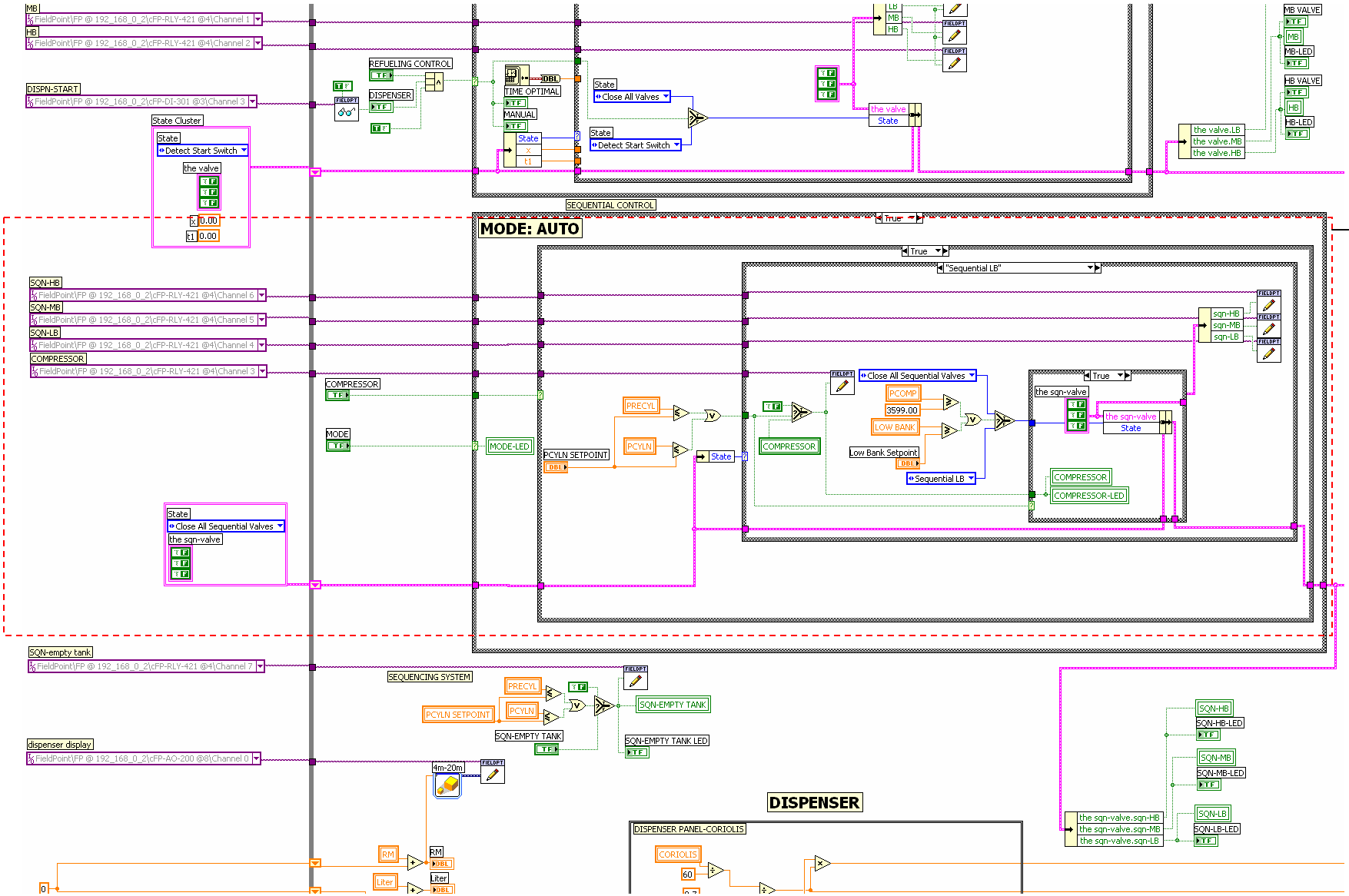

Figure 4.14: LabVIEW sub program for sequencing system

4.4 Perform and collect experimental data

Sections 4.1 to 4.3 have been to describing three main hardwares that are required for initiating the SYSID work: natural gas test rig, data acquisition & control system (DAQ) using FieldPoint and LabVIEW programs, respectively. The following section discusses the third steps of SYSID methodology i.e., perform and collect experimental using refueling and recycling process of the test rig.

4.4.1 Process flow of natural gas test rig

The P&ID diagram shown in Figure 4.15 comprises of storage cylinders horizontally stacked in metal frame, panel mounted dispenser, slow-filled compressor, gas piping, electrical control and data acquisition system. It has been equipped with adequate instrumentation system for purpose of analyzing flow measurement of natural gas and sufficient capacity to weigh the NGV cylinder and gas. As can be observed from the figure, materials or equipments are presented by tag numbers. These tag numbers will be defined individually in the process explanation and can be referred from Table 4.1. There are 4 types of flowmeters installed in the dispensing system which are coriolis **B310**, turbine **B320**, differential pressure **B330** and vortex **B340** with coriolis flowmeter acting as the reference flowmeter. At any time, only coriolis and any one of the three flowmeters could be used. Data from all flowmeters are electronically retrieved and stored in a data acquisition system **YC01**. The recycle system is to recover and recycle the natural gas from car storage into the supply storage system. The system consists of two timed-filled compressors **B470** and **B480**. It is expected a small amount of natural gas from car storage will be lost during each experiment trial. Thus, the system is equipped with make-up cylinders **B270** to compensate for the losses. The supply storage system consists of nine 55 liters cylindrical tanks altogether with maximum pressure at 3600 psig (at 70 °C) and they are all placed in one rack. These tanks are sub-divided into three different bank systems, low bank (LB) **B280,** medium bank (MB) **B290** and high bank (HB) **B300**. LB, MB and HB systems have 4, 3 and 2 cylindrical tanks respectively. All of these tanks have the same pressure of 3600 psig when they are fully occupied by natural gas. What differentiate these tanks are their functions and number of tanks. From the P&ID diagram, the refueling and recycling process is described in following section.

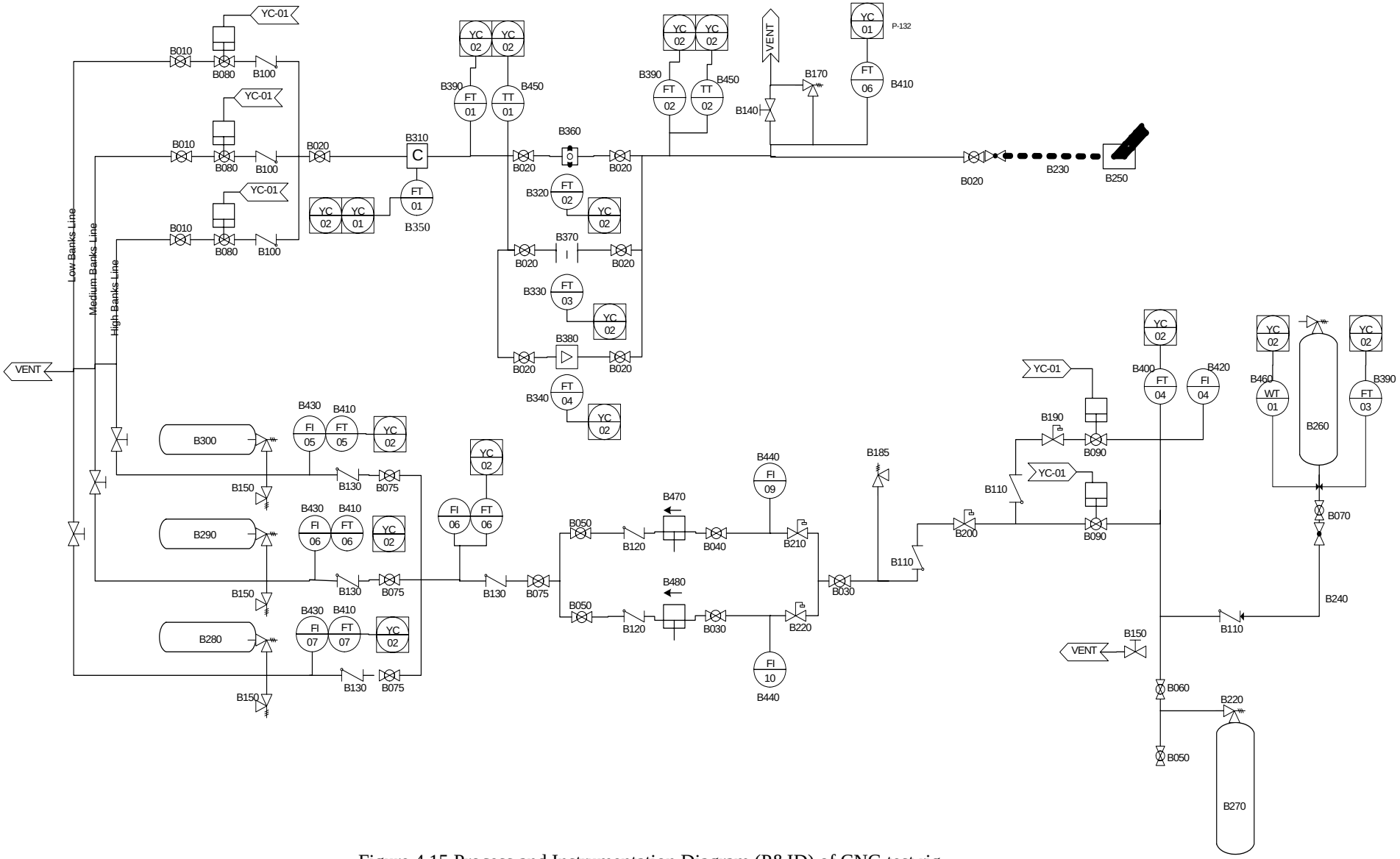

Figure 4.15 Process and Instrumentation Diagram (P&ID) of CNG test rig

Table 4.1: Tag numbers of natural gas test rig

ITEM	DESCRIPTION	QUANTITY	MATERIAL/SPECIFICATION
B010	VALVE, BALL	3	PARKER P/N: HPB6S8A
B020	VALVE, BALL	8	PARKER P/N: HPB6S8FF
B030	VALVE, BALL	2	KITZ BRASS 150PSIG MAWP
B040	VALVE, BALL	1	SWAGELOK P/N: SS-63TS8
B050	VALVE, BALL	3	SWAGELOK P/N: SS-33VF4
B060	VALVE, BALL	1	SWAGELOK P/N: SS-83KS8
B070	VALVE, BALL	1	OASIS P/N: BV506-NT
B075	VALVE, BALL	4	PARKER P/N: 4A-B2LJ2-SSP
B080	VALVE, BALL PNEUMATIC	3	PARKER P/N: 8A-B8LJ2-SSP-62AC-3
B090	VALVE, BALL PNEUMATIC	2	PARKER P/N: 8F-B8LJ2-SSP-62AC-3
B100	VALVE, CHECK	3	PARKER P/N: 8A-C8L-1-SS
B110	VALVE, CHECK	3	SWAGELOK P/N: SS-CHS16-1
B120	VALVE, CHECK	2	SWAGELOK P/N: SS-CHS4-1
B130	VALVE, CHECK	4	PARKER P/N: 4A-C4L-1-SS
B140	VALVE, NEEDLE	1	AGCO-P/N: H5RIC-22
B150	VALVE, NEEDLE	1	SWAGELOK P/N: SS-1RS4
B160	VALVE, NEEDLE	3	PARKER P/N: 4A-V4LN-SS
B170	VALVE, RELIEF	1	SWAGELOK P/N: SS-4R3A1 SET @ 3750PSIG
B180	VALVE, RELIEF	3	SWAGELOK P/N: SS-4R3A SET @ 3950PSIG
B185	VALVE, RELIEF	1	SWAGELOK P/N: SS-RL4M8F8 SET @ 100PSIG
B190	VALVE, REGULATOR	1	JORDAN P/N: JHR Cv=0.6 SET @ 150PSIG
B200	VALVE, REGULATOR	1	JORDAN P/N: JHR Cv=0.6 SET @ 30 PSIG
B210	VALVE, REGULATOR	1	JORDAN P/N: MARK608 5/16” OR SET @ 7” H2O
B220	VALVE, REGULATOR	1	JORDAN P/N: MARK608 5/16” OR SET @ 35” H2O
B230	HOSE, FLEXIBLE	1	SWAGELOK P/N: SS-NGS6-NN-120X
B240	HOSE, FLEXIBLE	1	PARKER P/N: 5CNG0101-16-16-16-120
B250	NOZZLE	1	SWAGELOK P/N: SS-83XKF4
B260	CYLINDER, NGV	1	EKC 1x55LWC 3600PSIG
B270	CYLINDER, NGV	1	EKC 3x55LWC 3600PSIG
B280	CYLINDER, NGV	1	EKC 4x55LWC 3600PSIG LOW BANK
B290	CYLINDER, NGV	1	EKC 3x55LWC 3600PSIG MEDIUM BANK
B300	CYLINDER, NGV	1	EKC 2x55LWC 3600PSIG HIGH BANK
B310	FLOW, SENSOR CORIOLIS	1	MICROMOTION P/N: CNG050S239NCAZEZZZ
B320	FLOW, SENSOR TURBINE	1	HOFFER P/N: 3/ 4x3 /4-25-CB-1RPR-MS-CE
B330	FLOW, SENSOR ORIFICE	1	ENDRESS + HAUSER P/N: DN25 PN250
B340	FLOW, SENSOR VORTEX	1	ENDRESS + HAUSER P/N: 70HS25-D0D20B100
B350	FLOW, TRANSMITTER CORIOLIS	1	MICROMOTION P/N: 2700I11BBFEZZZ
B360	FLOW, TRANSMITTER TURBINE	1	HOFFER P/N: HIT2A-3-B-C-X-FX
B370	FLOW, TRANSMITTER ORIFICE	1	ENDRESS + HAUSER P/N: PMD235-MB588EM3C
B380	FLOW, TRANSMITTER VORTEX	1	ENDRESS + HAUSER P/N: 70HS25-D0D20B1B100
B390	PRESSURE, TRANSMITTER	3	ENDRESS + HAUSER P/N: PMP731-I33Z1M21X1
B400	PRESSURE, TRANSMITTER	2	MURPHY P/N: PXMS-6000
B410	PRESSURE, TRANSMITTER	5	MURPHY P/N: PXMS-5000
B420	PRESSURE, GAUGE	1	SWAGELOK
B430	PRESSURE, GAUGE	4	SWAGELOK
B440	PRESSURE, GAUGE	2	ASHCROFT 2-1/2” DIAL 0-60” H2O
B450	TEMPERATURE, TRANSMITTER	3	ENDRESS + HAUSER P/N: TMT162-E21231AAA
B460	LOAD CELL	1	METTLER TOLEDO EX APPROVED, 0-150KG
B470	COMPRESSOR, TIME FILLED	1	FUEL MAKER P/N: FMQ-2-36
B480	COMPRESSOR, TIME FILLED	1	FUEL MAKER P/N: FMQ-8-36
YC-01	DISPENSER REGISTER	1	KRAUS P/N: 09 N28AGUCGMS-D
YC-02	DATA ACQUISITION SYSTEM	1	NATIONAL INSTRUMENTS FIELDPOINT

4.4.2 Refueling and recycling process of natural gas test rig

To dispense natural gas to vehicle tank **B260**, nozzle **B250** is connected to receptacle that is located at the cylinder's neck. After that, the switch on display panel is turned to 'ON' position. Next, the nozzle valve **B250** is turned to 180 degree to 'ON' position. When the dispensing occurs, the **B240** hose should not be connected to the vehicle tank. The hose is only connected to **B070** and **B110** valves when recycling system is operated. The pressure, temperature and mass of natural gas are measured using transmitters **B390**, **B450**, and **B460** as shown in the diagram**.** These transmitters will then send input signal to the data acquisition system **YC01**. Figure 4.16 shows procedures for refueling natural gas using the test rig.

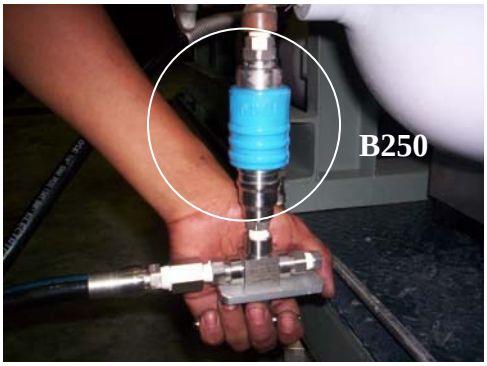

(a) Nozzle is pushed into receptacle located at cylinder neck. A 'click' sound should be heard.

(b) Switch located on display panel is turned to 'ON' position.

(c) Nozzle valve is turned 180 degree to 'ON' position. Gas will then flow to cylinder.

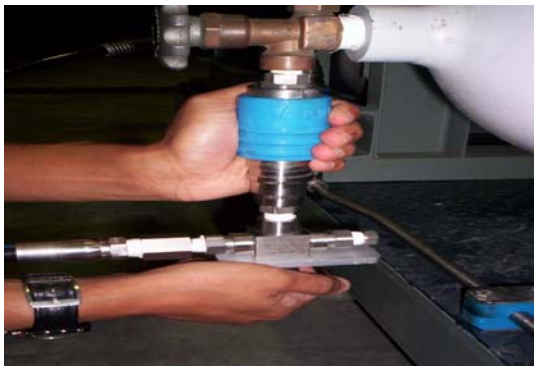

(d) When filling has completed, turn nozzle valve is turned back to 'OFF' position. Nozzle is uncoupled from receptacle by pulling blue collar.

Figure 4.16: Procedure of refueling CNG using test rig

After the refueling process, recycling system is used to empty the vehicle cylinder **B260** by transferring the gas to the storage cylinders **B280**, **B290** and **B300**. This is done via timed-filled compressor that has inlet and discharge pressure of 1.25 psig and 3600 psig respectively. Once empty, the compressor **B470** or **B480** will stop before the next sampling process could take place. To operate the recycling system, flexible hose **B240** is connected to temporary storage tank **B270**. One end of high pressure flexible hose is coupled to ball valve **B070** located at bottom neck of the vehicle tank **B260** while the other end is connected to inlet of check valve **B110**. After that, both valves **B070** and **B060** are turned to 'ON' position. Natural gas will flow to the temporary storage tanks **B270** before it is stored back to low bank **B280**, medium bank **B290** and high bank **B300** until all pressures approach the pressure value set at control system**YC01**. Figure 4.17 shows procedures for recycling the natural gas using the test rig.

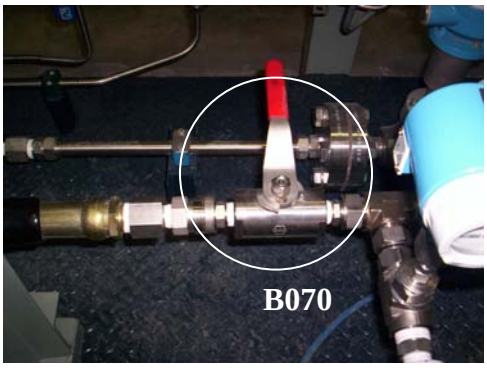

(a) One end of high pressure flexible hose is coupled to car cylinder bottom neck.

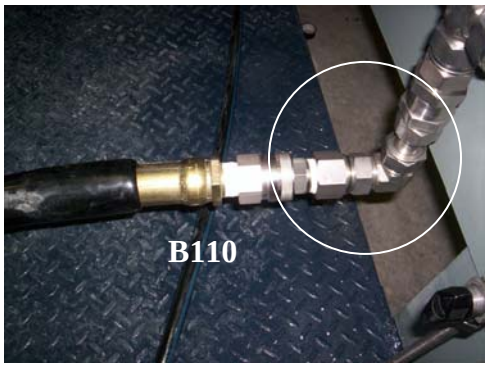

(b) The other end of flexible hose is coupled to inlet of regulator.

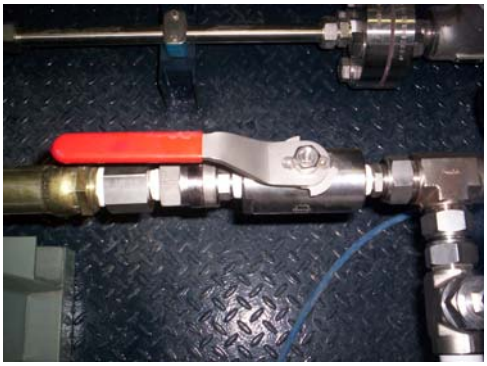

(c) The valve located at car cylinder bottom neck is turned to 'ON' position.

(d) The valve on regulator inlet is turned to 'ON' position. The gas would flow to recycling tank until the flow is stabilized.

Figure 4.17: Procedure of recycling CNG using test rig

4.4.3 Collecting experimental data from natural gas test rig

From the refueling and recycling process of CNG, the experimental procedures to collect the input and output data from actual coriolis would be described. As shown by Figure 4.15, the natural gas will flow through coriolis flowmeter **B310** and send the measured value to data acquisition system **YC01** using pressure transmitter **B350.** These filling processes are controlled by solenoid valves which get input signal from **YC01.**

Figure 4.18 in following section shows results of LabVIEW user interface application at the initial condition before collecting experimental data. Initially, low bank **B280**, medium bank **B290** and high bank **B300** are set at 3600 psig; whilst the receiver tank **B260** is set at empty where $\approx$ 20 psig.

Next, Figure 4.19 shows when ball valve **B080** of low bank **B280** is opened, gas would flow from low bank **B280,** through flexible hose **B230** and nozzle **B250**, into the receiver tank **B260** to develop lower pressure difference. The gas flows due to differential pressure between the tanks and will continue to flow until pressure in the receiver tank **B260** approach the pressure in the low bank **B280**.

Then, Figure 4.20 shows when ball valve **B080** of medium bank **B290** is opened, the flow will switch to medium bank **B290** to continue refueling until pressure in the receiver tank **B260** approach the pressure in the medium bank **B290.**

Lastly, Figure 4.21 shows when ball valve **B080** of high bank **B300** is opened, the flow will switch to high bank **B300** to perform the same task until the vehicle tank **B260** reaches its maximum capacity $\approx$ 3000 psig. Coriolis flowmeter is generally regarded as a master flowmeter because it offers greatest accuracy and reliability under the exacting measurement conditions for determining mass of Compressed Natural Gas (CNG) compared to turbine **B320**, differential pressure **B330** and vortex **B340.** Since the flowmeters are installed parallel to each other, the natural gas flows only through any one of these flowmeters. By following all these procedures, data from coriolis **B350**, receiver pressure **B390** and load cells **B460** are sent to FieldPoint for SYSID analysis. The next section shows the analysis of experimental data stored in the FieldPoint.

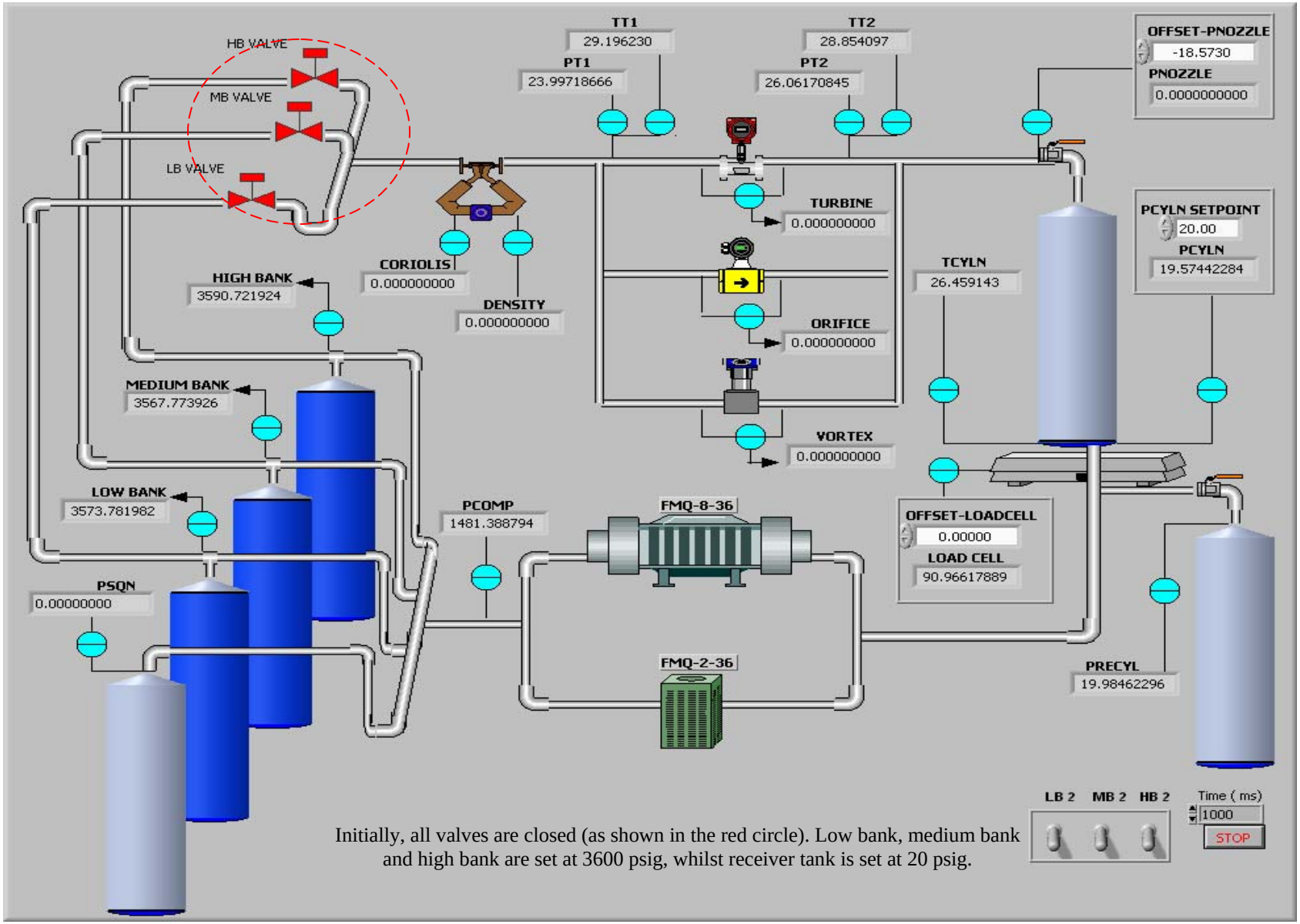

Initially, all valves are closed (as shown in the red circle). Low bank, medium bank and high bank are set at 3600 psig, whilst receiver tank is set at 20 psig.

Figure 4.18: Initial condition

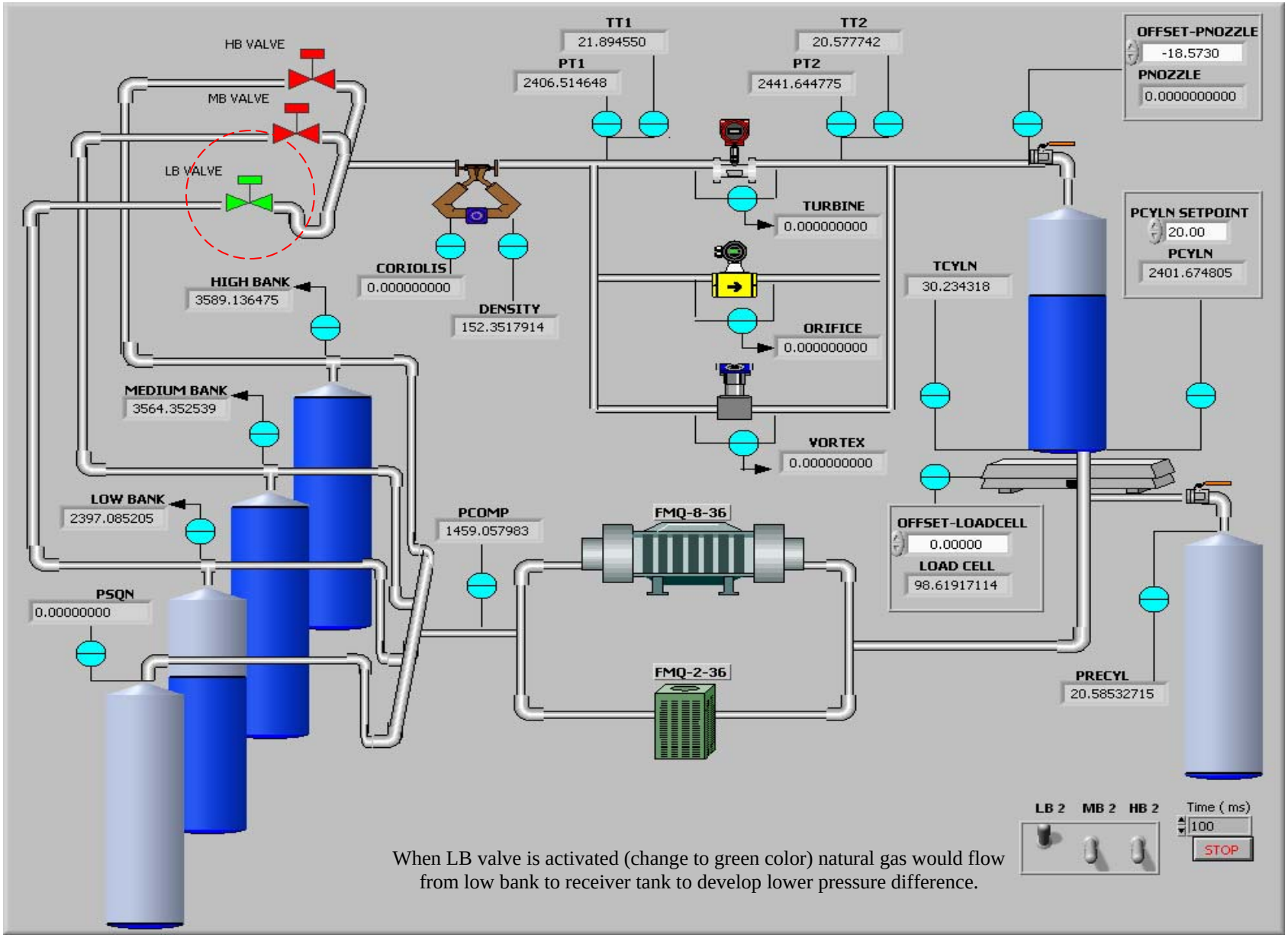

Figure 4.19: Low bank refueling

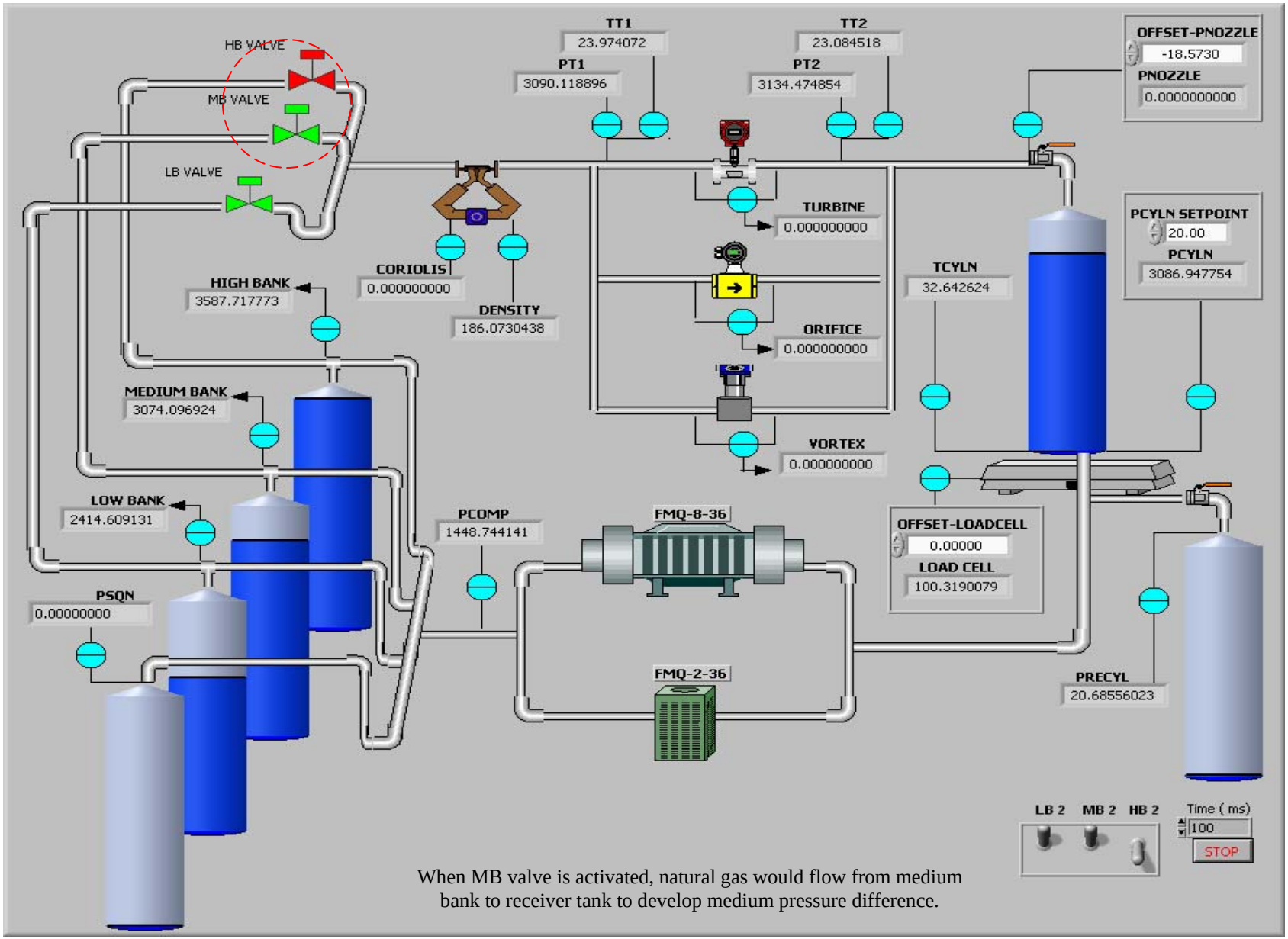

Figure 4.20: Medium bank refueling

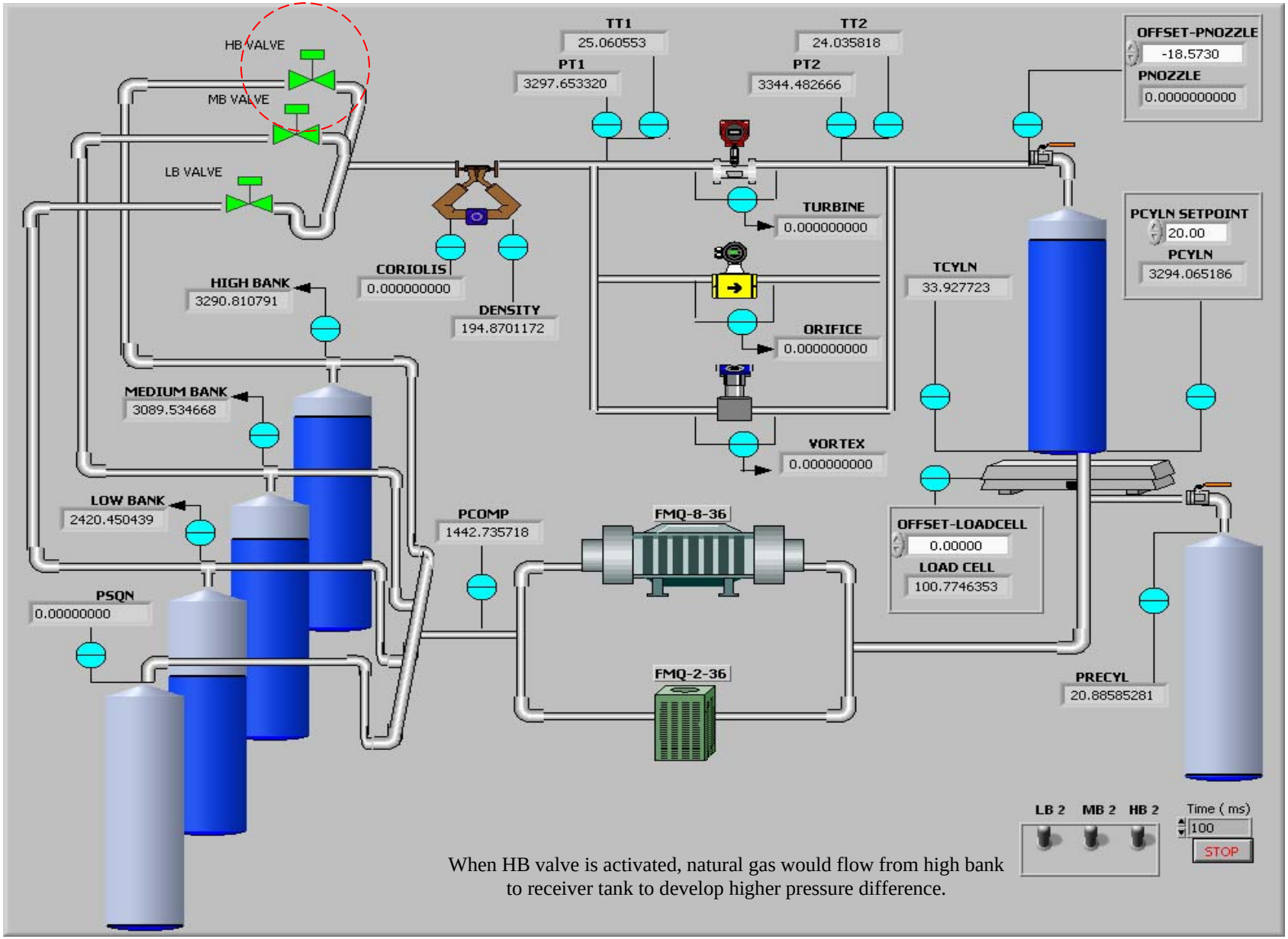

Figure 4.21: High bank refueling

4.4.4 Analyzing experimental data using LabVIEW

Figure 4.22 shows a sample of data taken from the FieldPoint. Please refer Table 4.2 for type of data in each column.

Table 4.2: Types of data taken from FieldPoint

Column	Signal	Unit	Types of data
1	date	month / day / year	Date of acquisition
2	time	hour / minute /second	Time of acquisition
3	PB1	psi	Pressure at low bank
4	PB2	psi	Pressure at medium bank
5	PB3	psi	Pressure at high bank
6	COMP	psi	Pressure at compressor
7	RECYL	psi	Pressure at recycle tank –(make-up cylinder)
8	PT1	psi	Pressure before flowmeter metering system
9	PT2	psi	Pressure after flowmeter metering system
10	PCYLN	psi	Pressure at receiver tank
11	TT1	°C	Temperature before flowmeter metering system
12	TT2	°C	Temperature after flowmeter metering system
13	TCYLND	°C	Temperature at receiver tank
14	Orifice	m^3/hr	Volumetric flowrate from orifice flowmeter
15	Vortex	m^3/hr	Volumetric flowrate from vortex flowmeter
16	Turbine	m^3/day	Volumetric flowrate from turbine flowmeter
17	PSQN	psi	Pressure at sequential tank
18	PNOZZLE	psi	Pressure at nozzle
19	Coriolis	kg/minute	Mass flowrate of CNG from coriolis flowmeter
20	Density	kg/m^3	Density of CNG from coriolis flowmeter
21	Load Cell	kg	Mass of CNG from load cell

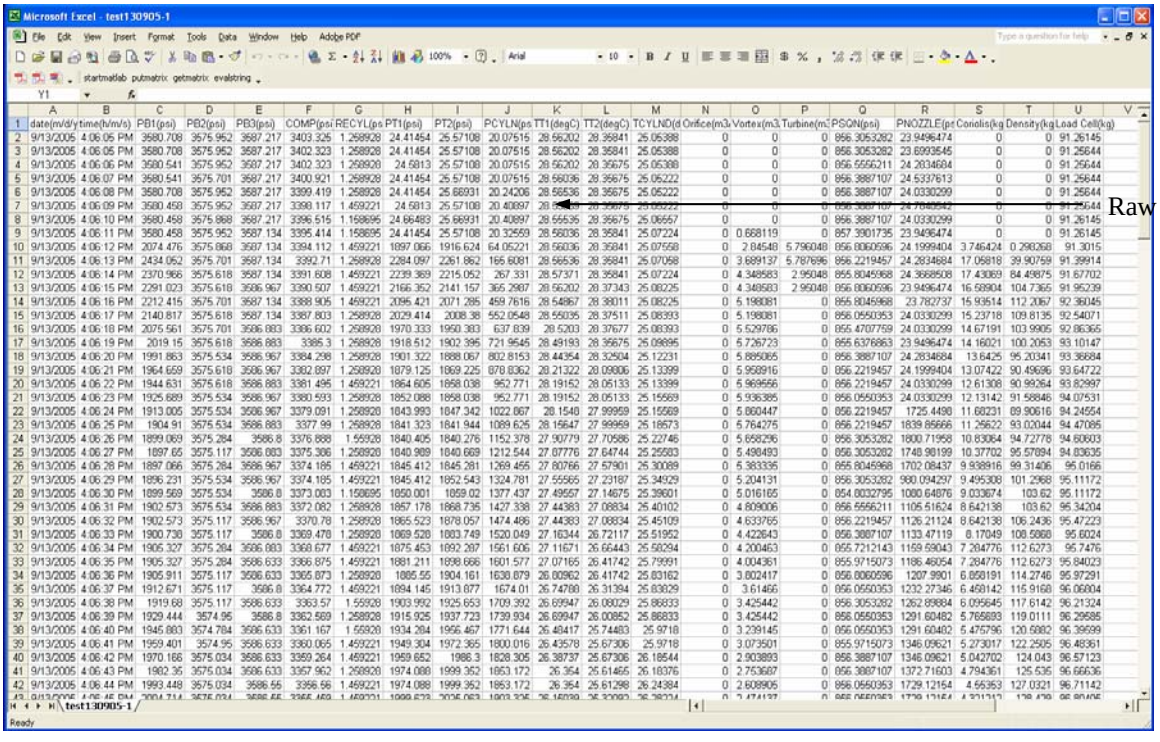

Figure 4.22: Sample of data

However, not all the data in Table 4.2 would be used to analyze the refueling process described from Figure 4.18-4.21, respectively. The only data that would be used are 'Coriolis', 'PCYLN' and 'Load Cell' data which represent mass flowrate measured by coriolis flowmeter, pressure inside receiver and total mass measured by load cell, respectively. Based on sample data shown in Figure 4.22, the data are modified as shown in Figure 4.23.

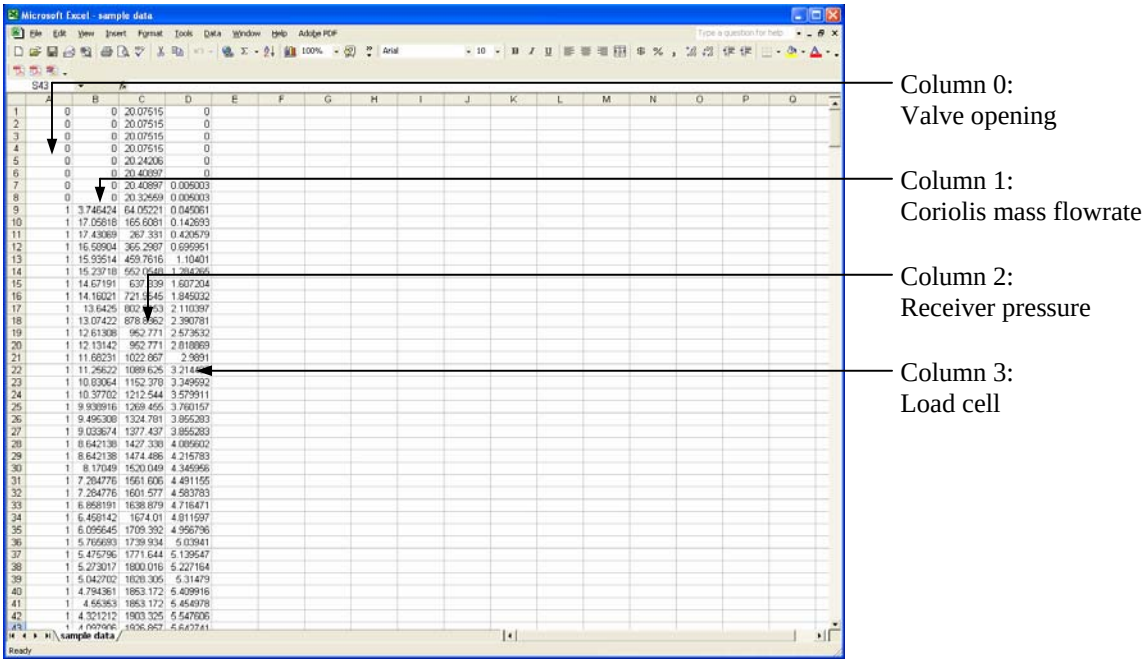

Figure 4.23: Modification of data

Notably, sequence 0 to 1 at column 0 is added manually to simulate the step input signal which represents closing and opening condition of low bank (LB), medium bank (MB) and high bank valves, respectively. However, no modifications are made to Column 1 and 2 which are data for 'Coriolis' and 'PCYLN', whilst, column 3 is new set of data to accumulate mass measured by load cell at each sampling time. The accumulated mass is developed by accumulating difference of 'Load Cell' at each row.

In following section, Figure 4.24 and Figure 4.25 are the LabVIEW front panel and LabVIEW program to convert modified data in Figure 4.23 to readable graphs such as valve opening, coriolis mass flowrate (CMF), receiver pressure and load cell, respectively.

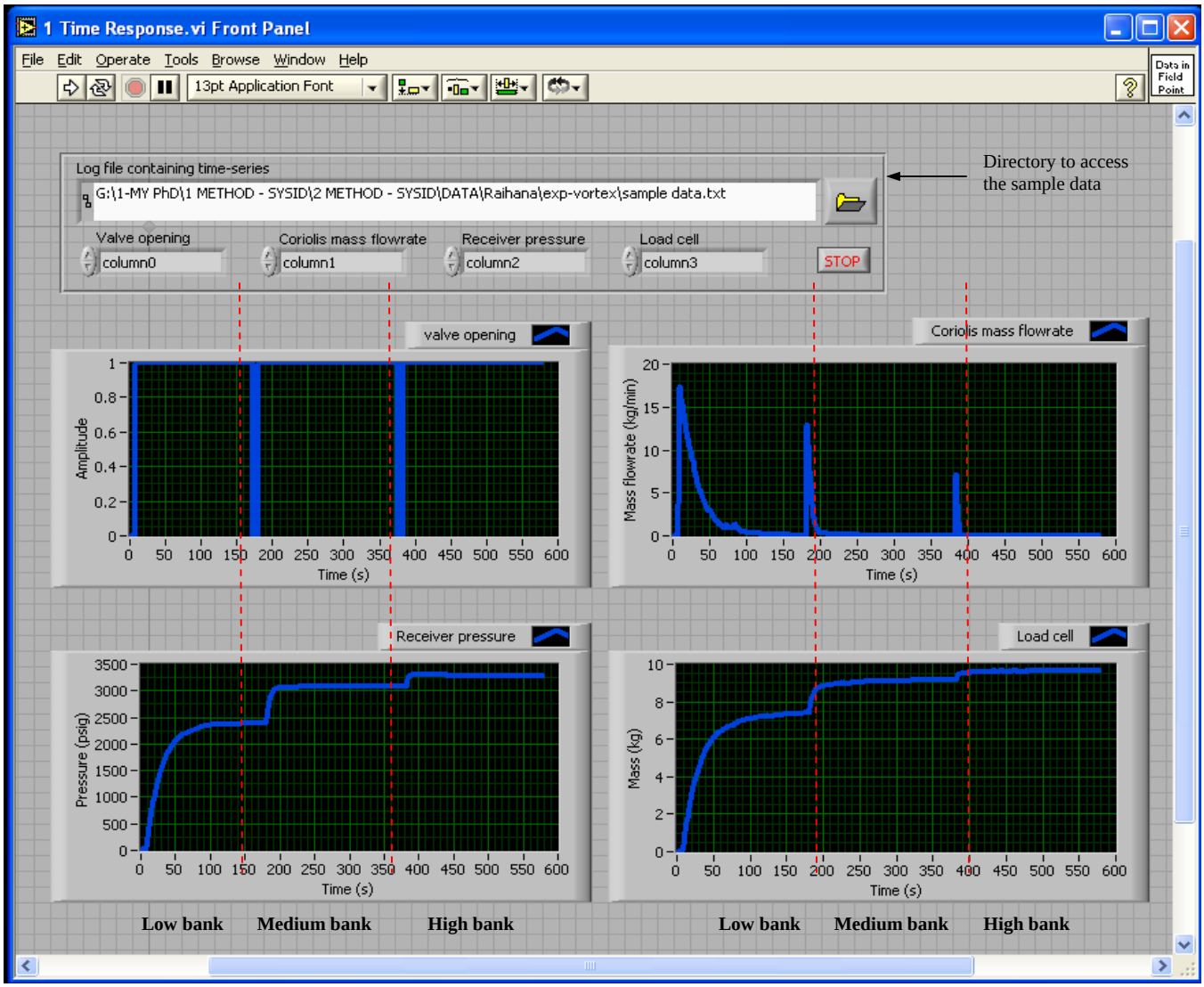

Figure 4.24: Sample of data is converted to readable graphs

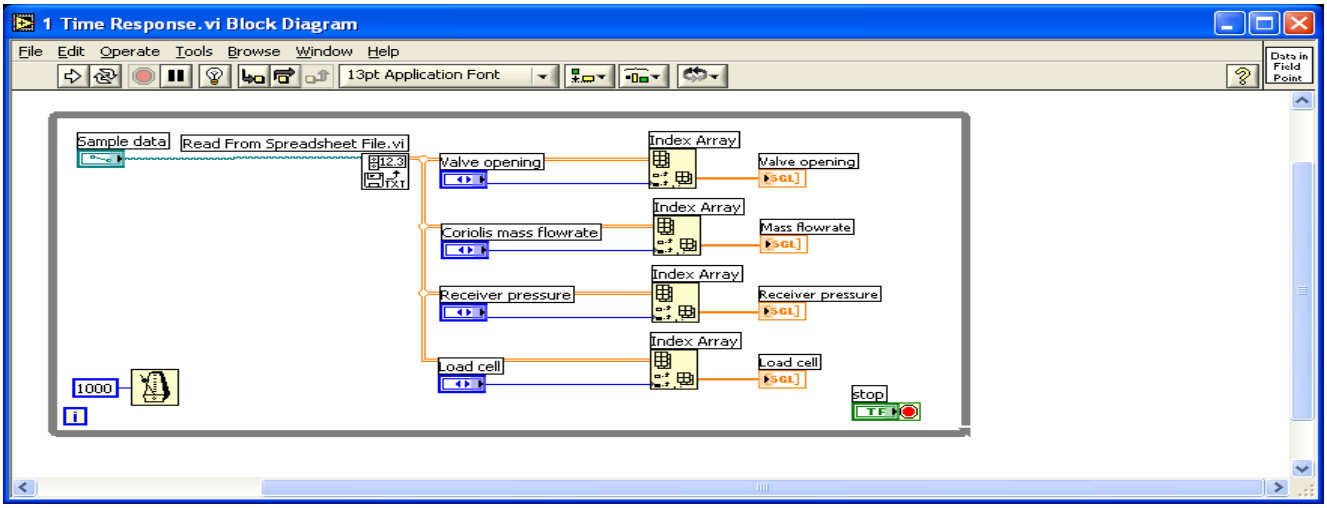

Figure 4.25: LabVIEW program to convert sample of data to readable graphs

Based on Figure 4.24, there are four types of graphs such as valve opening graph, coriolis mass flowrate (CMF) graph, receiver pressure graph and load cell graph for describing three process of refueling CNG: low bank refueling, medium bank refueling and high bank refueling which is separated using dashed line, respectively.

At first, when the low bank valve is opened, the valve opening graph is represented by a step function (which increases from 0 to 1), whilst the coriolis mass flowrate has increased from 0 kg/min to approximately 17 kg/min and dropped back to 0 kg/min back after 150 seconds. During this time range, the receiver pressure and load cell have increased approximately from 0 to 2500 psig and 0 to 7 kg, respectively.

Then, when the medium bank valve is opened, the valve opening graph is represented by a second step function, whilst the coriolis mass flowrate has increased again from 0 kg/min to approximately 13 kg/min and dropped back to 0 kg/min back after 350 seconds. During this time range, the receiver pressure and load cell have increased approximately from 2500 to 3000 psig and 7 to 9 kg, respectively.

Lastly, when the high bank valve is opened, the valve opening graph could be represented by the third step function, whilst the coriolis mass flowrate has increased again from 0 kg/min to approximately 5 kg/min and dropped back to 0 kg/min back after 400 seconds. During this time range, the receiver pressure and load cell have increased approximately from 3000 to 3300 psig and 9 to 9.6 kg, respectively.

This section has shown LabVIEW program to convert experimental data from FieldPoint to informative and representable graphs such as valve opening, coriolis mass flowrate (CMF), receiver pressure and load cell graphs, respectively. As shown by Figure 4.24, there are three types of refueling regions that have been developed such as low bank, medium bank and high bank refueling region. The suitable region to be selected as input and output data for SYSID would be described in the following section.

4.4.5 Selecting input and output data for SYSID

As mentioned in the introduction section, the input and output signals for identifying coriolis flowmeter are the step function and output signals from the system itself, in which, it is the valve opening and the coriolis mass flowrate (CMF) signals as shown in Figure 4.26 and Figure 4.27, respectively. Notably, at the low bank region, mass flowrate values are greater than zero if compared to mass flowrate at medium and high bank region. Therefore, only CMF data at low bank region could be selected for identification work (which is represented in red dashed line).

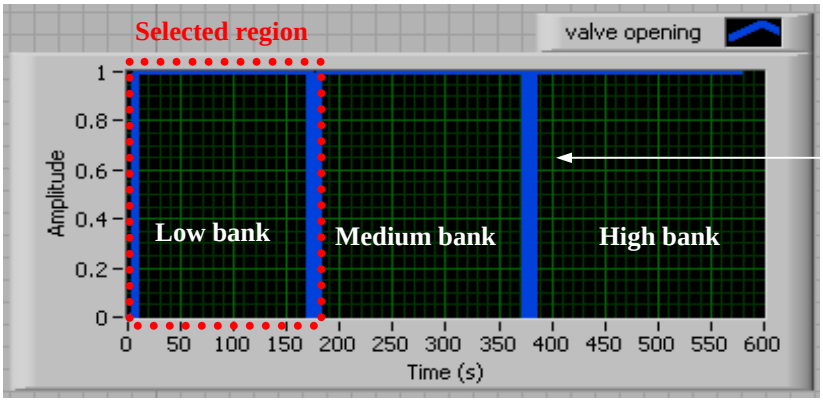

Notably, the signal of valve opening is equivalent to step function.

Figure 4.26: Input data for SYSID

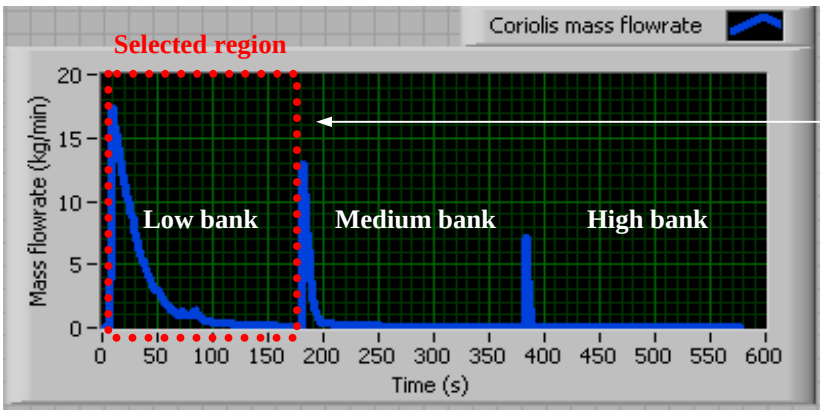

Only data at low bank region is selected for SYSID work.

Most of data at medium and high bank regions are approaching to zero compared to low bank

If data chosen are closed to zero, the SYSID prediction would be inaccurate.

Figure 4.27: Output data for SYSID

From the selected input and output data at low bank region, the discrete model of coriolis mass flowrate (CMF) would be determined based on three SYSID approaches such as non recursive, recursive and state space approach. The respective LabVIEW programs for each approach are shown in following section by Figure 4.28 to 4.30.

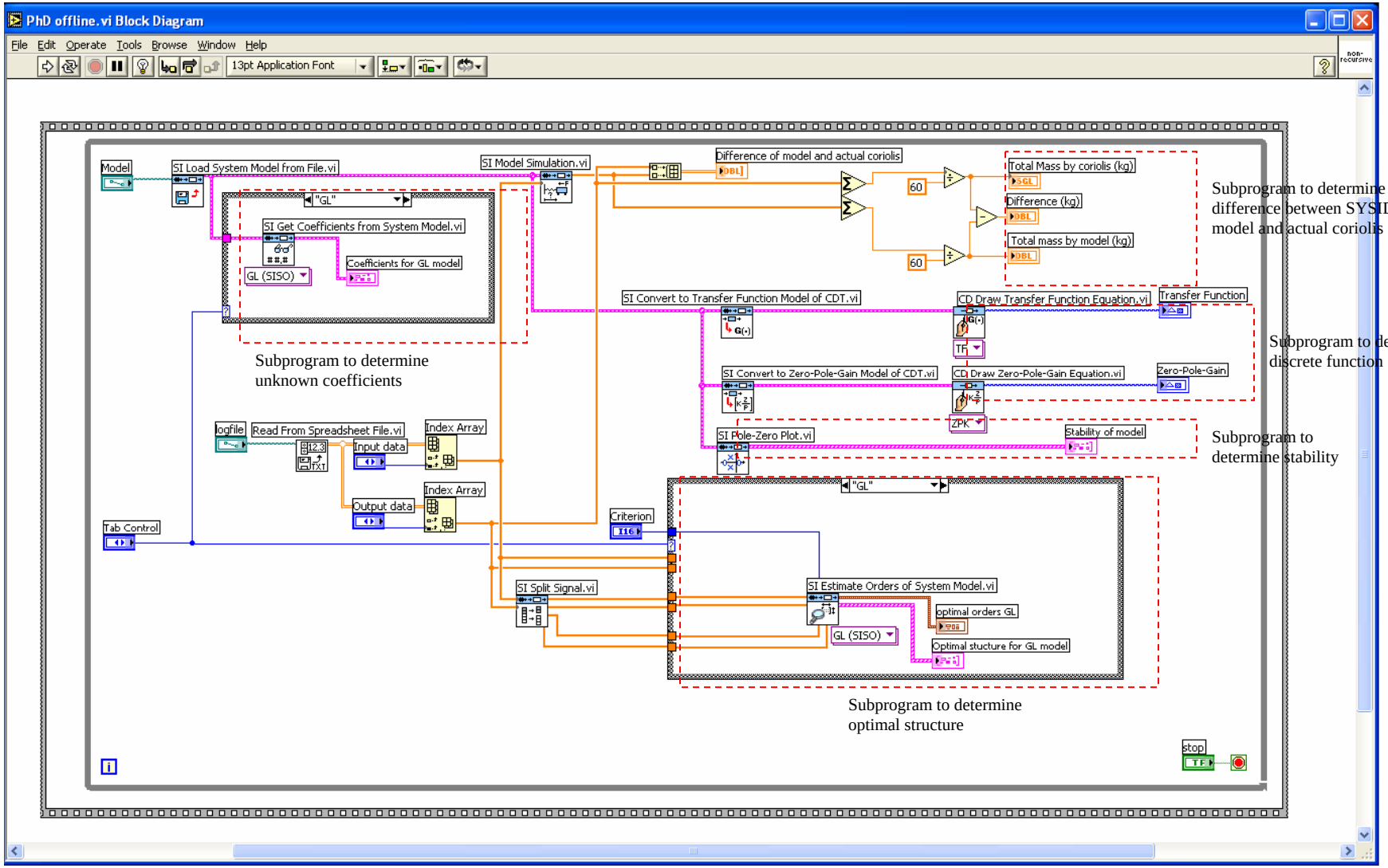

Figure 4.28: LabVIEW program to determine discrete model of CMF using non-recursive approach

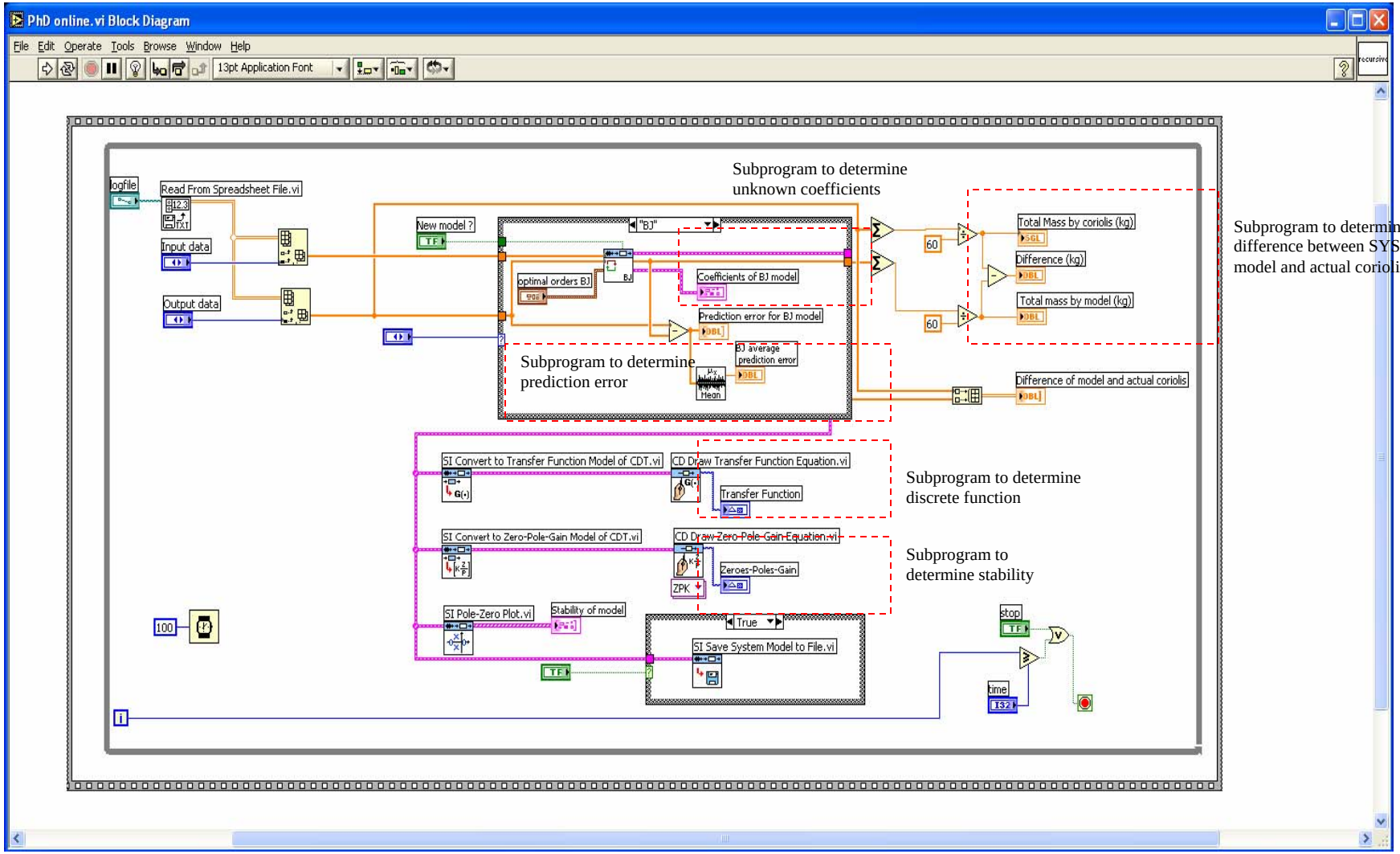

Figure 4.29: LabVIEW program to determine discrete model of CMF using recursive approach

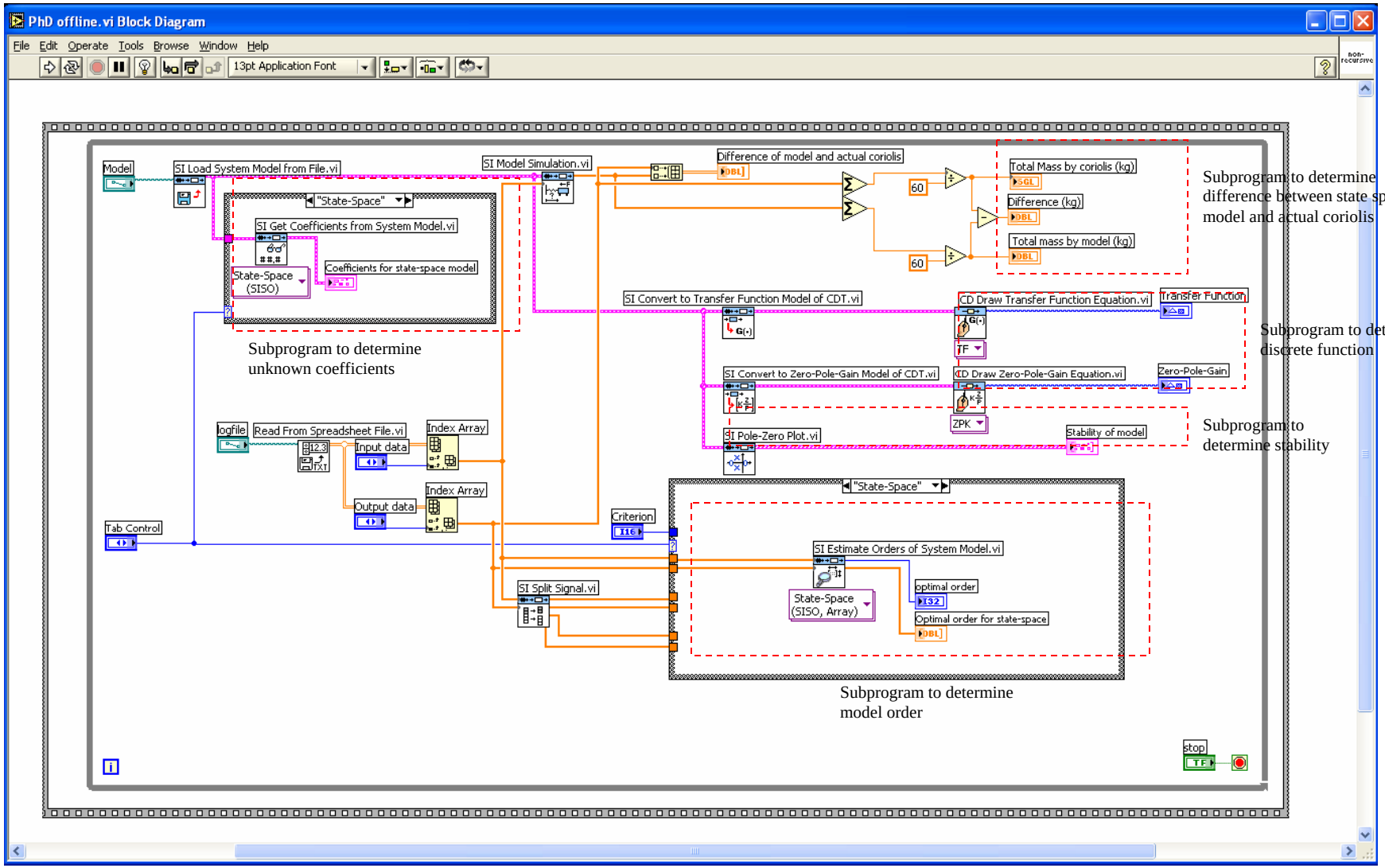

Figure 4.30: LabVIEW program to determine discrete model of CMF using state space approach

4.5 Determine discrete model of coriolis mass flowrate (CMF)

The following section discusses the forth steps of SYSID methodology i.e., determine discrete model of coriolis mass flowrate (CMF) using LabVIEW. Figure 4.28-4.30 shown in previous section are the LabVIEW programs to determine discrete model of CMF, whilst Figure 4.31-4.33 shown in following section are the LabVIEW front panels for non recursive, recursive and state space approach, respectively.

Based on Figure 4.31-4.33, the front panels for non recursive, recursive and state space are differentiated by three parts such as ‘optimal structure’ part, ‘prediction error’ part and ‘optimal order’ part, respectively. In following section, LabVIEW front panel of non recursive is shown for describing the ‘optimal order’ part.

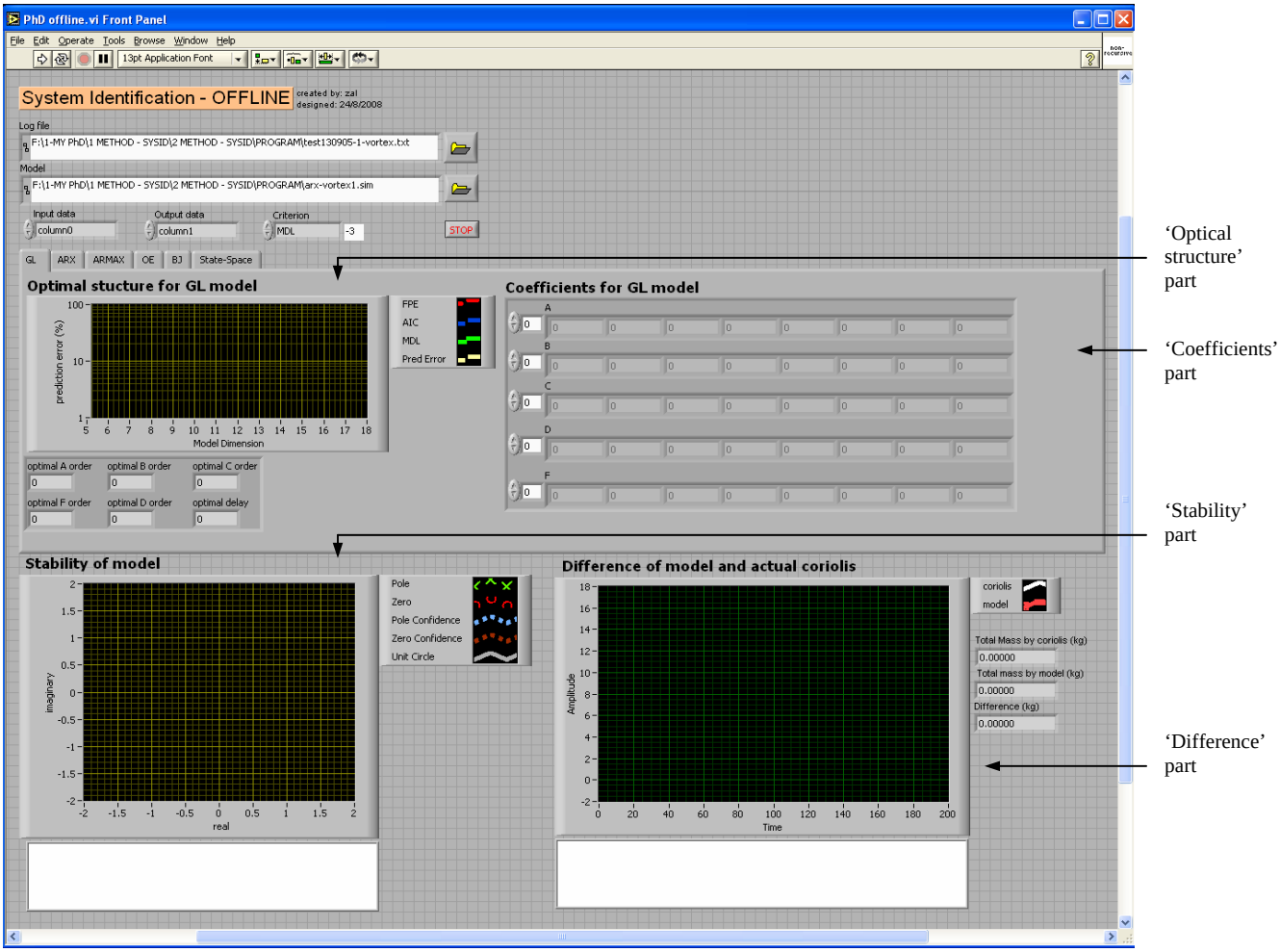

Figure 4.31: LabVIEW front panel to determine discrete model of CMF using non-recursive approach

Based on Figure 4.31, the non recursive approach would determine discrete model for CMF based on optimal structure analysis. The optimal structure analysis would determine suitable number of delays and suitable number of orders for $A(q), B(q), C(q), D(q), F(q)$ equations. As mentioned in Chapter 2, number of delays and number of order are chosen based on the minimum percentage of prediction error shown by Akaike's Information Criterion (AIC), Akaike's Final Prediction Error Criterion (FPE), and Minimum Data Length Criterion (MDL). In following section, LabVIEW front panel of recursive approach is shown for describing the 'prediction error' part.

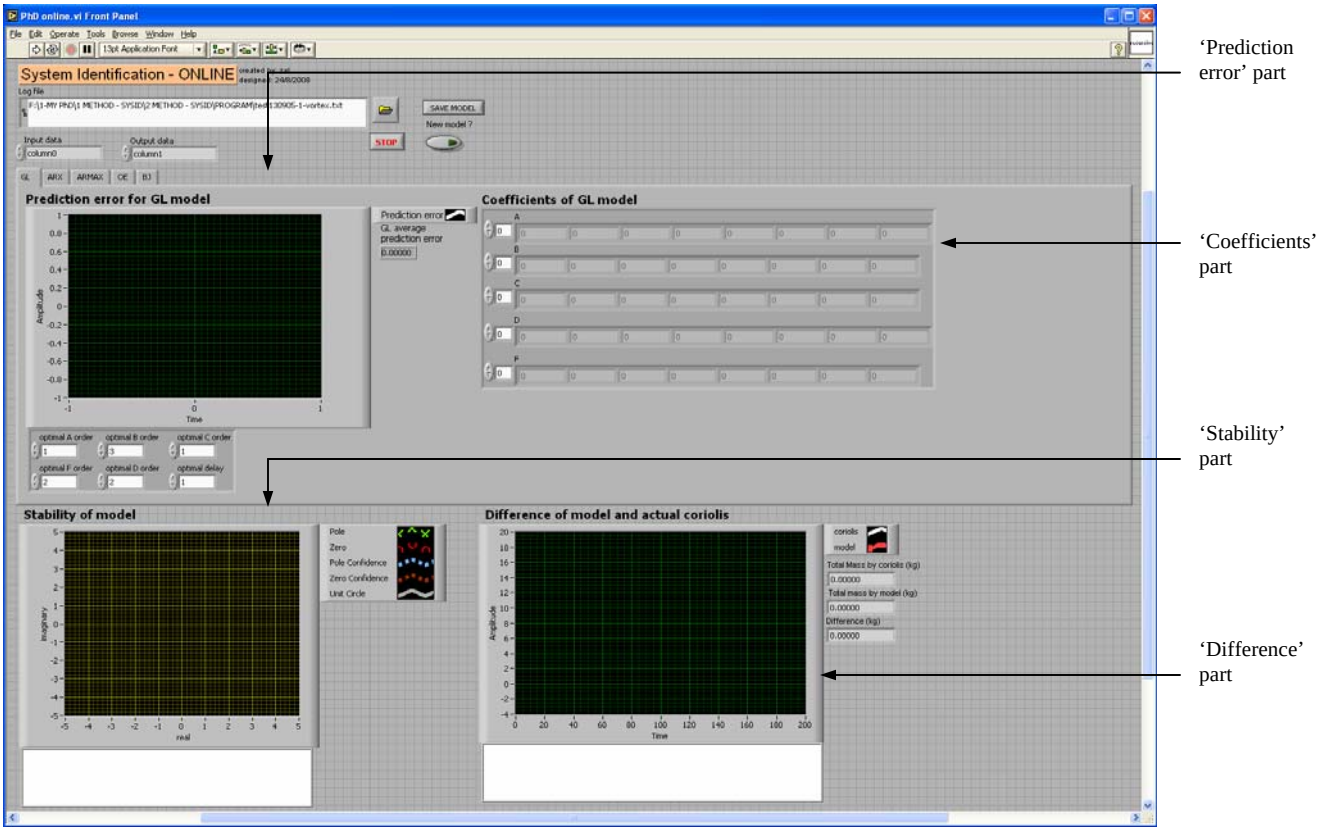

Figure 4.32: LabVIEW front panel to determine discrete model of CMF using recursive approach

Based on Figure 4.32, the recursive approach would determine discrete model for CMF based on prediction error analysis. The prediction error analysis would determine the amplitude of difference error and the average of difference error between the predicted model and the actual coriolis which is displayed on 'prediction error' part.

If the error is higher, the recursive program would decrease the prediction error until it is minimized to zero error, or any minimum error specified by the user. In the following section, the LabVIEW front panel of state space approach is shown for describing the 'optimal order' part.

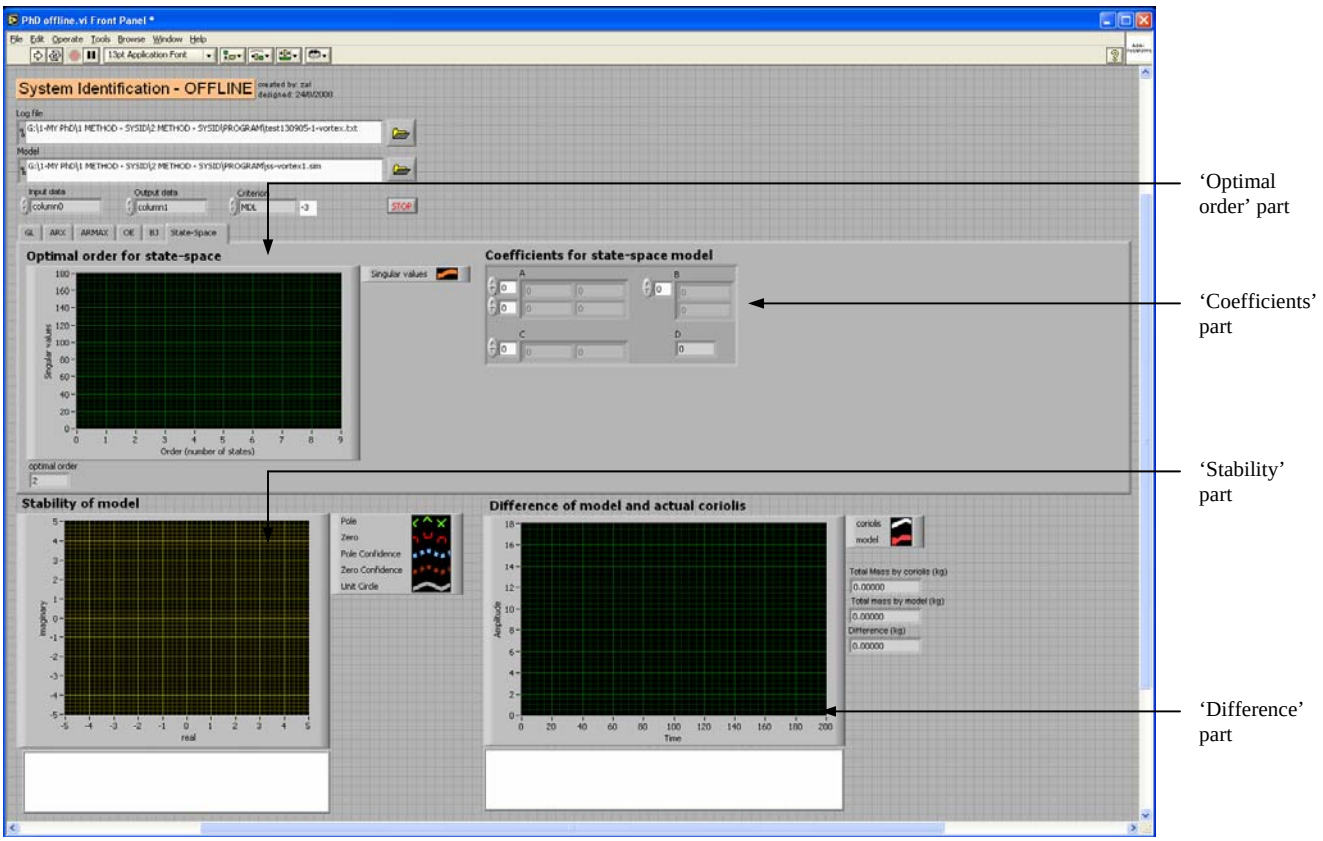

Figure 4.33: LabVIEW front panel to determine discrete model of CMF using state space approach

Based on Figure 4.33, the state space approach would determine discrete model for CMF based on optimal order analysis. The optimal order analysis would determine a suitable order for dimension of state vector $x(n)$ based on minimum number of singular values. As mentioned in Chapter 3, the dimension of state vector $x(n)$ is important for determining the system matrix A i.e., in which, the only setting that needs to be analyzed for the state space model.

Notably, from Figure 4.31-4.33, there are three similar parts in each front panels such as 'coefficients' part, 'stability' part and 'difference' part which are discussed in following section.

The ‘coefficients’ part shown in Figure 4.31 and Figure 4.32 display the unknown coefficients in polynomial form which are the unknown coefficients in $A(q), B(q), C(q), D(q), F(q)$ functions, whilst the ‘coefficients’ part shown in Figure 4.33 displays the unknown coefficients in state space form which is in A, B, C, D matrices. Since, the number of delays and the number of orders predicted by non recursive approach are already optimal, the same number of delays and the same number of orders would be used in the recursive approach. The number of delays would be highlighted by value ‘0’. Delays are indication for a lapse of time before results from model of coriolis mass flowrate (CMF) equals results from the actual coriolis. Notably, the number of orders in non recursive and recursive approach is equivalent to number of unknown coefficients in $A(q), B(q), C(q), D(q), F(q)$ functions.

From the coefficients values, polynomial functions would be developed and represented in two equations: zeroes-poles equation and difference equation. Since, FieldPoint uses sampling time of 1 second, both equations would be displayed in discrete form in which, Z-transformation with sampling period of 1 second. Based on discrete Z-transformation, the zeroes-poles equation would provide stability for the predicted models of CMF which is shown in the ‘stability’ part, whilst the difference equation would provide the predicted values of CMF which is calculated using power series expansion method. As described in Chapter 2, the power series expansion method is an infinite series of predicted values of CMF but in the discrete form. Please refer Chapter 2 for details explanations on power series expansion method. The series of predicted values would be accumulated and would be compared with the final mass measured by actual coriolis. Results of comparison would be displayed in ‘difference’ part of LabVIEW front panels.

This section has discussed LabVIEW program and LabVIEW front panel to develop discrete model of coriolis mass flowrate (CMF) using non-recursive, recursive and state space approach. As shown in Figure 4.31-4.33, there are five SYSID parametric models and one state space model that need to be tested such as GL, ARX, ARMAX, OE and BJ. Figure 4.34-4.38 in following section shows the analyses of SYSID parametric models after tested using the first approach i.e., non recursive approach.

4.5.1 Analyses of non recursive approach

Figure 4.34 shows the discrete model for coriolis mass flowrate developed using General Linear (GL) model. From the 'optimal structure' part, criterions FPE, AIC and MDL have shown that model dimension '9' has the smallest prediction error compared to other model dimensions. In this section, the FPE, AIC and MDL are represented by red, blue and green color, respectively.

The model dimension '9' is given by total sum of each order, $A+B+C+D+F$, (1+3+1+2+2 = 9) which equals to number of order and number of unknown coefficients in $A(q), B(q), C(q), D(q), F(q)$ equations.

The delays shown is '1' which is highlighted by one '0' in the 'coefficient' part.

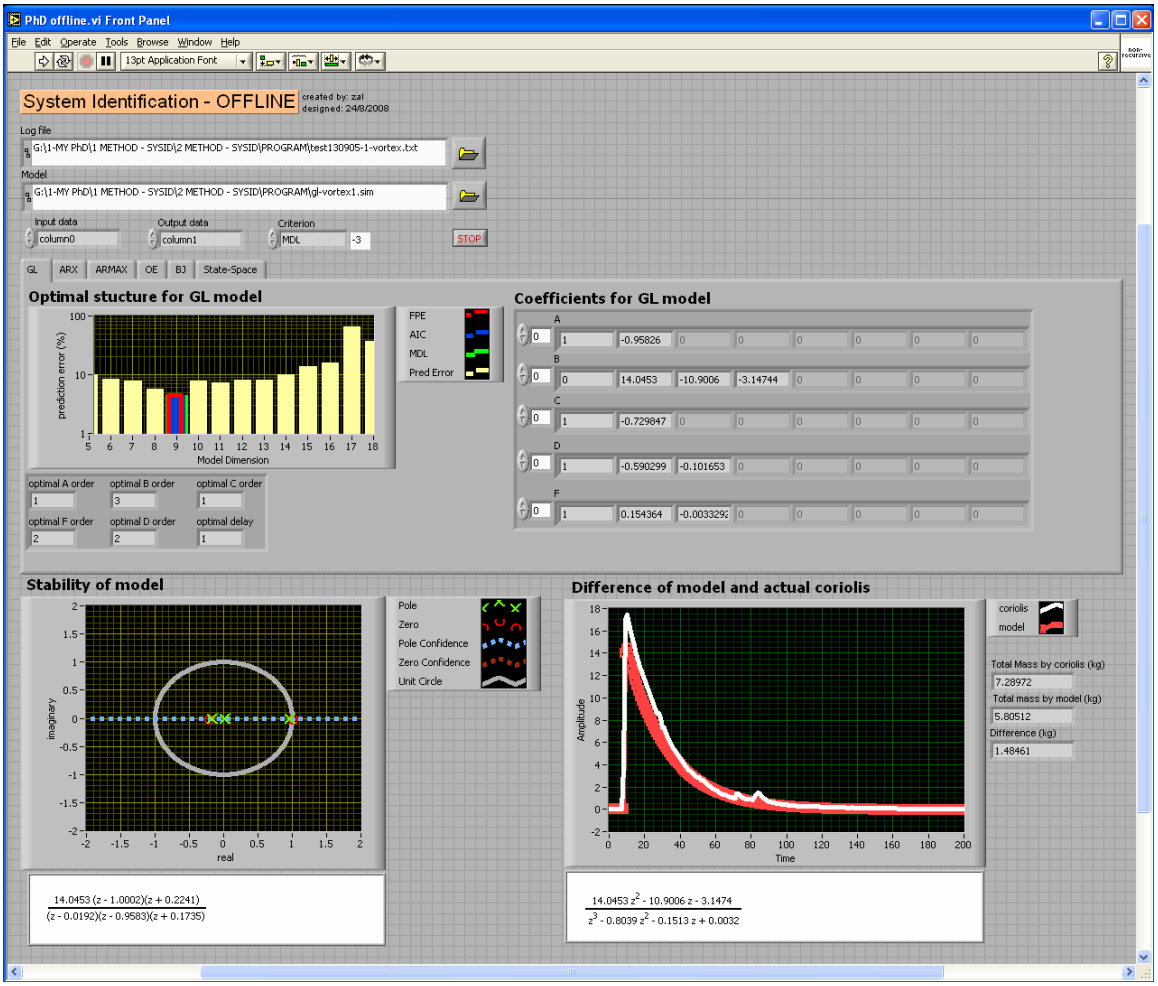

Figure 4.34: Discrete model of CMF using GL model

Based on Figure 4.34, the order and the unknown coefficients in polynomial function are

$$A(q) = 1 - 0.9582q^{-1} \tag{4.1}$$

$$B(q) = 14.0453q^{-1} - 10.9006q^{-2} - 3.1474q^{-3} \tag{4.2}$$

$$C(q) = 1 - 0.7299q^{-1} \tag{4.3}$$

$$D(q) = 1 - 0.5903q^{-1} - 0.1017q^{-2} \tag{4.4}$$

$$F(q) = 1 + 0.1544q^{-1} - 0.0033q^{-2} \tag{4.5}$$

Whilst, the zeroes-poles function could be represented as

$$\frac{14.0453(z - 1.0002)(z + 0.2241)}{(z - 0.0192)(z - 0.9583)(z + 0.1735)} \tag{4.6}$$

As shown from the ‘stability’ part, all zeroes and poles are inside the unit circle which indicates the developed model is boundedly stable. In this section, the zeroes and poles are represented by red and green color, respectively.

The difference equation for the model could be represented as

$$\frac{14.0453z^2 - 10.9006z - 3.1474}{z^3 - 0.8339z^2 - 0.1513z + 0.0032} \tag{4.7}$$

From the ‘difference’ part, the total mass measured by actual coriolis and GL models are 7.2897 kg and 5.8051 kg, respectively, whilst the difference is 1.4846 kg. Since, the GL model produces smaller difference, the graph developed by GL model overlaps the graph developed by actual coriolis, with a minor difference.

In this section, all developed models and actual coriolis are represented using red and white color, respectively. The following section discusses the second analysis of SYSID parametric models i.e., the Autoregressive Exogeneous Input (ARX) model.

Figure 4.35 shows the discrete model for coriolis mass flowrate developed using Autoregressive Exogeneous Input (ARX) model. From the 'optimal structure' part, criterions FPE and MDL have shown that model dimension '4' has the smallest prediction error, whilst criterion AIC has shown that model dimension '5' has the smallest prediction error compared to other model dimensions. Since model dimension '4' is smaller than model dimension '5', it is chosen to be the most optimal structure for ARX.

The model dimension '4' is given by total sum of each order, $A+B$, (1+3 = 4) which equals to number of order and number of unknown coefficients in $A(q), B(q)$ equations.

The delays shown is '1' which is highlighted by one '0' in the 'coefficient' part.

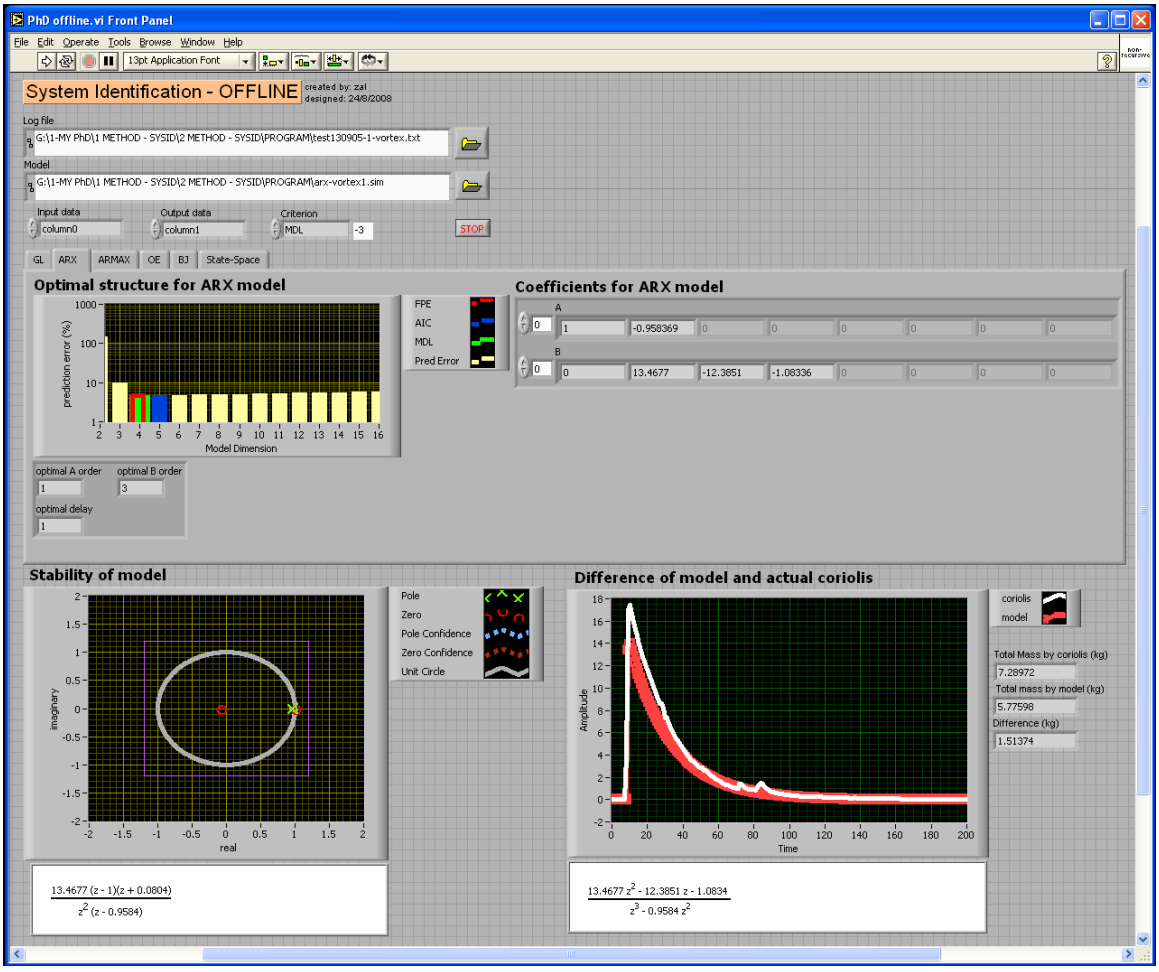

Figure 4.35: Discrete model of CMF using ARX model

Based on Figure 4.35, the order and the unknown coefficients in polynomial function are

$$A(q) = 1 - 0.9584q^{-1} \tag{4.8}$$

$$B(q) = 13.4677q^{-1} - 12.3851q^{-2} - 1.0834q^{-3} \tag{4.9}$$

Whilst, the zeroes-poles function could be represented as

$$\frac{13.4677(z-1)(z+0.0804)}{z^2(z-0.9584)} \tag{4.10}$$

As shown from the 'stability' part, all zeroes and poles are inside the unit circle which indicates the developed model is boundedly stable.

The difference equation for the model could be represented as

$$\frac{13.4677z^2 - 12.3851z - 1.0834}{z^3 - 0.9584z^2} \tag{4.11}$$

From the 'difference' part, the total mass measured by actual coriolis and ARX models are 7.2897 kg and 5.7760 kg, respectively, whilst the difference is 1.5137 kg. Since, the ARX model produces smaller difference, the graph developed by ARX model overlaps the graph developed by actual coriolis, with a minor difference.

The following section discusses the third analysis of SYSID parametric models i.e., the Autoregressive Moving Average with Exogeneous Input (ARMAX) model.

Figure 4.36 shows the discrete model for coriolis mass flowrate using Autoregressive Moving Average with Exogeneous Input (ARMAX) model. From the 'optimal structure' part, criterions FPE, AIC and MDL have shown that model dimension '5' has the smallest prediction error compared to other model dimensions.

The model dimension '5' is given by total sum of each order, $A+B+C$, (1+3+1 = 5) which equals to number of order and number of unknown coefficients in $A(q), B(q), C(q)$ equations.

The delays shown is '3' which is highlighted by three '0' in the 'coefficient' part.

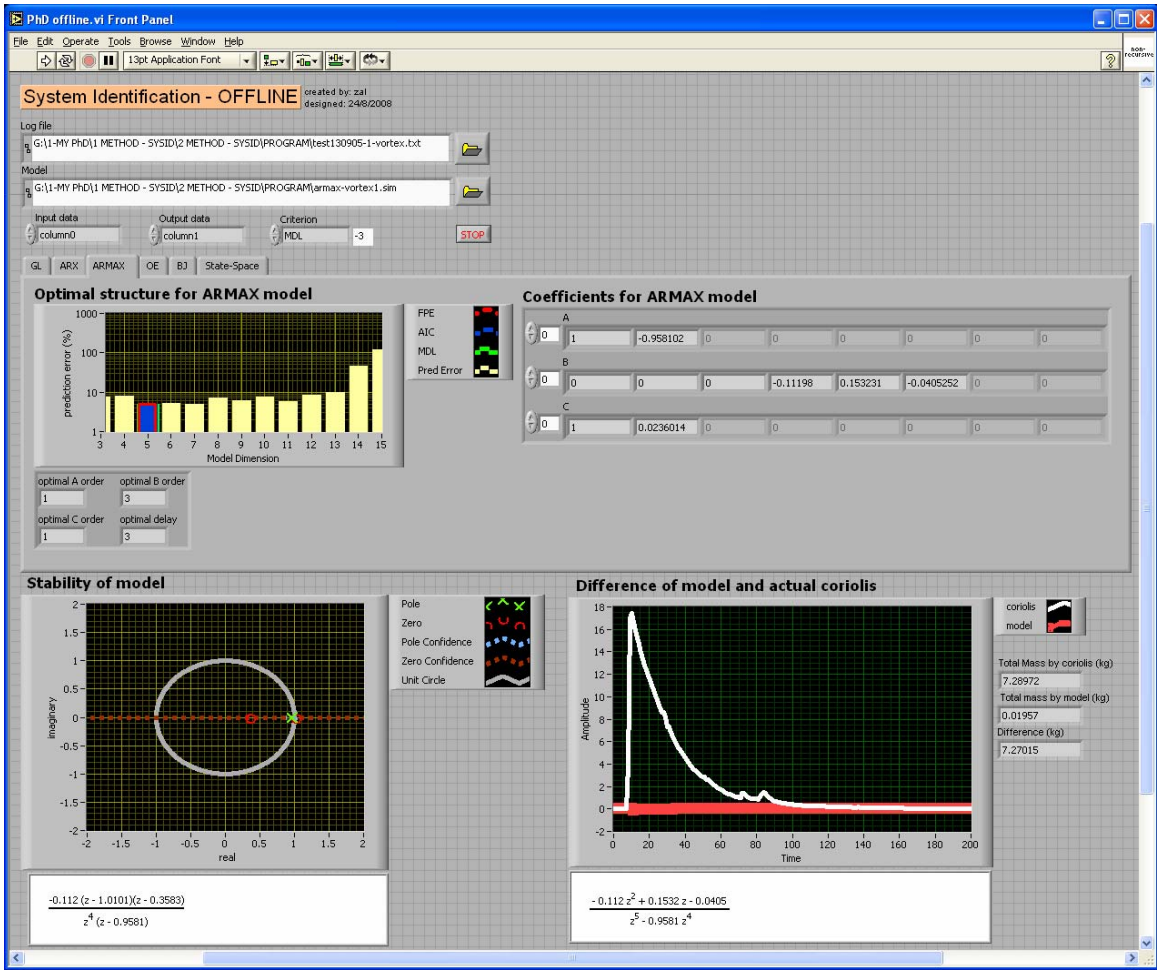

Figure 4.36: Discrete model of CMF using ARMAX model

Based on Figure 4.36, the order and the unknown coefficients in polynomial function are

$$A(q) = 1 - 0.9581q^{-1} \tag{4.12}$$

$$B(q) = -0.1120q^{-3} - 0.1532q^{-4} - 0.0405q^{-5} \tag{4.13}$$

$$C(q) = 1 - 0.0236q^{-1} \tag{4.14}$$

Whilst, the zeroes-poles function could be represented as

$$\frac{-0.1120(z-1.0101)(z-0.3583)}{z^4(z-0.9581)} \tag{4.15}$$

As shown from the 'stability' part, all zeroes and poles are inside the unit circle which indicates the developed model is stable.

The difference equation for the model could be represented as

$$\frac{14.0453z^2 - 10.9006z - 3.1474}{z^3 - 0.8339z^2 - 0.1513z + 0.0032} \tag{4.16}$$

From the 'difference' part, the total mass measured by actual coriolis and ARMAX models are 7.2897 kg and 0.0196 kg, respectively, whilst the difference is 7.2702 kg. Since, the ARMAX model produces bigger difference, the graph developed by ARMAX model doesn't overlap the graph developed by actual coriolis.

The following section discusses the fourth analysis of SYSID parametric models i.e., the Output Error (OE) model.

Figure 4.37 shows the discrete model for coriolis mass flowrate using Output Error (OE) model. From the 'optimal structure' part, criterions FPE, AIC and MDL have shown that model dimension '7' has the smallest prediction error compared to other model dimensions.

The model dimension '7' is given by total sum of each order, $B+F$, (6+1 = 7) which equals to number of order and number of unknown coefficients in $B(q), F(q)$ equations.

The delays shown is '5' which is highlighted by five '0' in the 'coefficient' part.

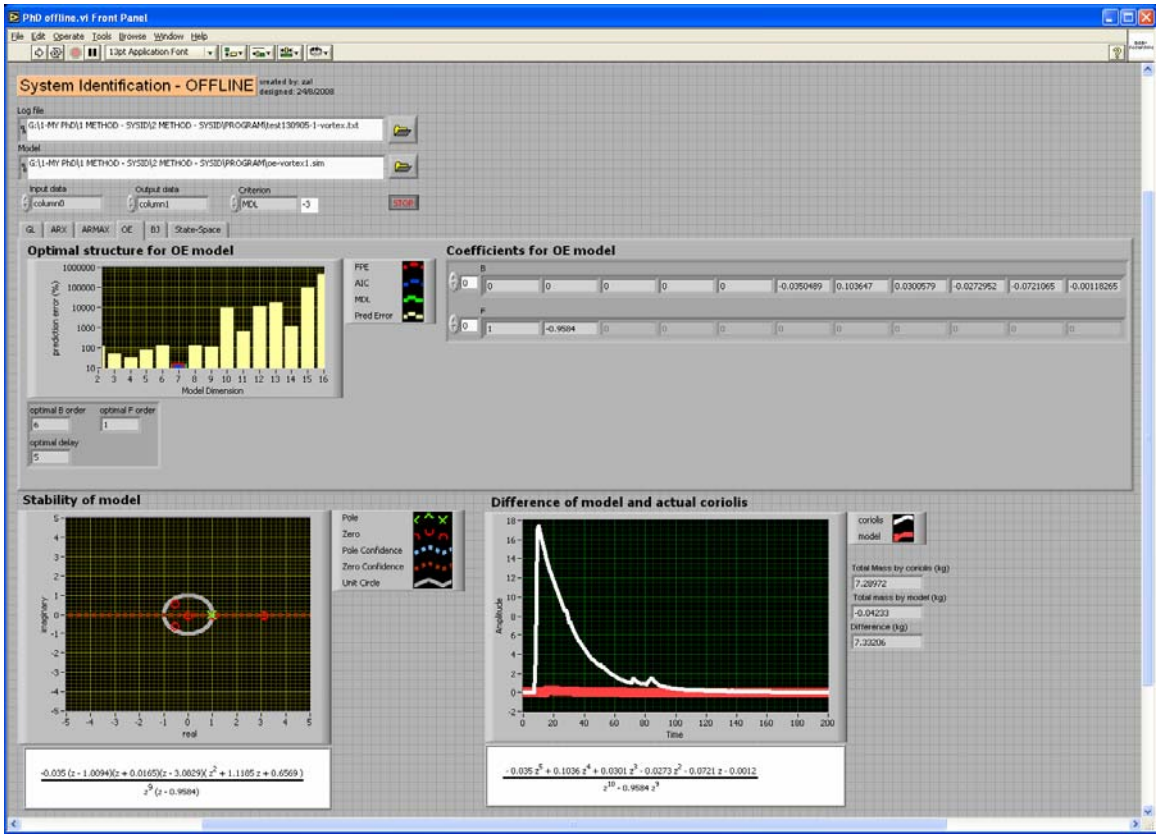

Figure 4.37: Discrete model of CMF using OE model

Based on Figure 4.37, the order and the unknown coefficients in polynomial function are

$$B(q) = -0.0350q^{-5} + 0.1036q^{-6} + 0.0301q^{-7} - 0.0273q^{-8} - 0.0721q^{-9} - 0.0012q^{-10} \quad (4.17)$$

$$F(q) = 1 - 0.9584q^{-1} \quad (4.18)$$

Whilst, the zeroes-poles function could be represented as

$$\frac{-0.035(z-1.0094)(z+0.0165)(z-3.0829)(z^2+1.1185z+0.6569)}{z^9(z-0.9584)} \quad (4.19)$$

As shown from the 'stability' part, one of the zeroes is located outside from the unit circle which is at 3.0829. This indicates that the developed model is not stable.

The difference equation for the model could be represented as

$$\frac{-0.035z^5 + 0.1036z^4 + 0.0301z^3 - 0.0273z^2 - 0.0721z - 0.0012}{z^{10} - 0.9584z^9} \quad (4.20)$$

From the 'difference' part, the total mass measured by actual coriolis and OE models are 7.2897 kg and -0.0423 kg, respectively, whilst the difference is 7.3321 kg. Since, the OE model produces bigger difference, the graph developed by OE model doesn't overlap the graph developed by actual coriolis.

The following section discusses the fifth analysis of SYSID parametric models i.e., the Box-Jenkins (BJ) model.

Figure 4.38 shows the discrete model for coriolis mass flowrate using Box-Jenkins (BJ) model. From the 'optimal structure' part, criterions FPE, AIC and MDL have shown that model dimension '9' has the smallest prediction error compared to other model dimensions.

The model dimension '9' is given by total sum of each order, $B+C+D+F$, (4+3+1+1 = 9) which equals to number of order and number of unknown coefficients in $B(q), C(q), D(q), F(q)$ equations.

The delays shown is '4' which is highlighted by four '0' in the 'coefficient' part.

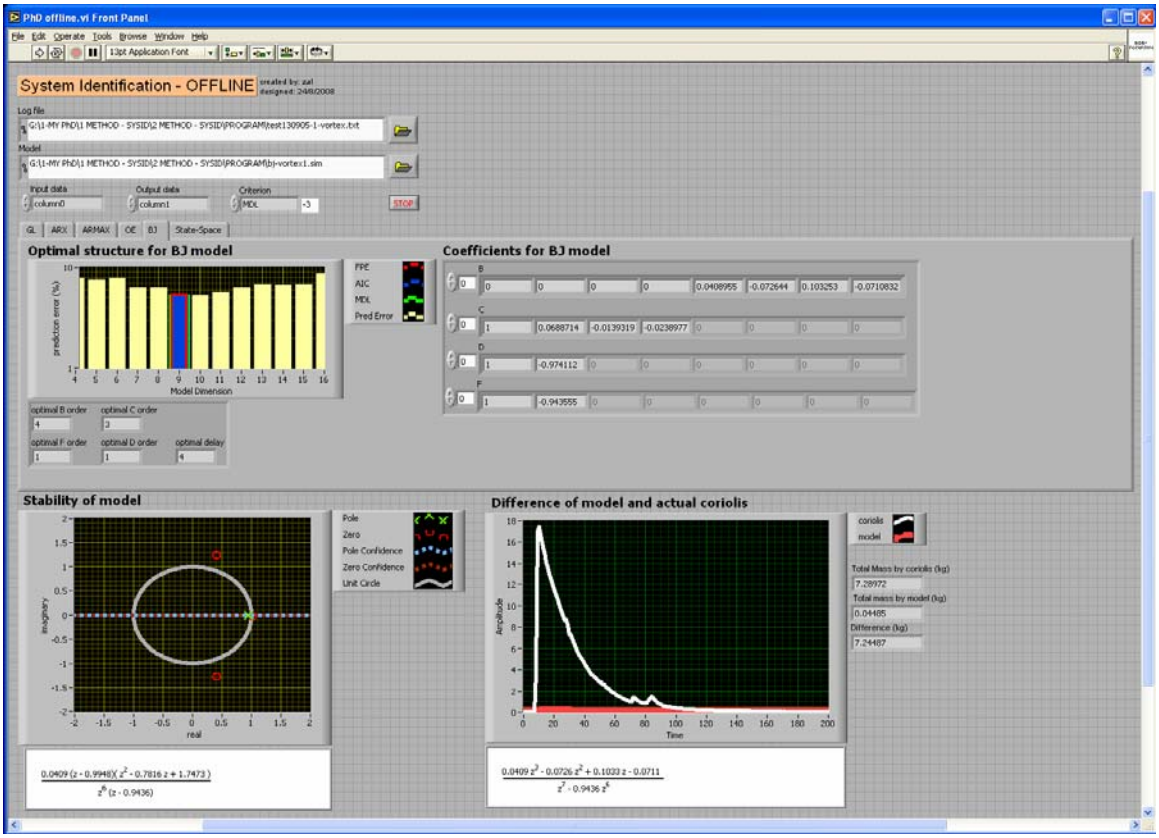

Figure 4.38: Discrete model of CMF using BJ model

Based on Figure 4.38, the order and the unknown coefficients in polynomial function are

$$B(q) = 0.0409q^{-4} - 0.0726q^{-5} + 0.1033q^{-6} - 0.0711q^{-7} \quad (4.21)$$

$$C(q) = 1 + 0.0689q^{-1} - 0.0139q^{-2} - 0.0239q^{-3} \quad (4.22)$$

$$D(q) = 1 - 0.9741q^{-1} \quad (4.23)$$

$$F(q) = 1 - 0.9436q^{-1} \quad (4.24)$$

Whilst, the zeroes-poles function could be represented as

$$\frac{0.0409(z - 0.9948)(z^2 - 0.7816z + 1.7473)}{z^6(z - 0.9436)} \quad (4.25)$$

As shown from the 'stability' part, two of the zeroes are located outside from the unit circle which is $0.48 \pm$ j1.25. This indicates that the developed model is not stable.

The difference equation for the model could be represented as

$$\frac{0.0409z^3 - 0.0726z^2 + 0.1033z - 0.0711}{z^7 - 0.9436z^6} \quad (4.26)$$

From the 'difference' part, the total mass measured by actual coriolis and BJ models are 7.2897 kg and 0.0449 kg, respectively, whilst the difference is 7.2449 kg. Since, the BJ model produces bigger difference, the graph developed by BJ model doesn't overlap the graph developed by actual coriolis.

Figure 4.34-4.38 in this section has shown the LabVIEW front panels to develop the discrete model for coriolis mass flowrate (CMF) based on the first approach which is non-recursive approach. Figure 4.39-4.43 in following section shows the analyses of SYSID parametric models after tested using the second approach i.e., recursive approach.

4.5.2 Analyses of recursive approach

Figure 4.39 shows the discrete model for coriolis mass flowrate developed using General Linear (GL) model. The model order used for A, B, C, D, F polynomials are 1, 3, 1, 2, 2, whilst the delay order used is 1, which are equal to model order and delay order predicted by GL model in non recursive section.

From the 'prediction error' part, the maximum error achieved is equal to 7, whilst the minimum error achieved is equal to 0. The average prediction error is equal to 0.0407.

The delay order '1' is highlighted by one '0' in the 'coefficient' part.

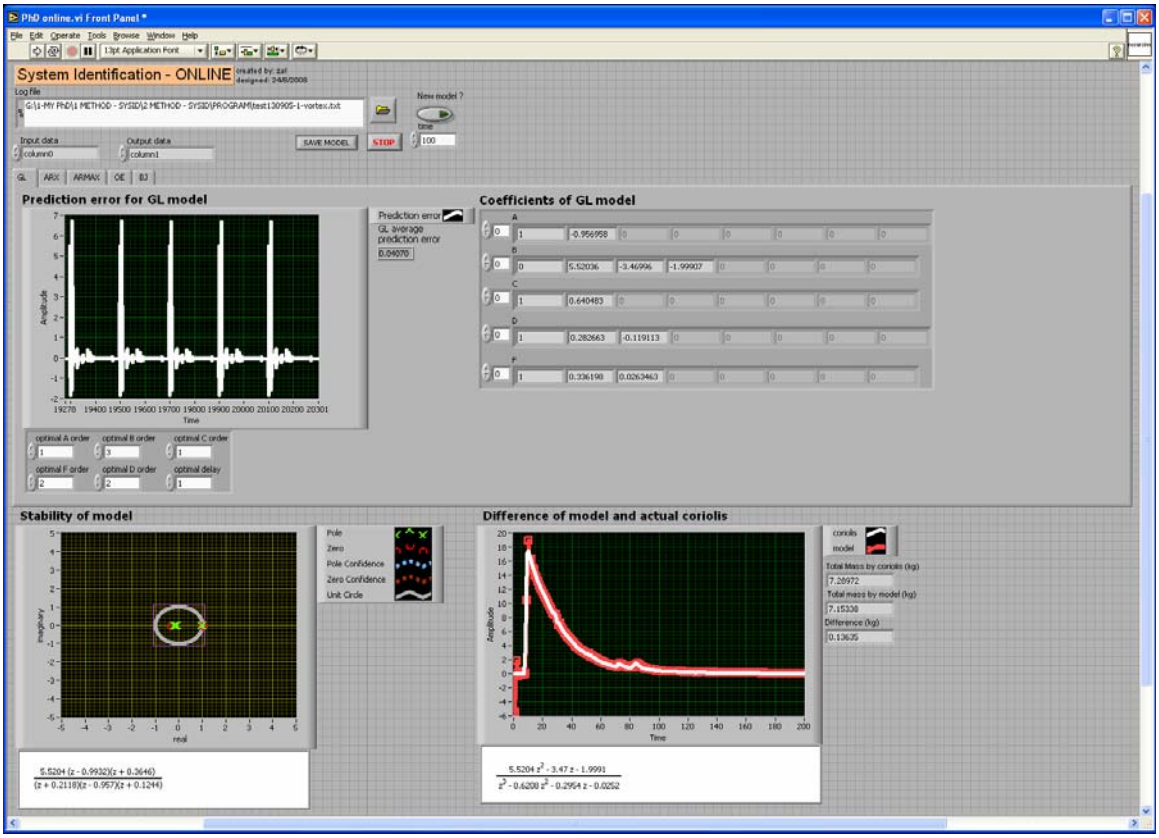

Figure 4.39: Discrete model of CMF using GL model

Based on Figure 4.39, the order and the unknown coefficients in polynomial function are

$$A(q) = 1 - 0.9570q^{-1} \tag{4.27}$$

$$B(q) = 5.5204q^{-1} - 3.4700q^{-2} - 1.9991q^{-3} \tag{4.28}$$

$$C(q) = 1 + 0.6405q^{-1} \tag{4.29}$$

$$D(q) = 1 + 0.2827q^{-1} - 0.1191q^{-2} \tag{4.30}$$

$$F(q) = 1 + 0.3362q^{-1} + 0.0263q^{-2} \tag{4.31}$$

Whilst, the zeroes-poles function could be represented as

$$\frac{5.5204(z - 0.9932)(z + 0.3646)}{(z + 0.2118)(z - 0.957)(z + 0.1244)} \tag{4.32}$$

As shown from the ‘stability’ part, all zeroes and poles are inside the unit circle which indicates the developed model is stable. In this section, the zeroes and poles are represented by red and green color, respectively.

The difference equation for the model could be represented as

$$\frac{5.5204z^2 - 3.47z - 1.9991}{z^3 - 0.6208z^2 - 0.2954z - 0.0252} \tag{4.33}$$

From the ‘difference’ part, the total mass measured by actual coriolis and GL models are 7.2897 kg and 7.1534 kg, respectively, whilst the difference is 0.1364 kg. Since, the GL model produces smaller difference, the graph developed by GL model overlaps the graph developed by actual coriolis, with a minor difference.

In this section, all developed models and actual coriolis are represented using red and white color, respectively. The following section discusses the second analysis of SYSID parametric models i.e., the Autoregressive Exogeneous Input (ARX) model.

Figure 4.40 shows the discrete model for coriolis mass flowrate developed using Autoregressive Exogeneous Input (ARX) model. The model order used for A, B polynomials are 1, 3 whilst the delay order used is 1, which are equal to model order and delay order predicted by ARX model in non recursive section.

From the 'prediction error' part, the maximum error achieved is equal to 7, whilst the minimum error achieved is equal to 0. The average prediction error is equal to 0.0546.

The delay order '1' is highlighted by one '0' in the 'coefficient' part.

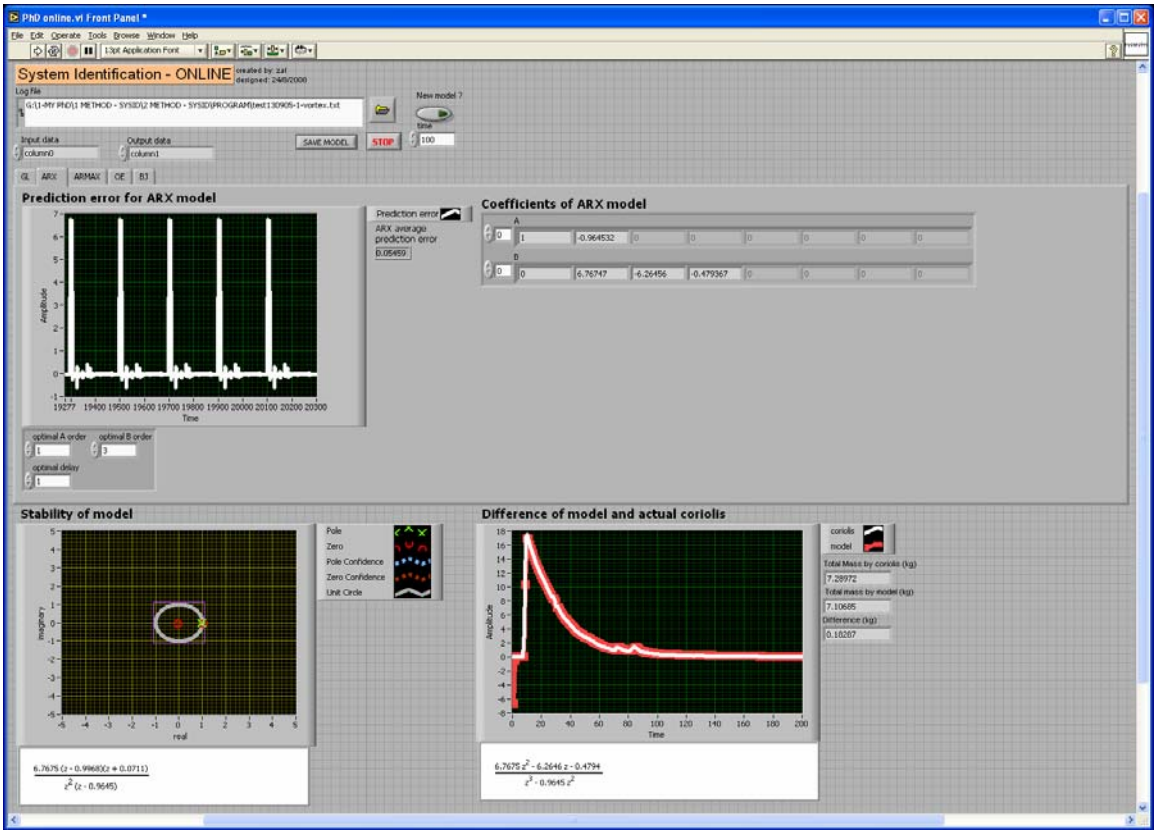

Figure 4.40: Discrete model of CMF using ARX model

Based on Figure 4.40, the order and the unknown coefficients in polynomial function are

$$A(q) = 1 - 0.9645q^{-1} \tag{4.34}$$

$$B(q) = 6.7675q^{-1} - 6.2646q^{-2} - 0.4794q^{-3} \tag{4.35}$$

Whilst, the zeroes-poles function could be represented as

$$\frac{6.7675(z - 0.9968)(z + 0.0711)}{z^2(z - 0.9645)} \tag{4.36}$$

As shown from the 'stability' part, all zeroes and poles are inside the unit circle which indicates the developed model is stable.

The difference equation for the model could be represented as

$$\frac{6.7675z^2 - 6.2646z - 0.4794}{z^3 - 0.9645z^2} \tag{4.37}$$

From the 'difference' part, the total mass measured by actual coriolis and ARX models are 7.2897 kg and 7.1069 kg, respectively, whilst the difference is 0.1829 kg. Since, the ARX models produces smaller difference, the graph developed by ARX model overlaps the graph developed by actual coriolis, with a minor difference.

The following section discusses the third analysis of SYSID parametric models i.e., the Autoregressive Moving Average with Exogeneous Input (ARMAX) model.

Figure 4.41 shows the discrete model for coriolis mass flowrate developed using Autoregressive Moving Average with Exogeneous Input (ARMAX) model. The model order used for A, B, C polynomials are 1, 3, 1 whilst the delay order used is 3, which are equal to model order and delay order predicted by ARMAX model in non recursive section.

From the 'prediction error' part, the maximum error achieved is equal to 12, whilst the minimum error achieved is equal to 0. The average prediction error is equal to 0.0614.

The delay order '3' is highlighted by three '0' in the 'coefficient' part.

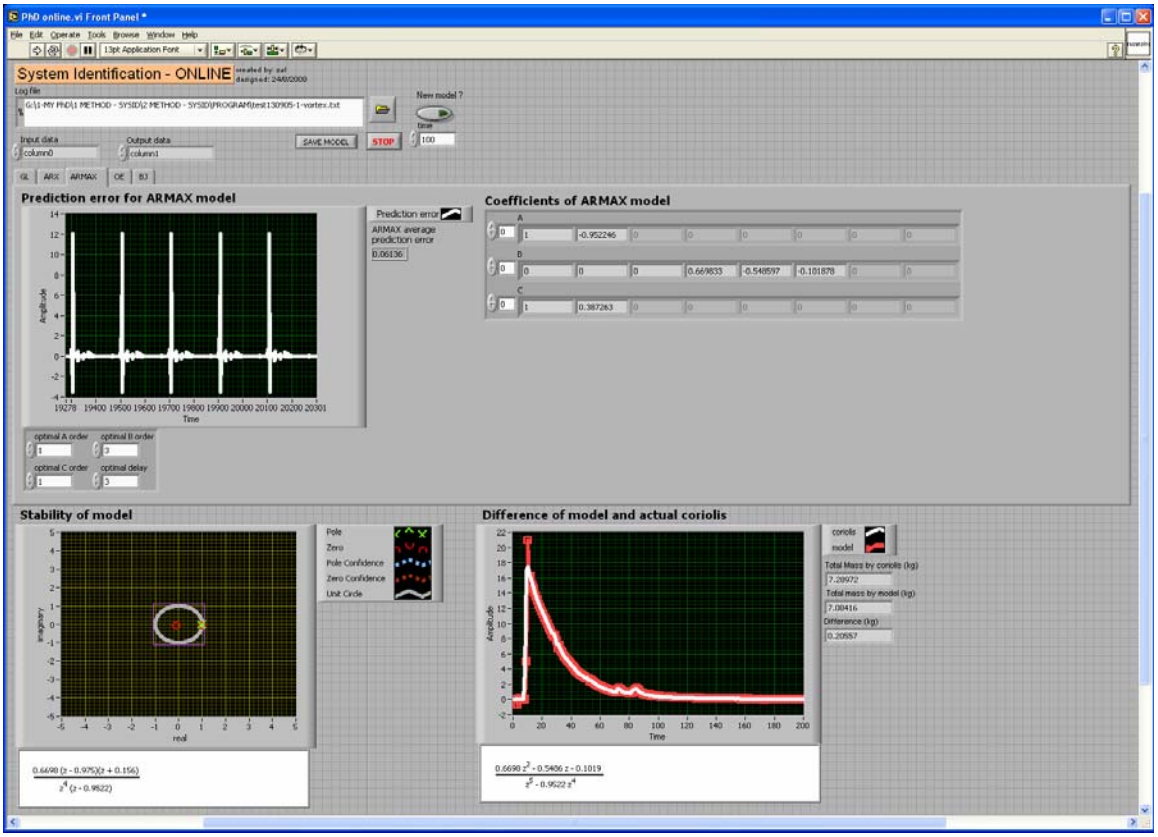

Figure 4.41: Discrete model of CMF using ARMAX model

Based on Figure 4.41, the order and the unknown coefficients in polynomial function are

$$A(q) = 1 - 0.9522q^{-1} \tag{4.38}$$

$$B(q) = 0.6698q^{-3} - 0.5486q^{-4} - 0.1019q^{-5} \tag{4.39}$$

$$C(q) = 1 - 0.3873q^{-1} \tag{4.40}$$

Whilst, the zeroes-poles function could be represented as

$$\frac{0.6698(z - 0.975)(z + 0.156)}{z^4(z - 0.9522)} \tag{4.41}$$

As shown from the ‘stability’ part, all zeroes and poles are inside the unit circle which indicates the developed model is boundedly stable.

The difference equation for the model could be represented as

$$\frac{0.6698z^2 - 0.5486z - 0.1019}{z^5 - 0.9522z^4} \tag{4.42}$$

From the ‘difference’ part, the total mass measured by actual coriolis and ARMAX models are 7.2897 kg and 7.0842 kg, respectively, whilst the difference is 0.2056 kg. Since, the ARMAX model produces smaller difference, the graph developed by ARMAX model overlaps the graph developed by actual coriolis, with a minor difference.

The following section discusses the fourth analysis of SYSID parametric models i.e., the Output Error (OE) model.

Figure 4.42 shows the discrete model for coriolis mass flowrate developed using Output Error (OE) model. The model order used for B, F polynomials are 6, 1 whilst the delay order used is 5, which are equal to model order and delay order predicted by OE model in non recursive section.

From the 'prediction error' part, the maximum error achieved is equal to 14, whilst the minimum error achieved is equal to 0. The average prediction error is equal to 1.3033.

The delay order '5' is highlighted by five '0' in the 'coefficient' part.

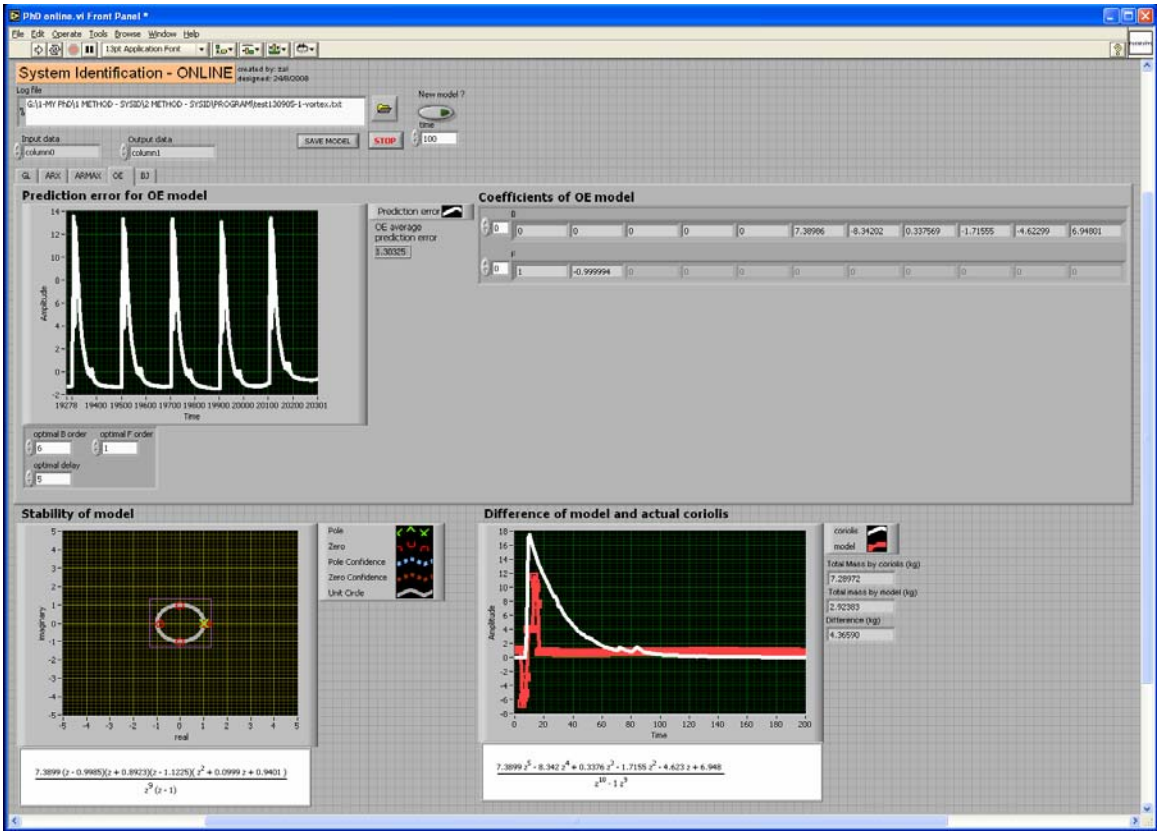

Figure 4.42: Discrete model of CMF using OE model

Based on Figure 4.42, the order and the unknown coefficients in polynomial function are

$$B(q) = 7.3899q^{-5} - 8.3420q^{-6} + 0.3376q^{-7} - 1.7156q^{-8} - 4.6230^{-9} + 6.9480q^{-10} \quad (4.43)$$

$$F(q) = 1 - 0.9999q^{-1} \quad (4.44)$$

Whilst, the zeroes-poles function could be represented as

$$\frac{7.3899(z - 0.9985)(z + 0.8923)(z - 1.1225)(z^2 + 0.0999z + 0.9401)}{z^9(z - 1)} \quad (4.45)$$

As shown from the 'stability' part, one of the zeroes is located outside from the unit circle which is at 1.1225. This indicates that the developed model is not stable.

The difference equation for the model could be represented as

$$\frac{7.3899z^5 - 8.342z^4 + 0.3376z^3 - 1.7155z^2 - 4.623z + 6.948}{z^{10} - 1z^9} \quad (4.46)$$

From the 'difference' part, the total mass measured by actual coriolis and OE models are 7.2897 kg and 2.9238 kg, respectively, whilst the difference is 4.3659 kg. Since, the OE model produces bigger difference, the graph developed by OE model doesn't overlap the graph developed by actual coriolis.

The following section discusses the fifth analysis of SYSID parametric models i.e., the Box Jenkins (BJ) model.

Figure 4.43 shows the discrete model for coriolis mass flowrate developed using Box Jenkins (BJ) model. The model order used for B, C, D, F polynomials are 4, 3, 1, 1 whilst the delay order used is 4, which are equal to model order and delay order predicted by OE model in non recursive section.

From the 'prediction error' part, the maximum error achieved is equal to 12, whilst the minimum error achieved is equal to 0. The average prediction error is equal to 0.0691.

The delay order '4' is highlighted by four '0' in the 'coefficient' part.

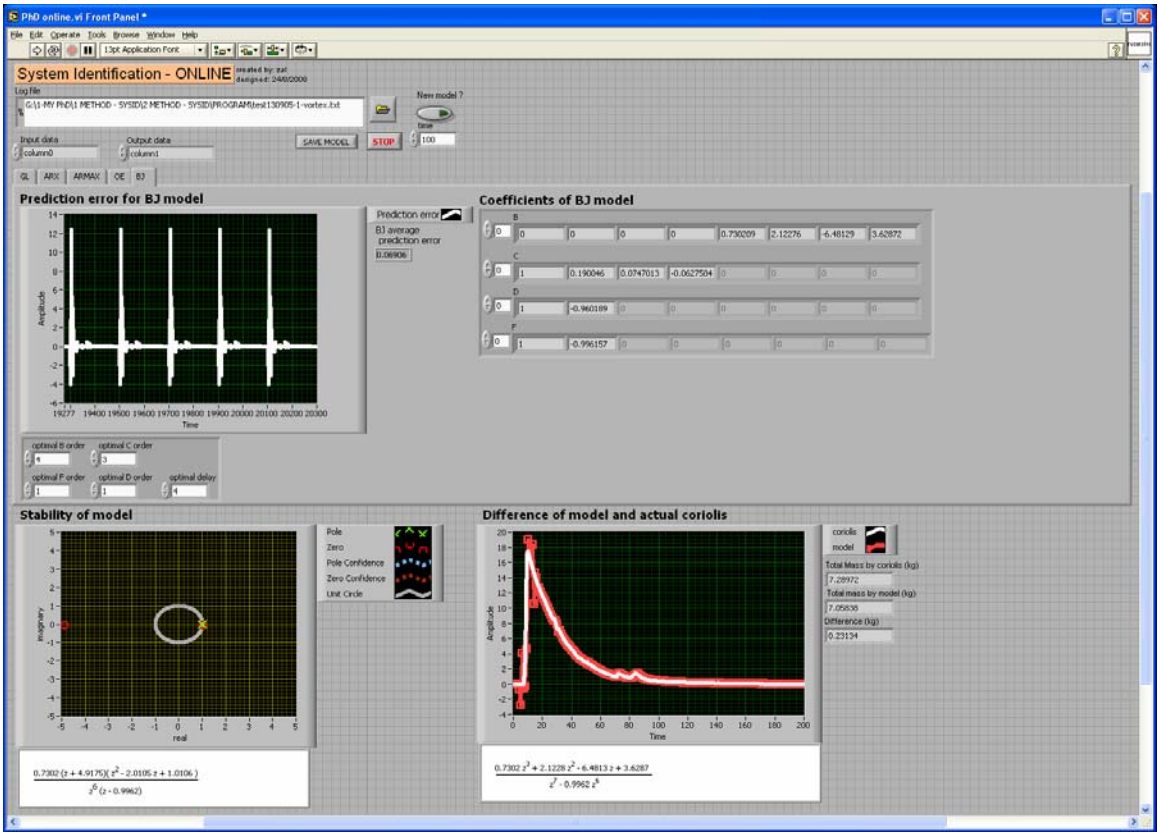

Figure 4.43: Discrete model of CMF using BJ model

Based on Figure 4.43, the order and the unknown coefficients in polynomial function are

$$B(q) = 0.7302q^{-4} + 2.1228q^{-5} - 6.4813q^{-6} + 3.6287q^{-7} \quad (4.47)$$

$$C(q) = 1 + 0.1900q^{-1} + 0.0747q^{-2} - 0.0628q^{-3} \quad (4.48)$$

$$D(q) = 1 - 0.9602q^{-1} \quad (4.49)$$

$$F(q) = 1 - 0.9962q^{-1} \quad (4.50)$$

Whilst, the zeroes-poles function could be represented as

$$\frac{0.7302(z + 4.9175)(z^2 - 2.0105z + 1.0106)}{z^6(z - 0.9962)} \quad (4.51)$$

As shown from the 'stability' part, one of the zeroes is located outside from the unit circle which is at -4.9175. This indicates that the developed model is not stable.

The difference equation for the model could be represented as

$$\frac{0.7302z^3 + 2.1228z^2 - 6.4813z + 3.6287}{z^7 - 0.9962z^6} \quad (4.52)$$

From the 'difference' part, the total mass measured by actual coriolis and BJ models are 7.2897 kg and 7.0584 kg, respectively, whilst the difference is 0.2313 kg. Since, the BJ model produces smaller difference, the graph developed by BJ model overlaps the graph developed by actual coriolis, with a minor difference.

Figure 4.39-4.43 in this section has shown the LabVIEW front panels to develop the discrete model for coriolis mass flowrate (CMF) based on the second approach which is non-recursive approach. Figure 4.44 in following section shows the analysis of SYSID model after tested using the third approach i.e., state space approach.

4.5.3 Analysis of state space approach

Figure 4.44 shows the discrete model for coriolis mass flowrate developed using the state space (SS) model. From the 'optimal order' part, the maximum singular value is equal to 180 which is located at order of 0, whilst the minimum singular values is equal to 0 which is located at order of 2, 3, 4, 5, 6, 7, 8 and 9.

The order would determine the minimum dimension of state vector $x(n)$ which would determine the number of unknown coefficients in matrix, *A*. As shown by the optimal order graph, order 0 and order 1 would be the impossible dimension, whilst order 3, 4, 5, 6, 7, 8 and 9 would increase the unknown coefficients to be determined in matrix, *A*.

Therefore, the possible option is order of 2 which is indicated by the first minimum singular values. This is also known as optimal order for dimension of state vector, $x(n)$ which is mentioned in Chapter 3.

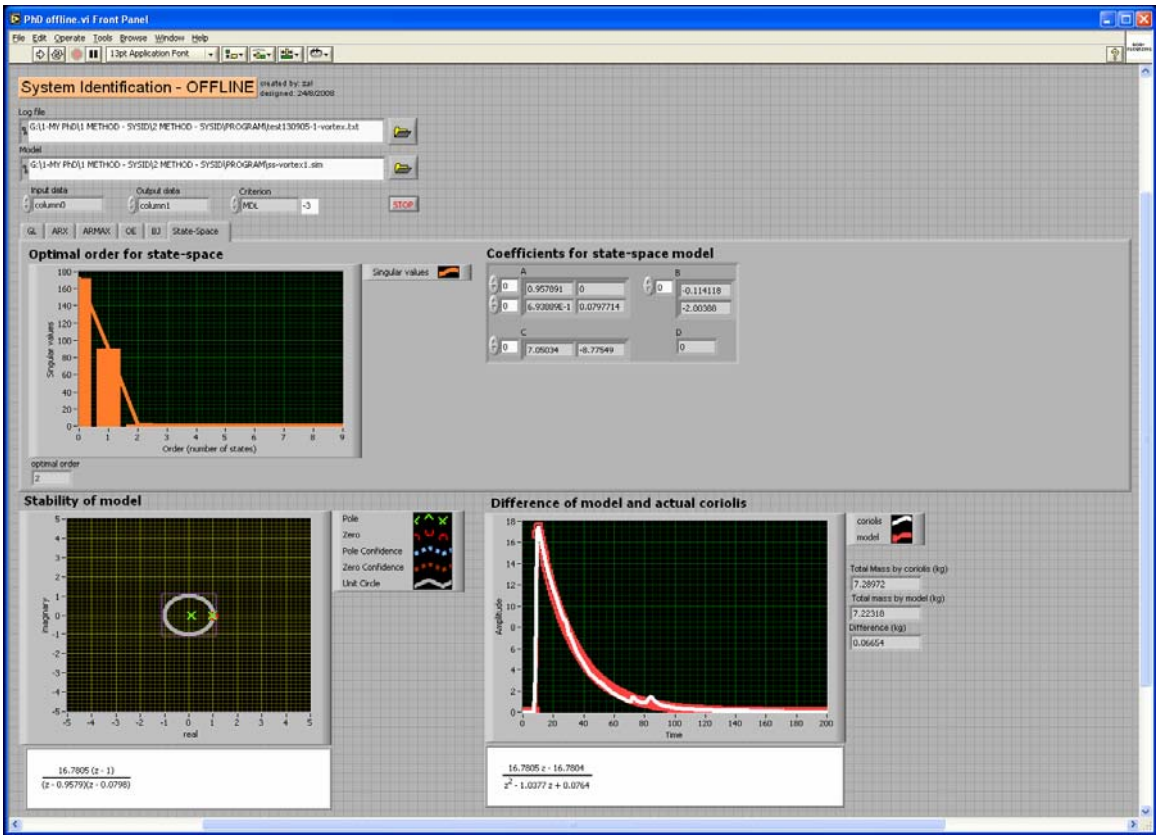

Figure 4.44: Discrete model of CMF using state space model

Based on Figure 4.44, the order and the unknown coefficients in system matrices are

$$A = \begin{bmatrix} 0.9579 & 0 \\ 0.6939 & 0.0798 \end{bmatrix} \qquad B = \begin{bmatrix} -0.1141 \\ -2.0039 \end{bmatrix}$$

$$C = \begin{bmatrix} 7.0503 & -8.7755 \end{bmatrix} \qquad D = \begin{bmatrix} 0 \end{bmatrix} \tag{4.53}$$

Whilst, the zeroes-poles function could be represented as

$$\frac{16.7805(z-1)}{(z-0.9579)(z-0.0798)} \tag{4.54}$$

As shown from the ‘stability’ part, all zeroes and poles are inside the unit circle which indicates the developed model is stable. In this section, the zeroes and poles are represented by red and green color, respectively.

The difference equation for the model could be represented as

$$\frac{16.7805z - 16.7804}{z^2 - 1.0377z + 0.0764} \tag{4.55}$$

From the ‘difference’ part, the total mass measured by actual coriolis and state space models are 7.2897 kg and 7.2232 kg, respectively, whilst the difference is 0.0665 kg. Since, the state space model produces smaller difference, the graph developed by state space model overlaps the graph developed by actual coriolis, with a minor difference. The state space model and actual coriolis are represented using red and white color, respectively.

This section has shown the LabVIEW front panels to develop the discrete model for coriolis mass flowrate (CMF) based on third approach which is the state space approach. Table 4.3 in following section shows table of comparison for all discrete models of CMF that have been developed using non recursive, recursive and state space approach. The purpose of the comparison is to choose a stable discrete model of CMF that has minimum difference of error compared to actual coriolis.

Table 4.3: Table of comparison for discrete model of coriolis mass flowrate (CMF) developed by non-recursive, recursive and state-space approach

Type	**Model**	**Zeroes-poles equation**	**Difference equation**	**Stability**	**Difference of total mass between discrete model of CMF and actual coriolis (kg)**
Non-recursive	GL	$\frac{14.0453(z-1.0002)(z+0.2241)}{(z-0.0192)(z-0.9583)(z+0.1735)}$	$\frac{14.0453z^2-10.9006z-3.1474}{z^3-0.8339z^2-0.1513z+0.0032}$	Stable	1.48461
	ARX	$\frac{13.4677(z-1)(z+0.0804)}{z^2(z-0.9584)}$	$\frac{13.4677z^2-12.3851z-1.0834}{z^3-0.9584z^2}$	Stable	1.51374
	ARMAX	$\frac{-0.112(z-1.0101)(z-0.3583)}{z^4(z-0.9581)}$	$\frac{-0.112z^2+0.1532z-0.0405}{z^5-0.9581z^4}$	Stable	7.27015
	OE	$\frac{-0.035(z-1.0094)(z+0.0165)(z-3.0829)(z^2+1.1185z+0.6569)}{z^9(z-0.9584)}$	$\frac{-0.035z^5+0.1036z^4+0.0301z^3-0.0273z^2-0.0721z-0.0012}{z^{10}-0.9584z^9}$	Not Stable	7.33206
	BJ	$\frac{0.0409(z-0.9948)(z^2-0.7816z+1.7473)}{z^6(z-0.9436)}$	$\frac{0.0409z^3-0.0726z^2+0.1033z-0.0711}{z^7-0.9436z^6}$	Not stable	7.24487
Recursive	GL	$\frac{5.5204(z-0.9932)(z+0.3646)}{(z+0.2118)(z-0.957)(z+01244)}$	$\frac{5.5204z^2-3.47z-1.9991}{z^3-0.6208z^2-0.2954z-0.0252}$	Stable	0.13635
	ARX	$\frac{6.7675(z-0.9968)(z+0.0711)}{z^2(z-0.9645)}$	$\frac{6.7675z^2-6.2646z-0.4794}{z^3-0.9645z^2}$	Stable	0.18287
	ARMAX	$\frac{0.6698(z-0.975)(z+0.156)}{z^4(z-0.9522)}$	$\frac{0.6698z^2-0.5486z-0.1019}{z^5-0.9522z^4}$	Stable	0.20557
	OE	$\frac{7.3899(z-0.9985)(z+0.8923)(z-1.1225)(z^2+0.0999z+0.9401)}{z^9(z-1)}$	$\frac{7.3899z^5-8.342z^4+0.3376z^3-1.7155z^2-4.623z+6.948}{z^{10}-1z^9}$	Not stable	4.36590
	BJ	$\frac{0.7302(z+4.9175)(z^2-2.0105z+1.0106)}{z^6(z-0.9962)}$	$\frac{0.7302z^3+2.1228z^2-6.4813z+3.6287}{z^7-0.9962z^6}$	Not stable	0.23134
State-space		$\frac{16.7805(z-1)}{(z-0.9579)(z-0.0798)}$	$\frac{16.7805z-16.7804}{z^2-1.0377z+0.0764}$	Stable	0.06654

4.5.4 Analysis of comparison for discrete model of CMF

Based on Table 4.3, a comparison is made based on stability and difference of total mass between coriolis mass flowrate (CMF) models and actual coriolis. For the non recursive models, GL, ARX, ARMAX, look stable, but OE and BJ model are not. Whilst, from the difference point of view, only GL model could present the actual coriolis accurately in which the minimum difference produced by GL is 1.4846 kg, respectively. For the recursive models, GL, ARX, ARMAX are considered stable, but OE and BJ are not. Whilst, from the difference point of view, only GL model could present the actual coriolis in which the minimum difference is 0.1364 kg. However, if difference from GL model is compared with difference from state space model, the minimum difference is the state space model in which the minimum difference is 0.0665 kg, respectively.

Since the difference is compared at final mass of measurement, further analysis is needed to compare discrete values of coriolis mass flowrate (CMF) models at each sampling time. For that reason, a method known as power series expansion is used to calculate the discrete values of CMF models which are non recursive, recursive and state space models, respectively. Please refer Chapter 3 for detail descriptions on power series expansion. The following calculation shows a typical example using state space model.

	16.7805**z-1**	+17.4132**z-2**	+16.7877**z-3**	+16.0903**z-4**	+	
z3-2.0377**z2** +1.1141**z**-0.0764	16.7805**z2**	-16.7804**z**				
	16.7805**z2**	-34.1936**z**	+18.6952	-1.2820**z-1**		
		17.4132**z**	-18.6952	+1.2820**z-1**		
		17.4132**z**	-35.4829	+19.4000**z-1**	-1.3304**z-2**	
			16.7877	-18.1180**z-1**	+1.3304**z-2**	
			16.7877	34.2083**z-1**	+18.7032**z-2**	-1.2826**z-3**
				16.0903**z-1**	-17.3728**z-2**	+1.2826**z-3**

Notably, an infinite series of discrete CMF values could be predicted at the quotient part or from the result of the division. In view of the fact that power series expansion is lengthy and consumes more time, a better option is to develop a computer program to generate the infinite series of discrete CMF values based on power series expansion algorithm. Figure 4.45-4.46 in following section shows a MATLAB Simulink program to calculate the power series expansion and sample of discrete values that have been generated for non recursive, recursive and state space models, respectively.

Figure 4.45 shows a MATLAB Simulink program to calculate the power series expansion using difference equations of non recursive, recursive and state space models. Results of discrete coriolis mass flowrate (CMF) values are stored in 'simout1' variable which are shown in following section as Figure 4.46, respectively.

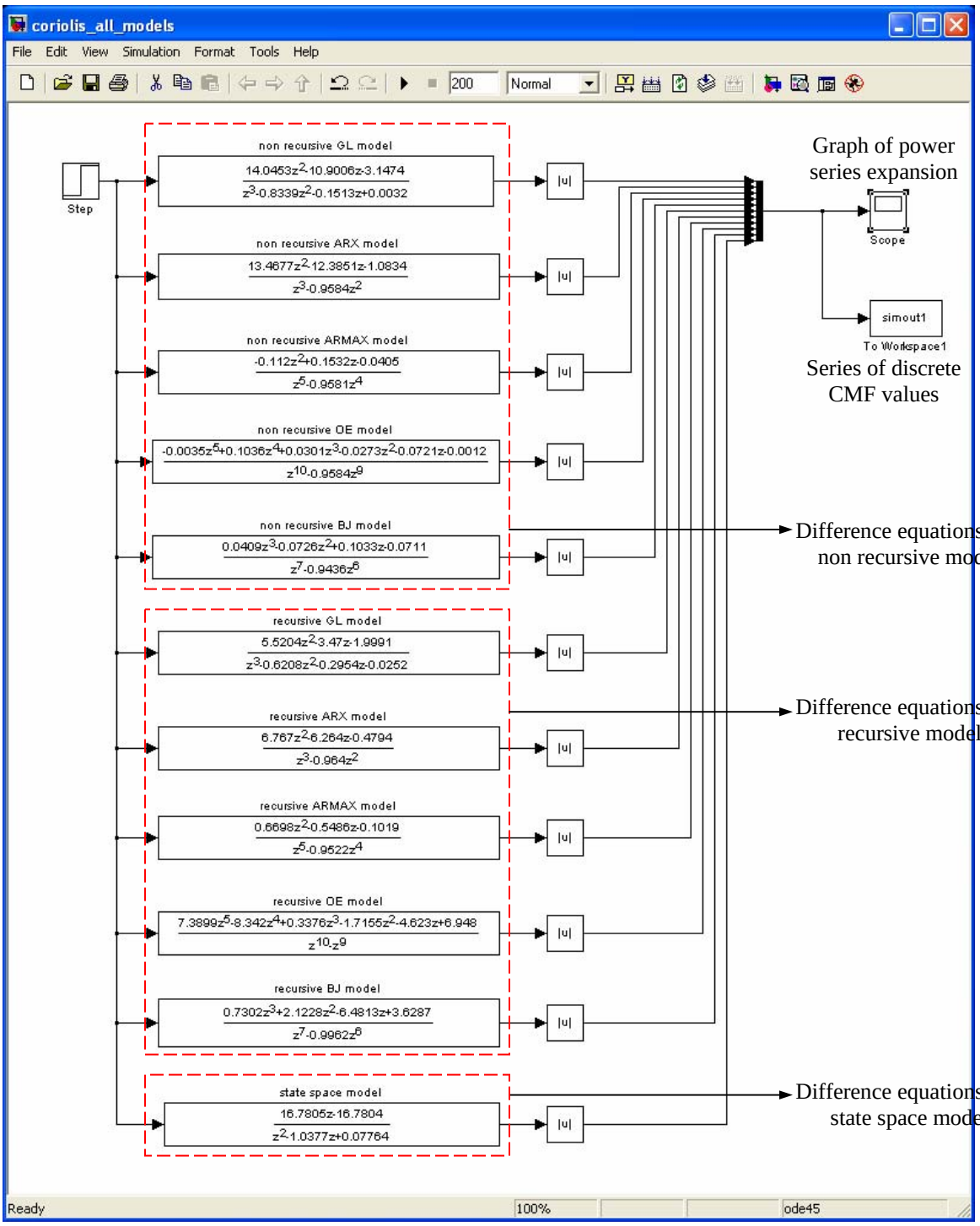

Figure 4.45: MATLAB Simulink program to calculate discrete CMF values

Figure 4.46 shows discrete coriolis mass flowrate (CMF) values which are generated by the 'simout1' variable from the MATLAB Simulink program, whilst, Table 4.4 shows type of discrete CMF values for non recursive, recursive and state space models at each column, respectively.

Table 4.4: Types of discrete values at each column

Column	Type of discrete values
1	Non recursive GL model
2	Non recursive ARX model
3	Non recursive ARMAX model
4	Non recursive OE model
5	Non recursive BJ model
6	Recursive GL model
7	Recursive ARX model
8	Recursive ARMAX model
8	Recursive OE model
10	Recursive BJ model
11	State space model

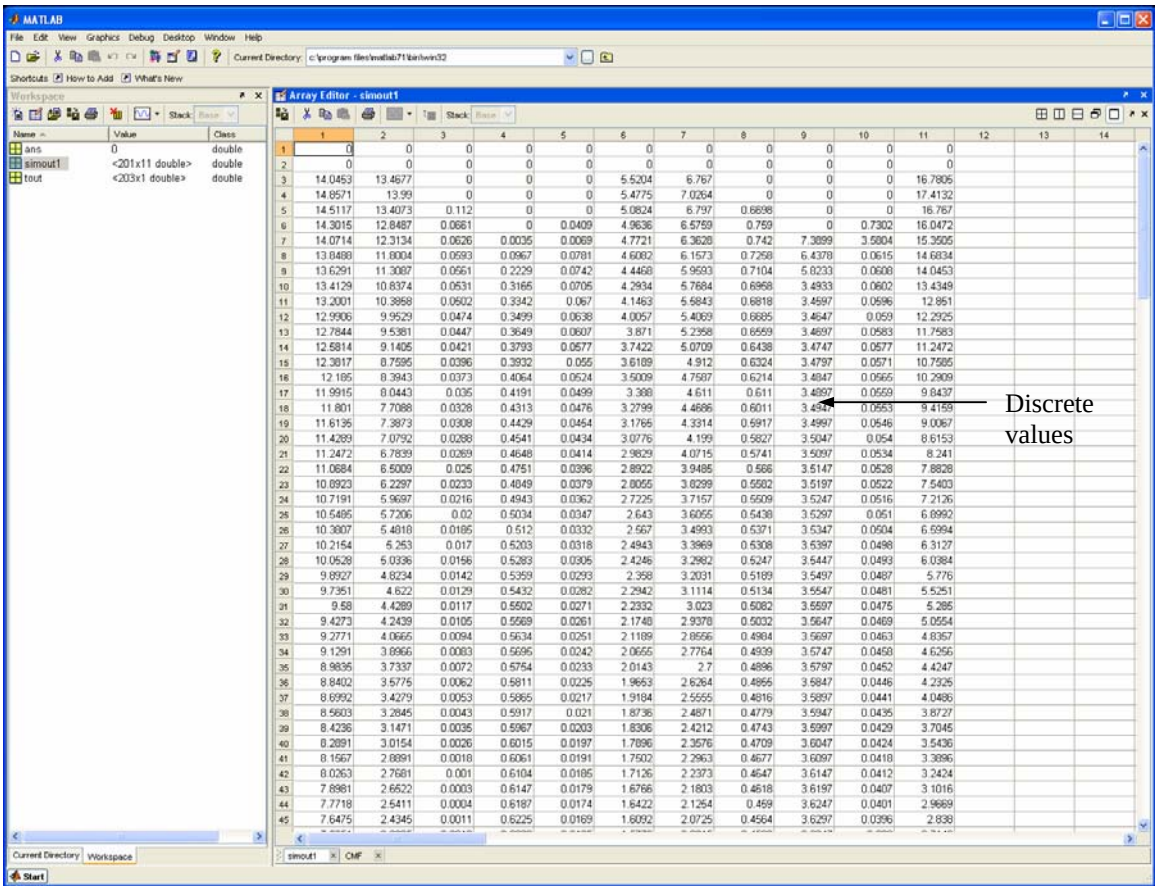

Figure 4.46: Discrete values generated from MATLAB Simulink program

Based on Figure 4.46, a comparison is made with coriolis data chosen at the low bank refueling region (similar data used in section 4.5.1-4.5.3) to determine discrete model of coriolis mass flowrate (CMF). Figure 4.47 shows a comparison of sample data between Figure 4.46 and coriolis data at low bank refueling region, respectively.

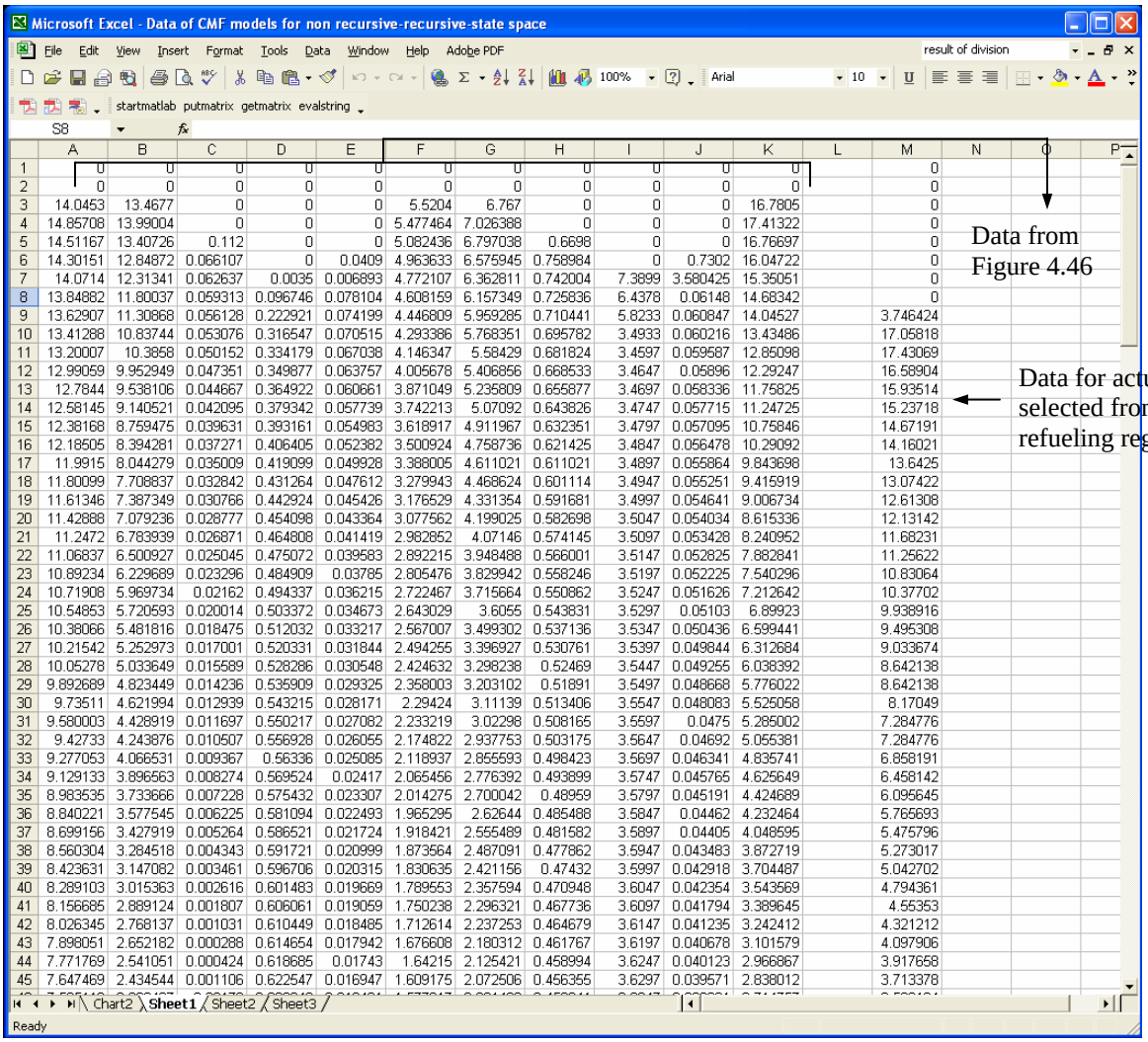

Figure 4.47: Sample of data to compare CMF values and actual coriolis

Notably, there are sequences of zeroes at initial stage of the sample data which indicate delays of measurements. By removing such delays and plotting back the data in graph, a comparison could be made at each sampling time. Figure 4.48 in following section shows graph of comparison between all CMF models and actual coriolis at each sampling time, respectively.

Figure 4.48 shows graph of comparison between coriolis mass flowrate (CMF) models and actual coriolis, respectively. Notably, there are two models that follow actual coriolis which are non recursive ARX and state space model. However, at each sampling time, only state space model could follow actual coriolis with a minimum difference of error.

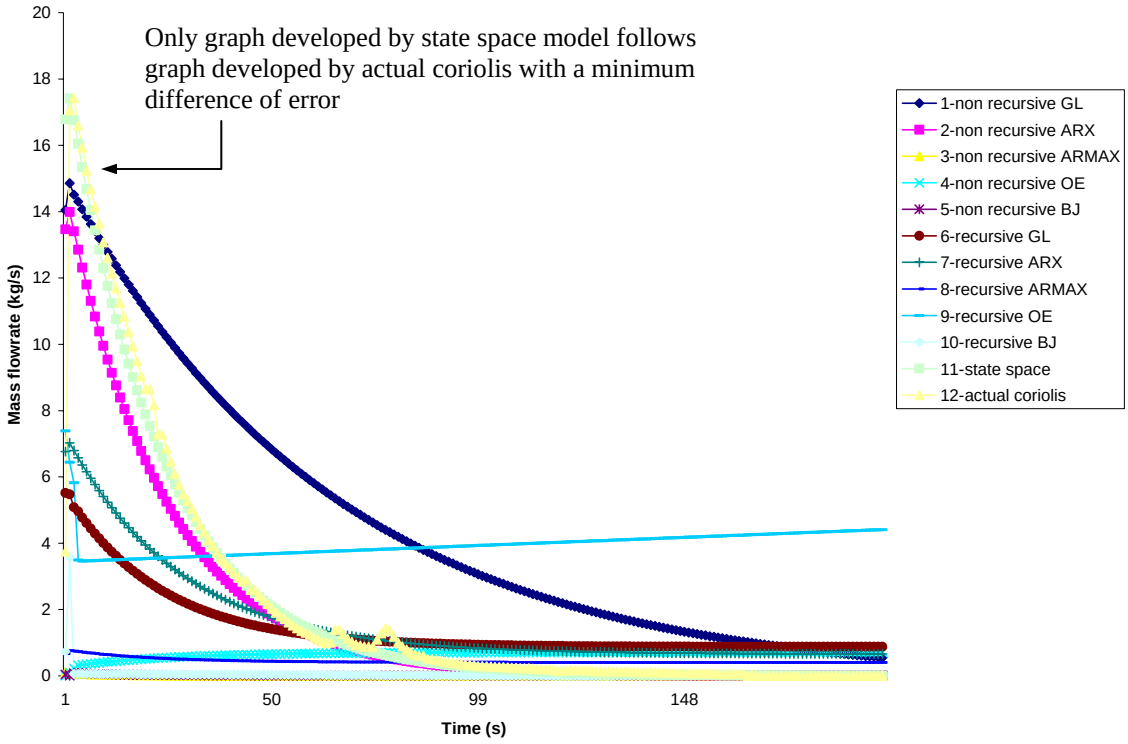

Figure 4.48: Graphs of comparison between all CMF models and actual coriolis

The analysis has shown that potential for state-space model to provide a more complete representation for actual coriolis as compared to other CMF models. As proposed by [249], this is due to its identification procedure i.e., N4SID algorithm does not involve in nonlinear optimization and hence the estimation reaches a solution regardless of the initial guess. By comparison, the parameter settings for the state-space model are simpler because it only involves selection of the appropriate order or the number of states model. The order can come from prior knowledge of the system or from the singular values of the information matrix, A. Since, the state space model is stable and produces minimum difference of error; it would represent the actual flowmeter system tested in this research, in which, the Micro Motion flowmeter. Based on the difference equation of state space model, the following section would discuss on developing inferential coriolis algorithm.

4.6 Develop algorithm for inferential coriolis model

The following section discusses the final steps of SYSID methodology i.e., develop algorithm for inferential coriolis model. Theoretically, the algorithm is made by finding a suitable trend line for non linear curve developed by discrete values of state space model and sensors values from the test rig, respectively. The trend line and non linear curve could be illustrated using a conceptual curve as shown in Figure 4.49, respectively.

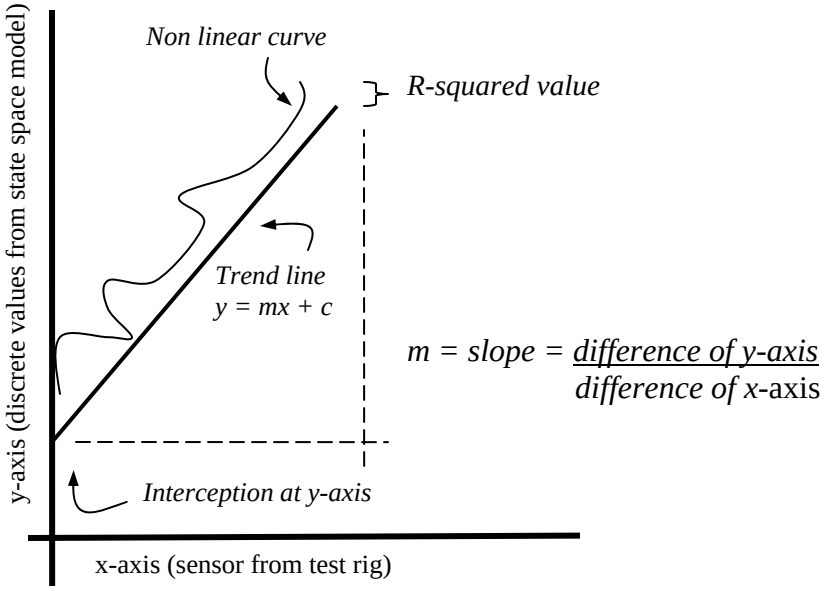

Figure 4.49: Trend line and conceptual curve

From the trend line, a relationship function could be designed based on R-squared (R^2) analysis. A trend line is actually a graphic representation of trends for data series, whilst the R-squared value is an indicator from 0 to 1 that reveals how closely the estimated values for the trend line correspond to the non linear curve. A trend line is most reliable when its R-squared value is equal or closer to 1 i.e., also known as coefficient of determination. Therefore, an assumption could be made that, if the trend line is 'completely' reliable, then the R-squared value would be equal to 1, which means the formula of the trend line is equal to a straight line curve i.e., $y = mx + c$. The value of y and x assumed here would present an equation or an inferential value for mass flowrate and sensor as an input, respectively. Whilst, m and c are slope and interception value also known as inferential coriolis parameters. The following section would discuss on inferential coriolis parameters based on various types of trend lines.

4.6.1 Designing trend line

In this research, equation of trend line, R-squared value and inferential coriolis parameters would be developed using a trend line program available in Microsoft Excel 2002 software. Figure 4.50 shows part of the trend line program which could be divided into two parts: option of trend lines and type of trend lines, respectively.

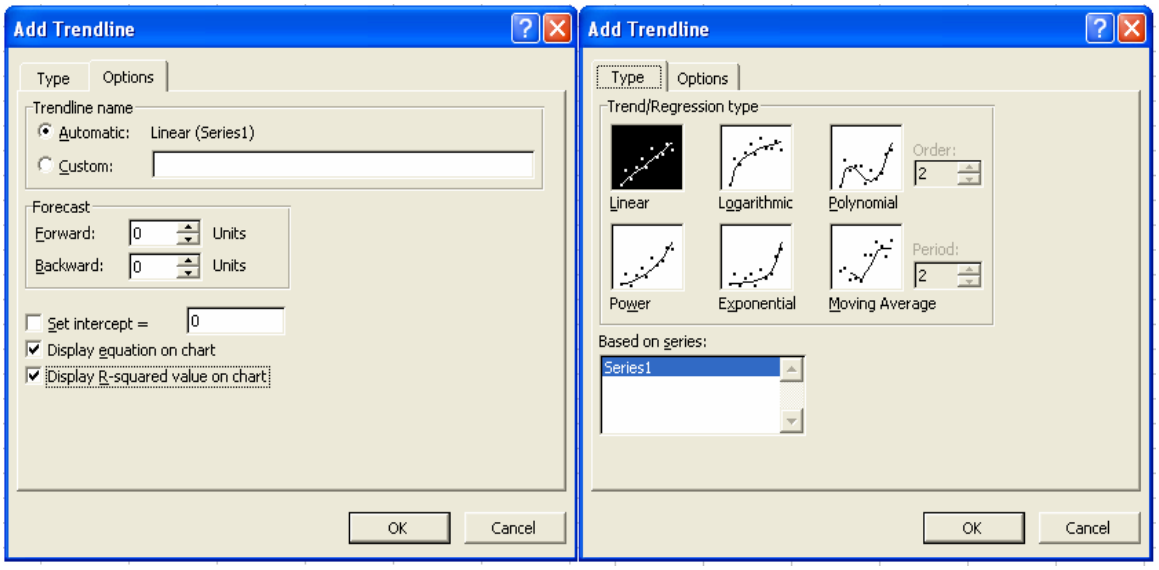

Figure 4.50: Trend line

Based on Figure 4.50, the option of trend line is to display the equation of trend line and the R-squared value, whilst type of trend lines is to select type of trend analysis such as linear, logarithmic, polynomial, power, exponential or moving average analysis, respectively. Since, logarithmic, power and exponential could not analyze negative trends, only linear and polynomial would be used in designing the trend lines, whilst, moving average is not applied here because it only presents a sequence of averages computed from parts of data series.

The following section discusses on designing trend line based on data stored in the FieldPoint as shown by Figure 4.22 and Table 4.2, respectively. Based on Table 4.2, there are 19 sensors in the test rig, but only pressure and temperature sensors at receiver and flow metering systems (PCYLN, TCYLN, PT, TT) could be used in designing trend line since the sensors give direct measurement to CNG refueling process.

Figure 4.51 shows an example of nonlinear curve for pressure sensor at receiver system (PCYLN) known as 'SS-PCYLN'. The curve is developed using pressure difference at receiver and discrete values from state space (SS) as x-axis and y-axis, respectively. In this design, the linear and polynomial trend lines are represented in red and green color, respectively.

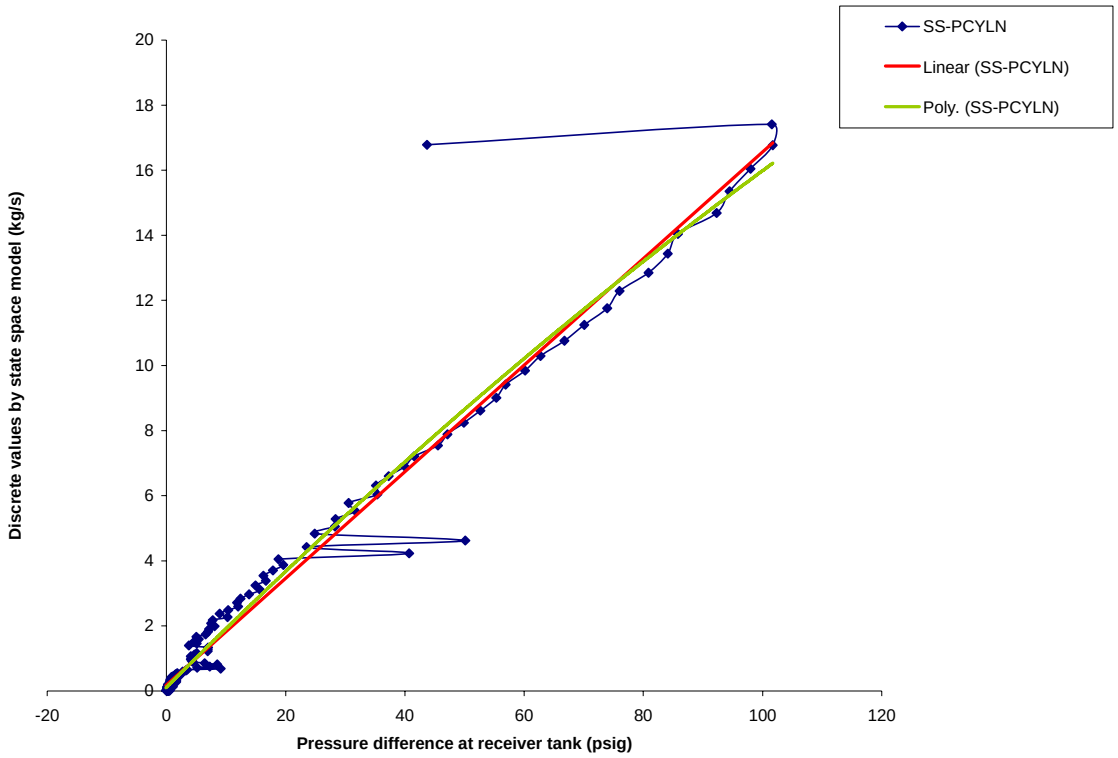

Figure 4.51: Non linear curve and trend lines for SS-PCYLN

Table 4.5: R-squared value for SS-PCYLN

Trend line	Equation	R-squared
Polynomial	$y = -0.0002x^2 + 0.1827x + 0.115$	0.9567
Linear	$y = 0.1637x + 0.1902$	0.9553

From Table 4.5, since both R-squared values are closed to 1, it shows that both trend lines have 'completely' reliable relationships with PCYLN sensor and state space model. Further analysis on trend line relationship is discussed using temperature sensor at receiver system (TCYLN).

Figure 4.52 shows an example of nonlinear curve for temperature sensor at receiver system (PCYLN) known as 'SS-TCYLN'. The curve is developed using temperature difference at receiver and discrete values from state space (SS) as x-axis and y-axis, respectively.

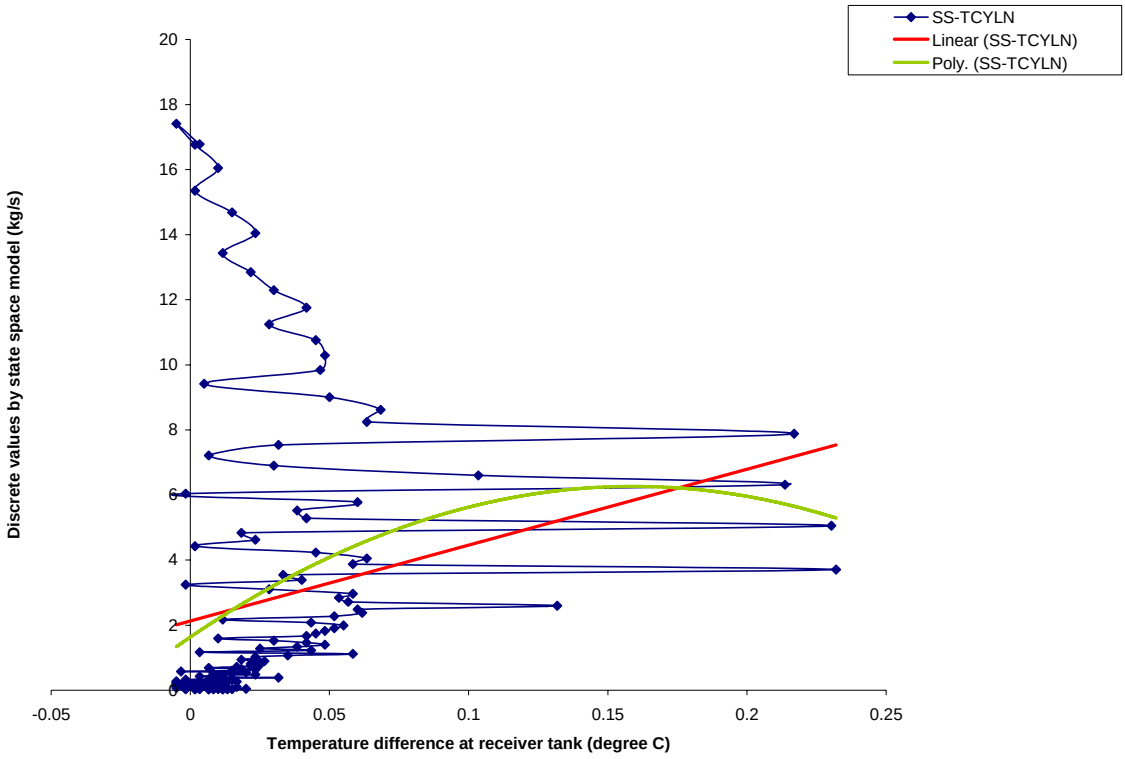

Figure 4.52: Non linear curve and trend lines for SS-TCYLN

Table 4.6: R-squared value for SS-TCYLN

Trend line	Equation	R-squared
Polynomial	$y = -183.08x^2 + 58.257x + 1.6301$	0.0641
Linear	$y = 23.32x + 2.1292$	0.046

From Table 4.6, since both R-squared values are closed to zero, it shows that both trend lines have non reliable relationships with TCYLN sensor and state space model. Further analysis on trend line relationship is discussed using pressure sensor at inlet of the flow metering system (PT1).

Figure 4.53 shows an example of nonlinear curve for pressure sensor at inlet of flow metering system (PT1) known as 'SS-PT1'. The curve is developed using inlet pressure difference and discrete values from state space (SS) as x-axis and y-axis, respectively.

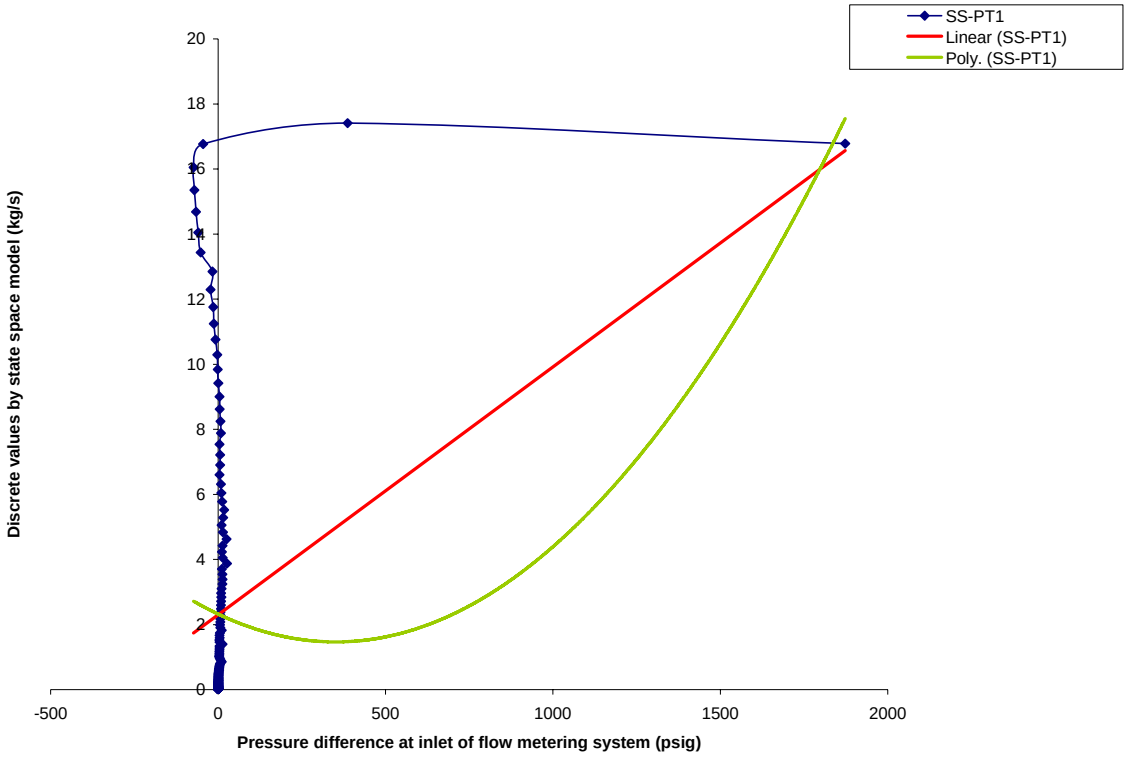

Figure 4.53: Non linear curve and trend lines for SS-PT1

Table 4.7: R-squared value for SS-PT1

Trend line	Equation	R-squared
Polynomial	$y = 7\times10^{-6}x^2 - 0.0049x + 2.3217$	0.0805
Linear	$y = 0.0076x + 2.2987$	0.0735

From Table 4.7, since both R-squared values are closed to zero, it shows that both trend lines have non reliable relationships with PT1 sensor and state space model. Further analysis on trend line relationship is discussed using temperature sensor at inlet of the flow metering system (TT1).

Figure 4.54 shows an example of nonlinear curve for temperature sensor at inlet of flow metering system (PT1) known as 'SS-TT1'. The curve is developed using inlet temperature difference and discrete values from state space (SS) as x-axis and y-axis, respectively.

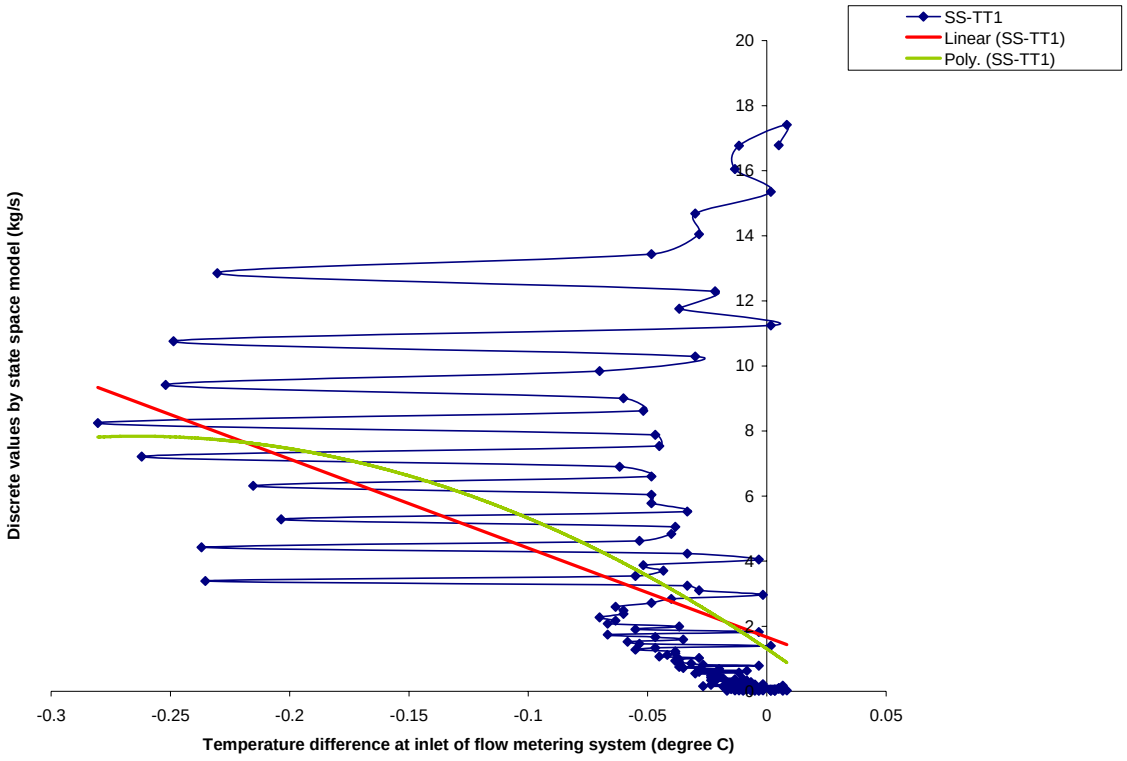

Figure 4.54: Non linear curve and trend lines for SS-TT1

Table 4.8: R-squared value for SS-TT1

Trend line	Equation	R-squared
Polynomial	$y = -93.873x^2 - 49.536x + 1.305$	0.1356
Linear	$y = -27.361x + 1.6651$	0.1272

From Table 4.8, since both R-squared values are closed to zero, it shows that both trend lines have non reliable relationships with TT1 sensor and state space model. Further analysis on trend line equation is discussed using pressure sensor at outlet of the flow metering system (PT2).

Figure 4.55 shows an example of nonlinear curve for pressure sensor at outlet of flow metering system (PT2) known as 'SS-PT2'. The curve is developed using outlet pressure difference and discrete values from state space (SS) as x-axis and y-axis, respectively.

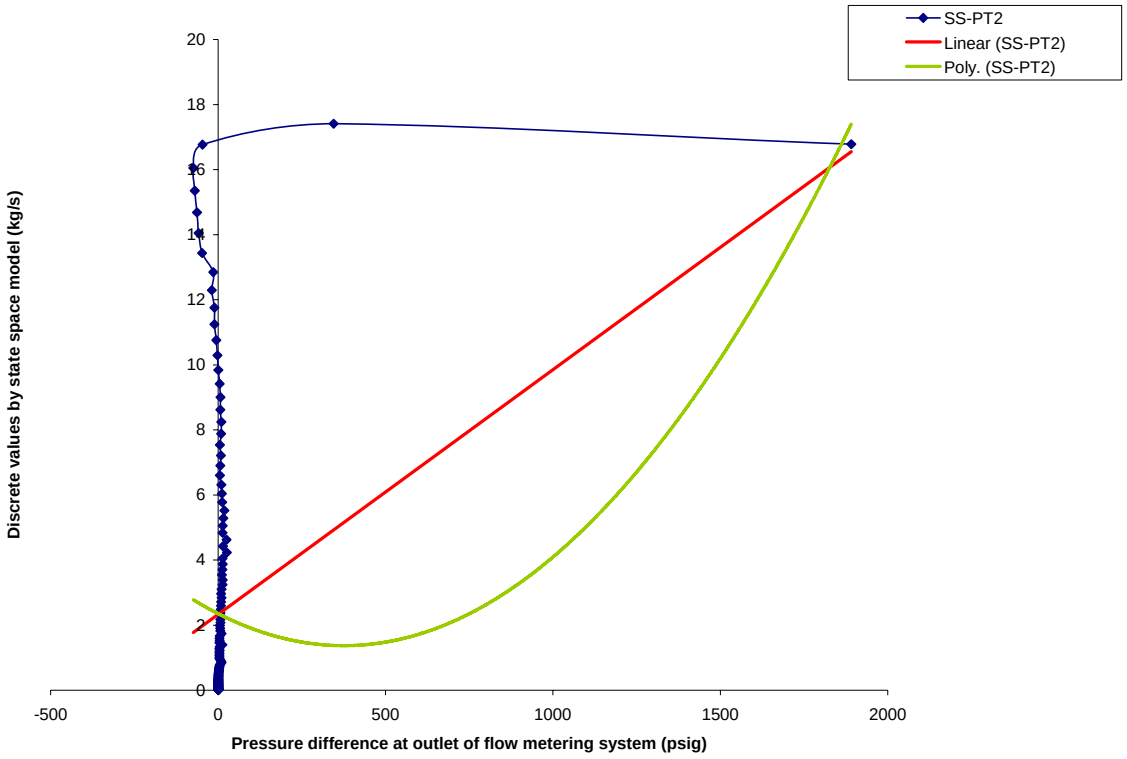

Figure 4.55: Non linear curve and trend lines for SS-PT2

Table 4.9: R-squared value for SS-PT2

Trend line	Equation	R-squared
Polynomial	$y = 7\times10^{-6}x^2 - 0.0052x + 2.3522$	0.0791
Linear	$y = 0.0075x + 2.3251$	0.0727

From Table 4.9, since both R-squared values are closed to zero, it shows that both trend lines have non reliable relationships with PT2 sensor and state space model. Further analysis on trend line equation is discussed using temperature sensor at outlet of the flow metering system (TT2).

Figure 4.56 shows an example of nonlinear curve for temperature sensor at outlet of flow metering system (TT2) known as 'SS-TT2'. The curve is developed using outlet temperature difference and discrete values from state space (SS) as x-axis and y-axis, respectively.

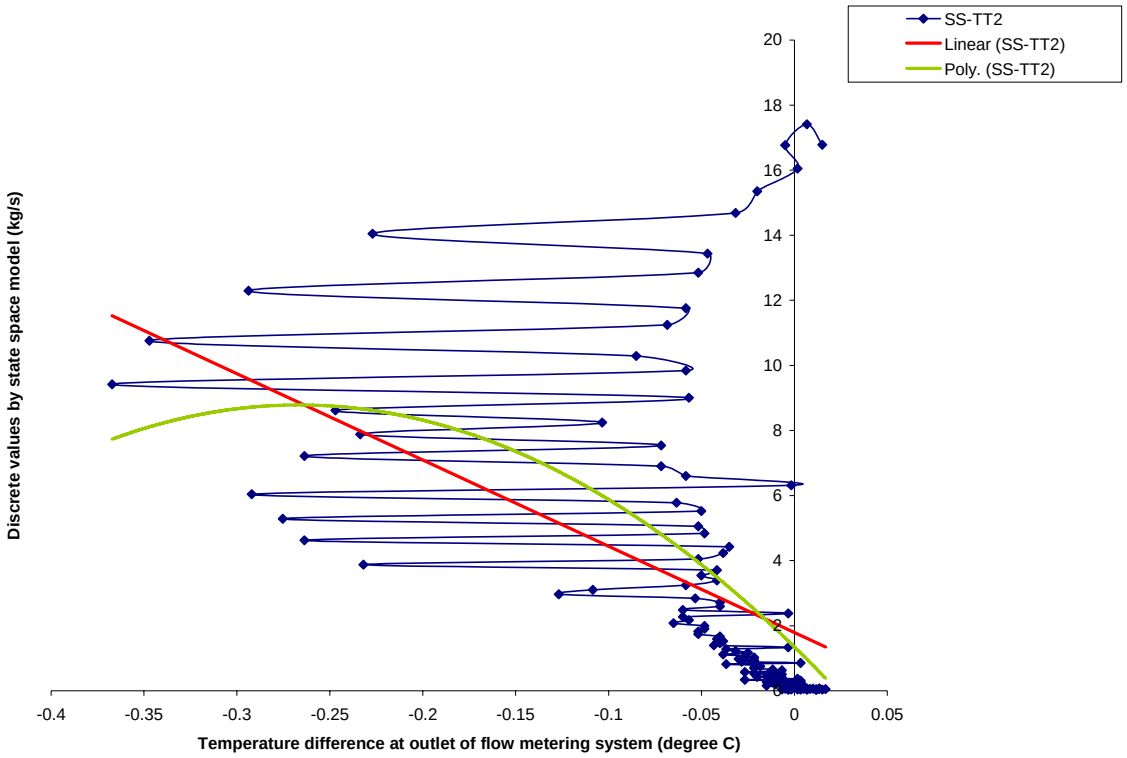

Figure 4.56: Non linear curve and trend lines for SS-TT2

Table 4.10: R-squared value for SS-TT2

Trend line	Equation	R-squared
Polynomial	$y = -104.48x^2 - 55.753x + 1.346$	0.2342
Linear	$y = -26.514x + 1.791$	0.2058

From Table 4.10, since both R-squared values are closed to zero, it shows that both trend lines have non reliable relationships with TT2 sensor and state space model. From this section, a table of comparison is made in following section to determine a suitable trend line for inferential coriolis equation and respective sensor input.

4.6.2 Identifying trend line

Table 4.11 shows table of comparison for R-squared values based on Figure 4.51-4.56 which are 'SS-PCYLN', 'SS-TCYLN', 'SS-PT1', 'SS-TT1', 'SS-PT2' and 'SS-TT2' i.e., non linear curve and trend line for determining inferential coriolis equation, respectively.

Table 4.11: Table of comparison for R-squared value

		Sensor					
		PCYLN	TCYLN	PT1	TT1	PT2	TT2
Trend line	Linear	0.9533	0.046	0.0735	0.1272	0.0727	0.2058
	Polynomial	0.9567	0.0641	0.0805	0.1356	0.0791	0.2342
	AVERAGE	0.9550	0.0551	0.0770	0.1314	0.0759	0.2200

Based on Table 4.11, the smallest R-squared value is 0.046 which is represented by linear trend line, whilst the highest R-squared value is 0.9567 which is represented by polynomial trend line. Since the highest R-squared value is produced by the polynomial trend line, the respective equation is chosen to represent inferential coriolis equation, whilst the suitable sensor to be used is PCYLN sensor. As mentioned earlier, the values of y, x and other constants are values for inferential value of mass flowrate, sensor input and inferential coriolis parameters, respectively. Notice that, the average of R-squared value developed by the PCYLN sensor is closer to 1, which is 0.9550. The value reveals how closely the sensor corresponds to inferential coriolis measurement.

In this section, a suitable trend line for inferential coriolis equation has been identified which is polynomial trend line. Further analysis is discussed in following section to identify suitable order of the polynomial trend line.

Figure 4.57 shows a 2nd order polynomial trend line for Figure 4.51. When, the order is increased to 2nd order, the equation of polynomial trend line is changed to $y = -0.0002x^2 + 0.1827x + 0.115$, whilst the R-squared value is equal to 0.9567.

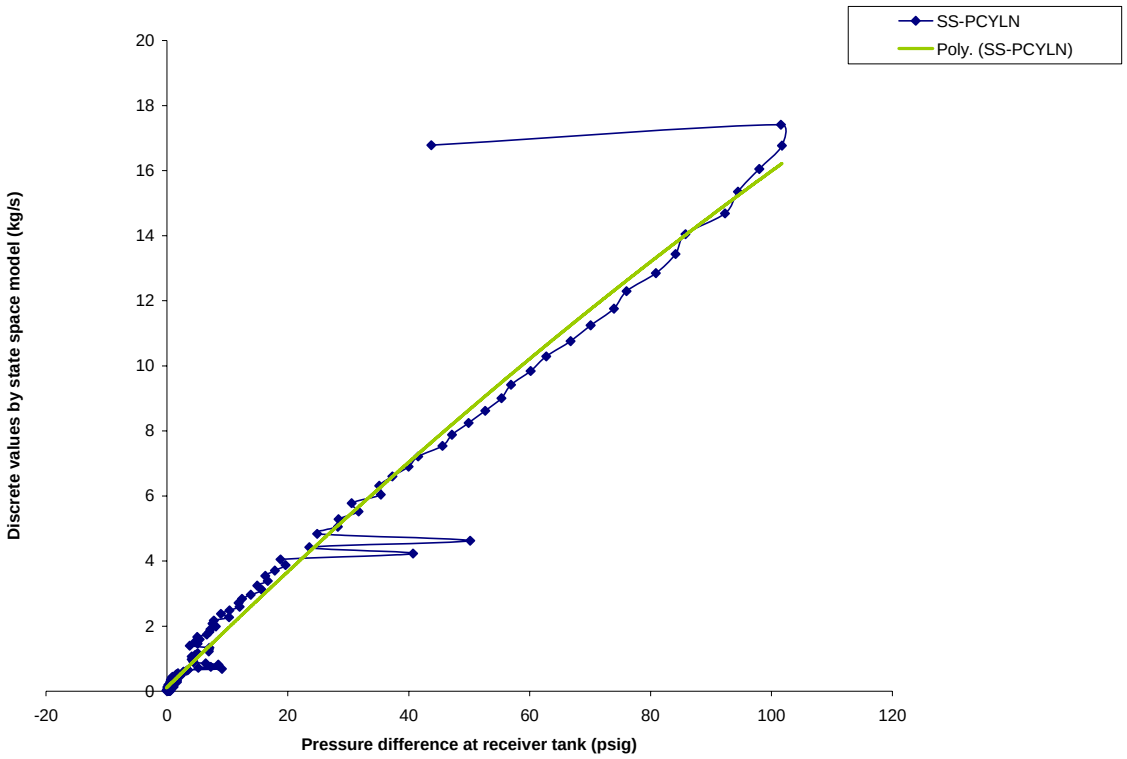

Figure 4.57: Non linear curve for SS-PCLYN using 2nd order polynomial trend line

Table 4.12: R-squared value for 2nd order polynomial trend line

Trend line	Equation	R-squared
Polynomial	$y = -0.0002x^2 + 0.1827x + 0.115$	0.9567

Based on Figure 4.57, both curves overlap when pressure difference is less than 20 psig, and separate when the pressure difference is between 20 to 40 psig, whilst, the major break occurs when the pressure difference is between 40 to 80 psig. The observation shows the polynomial trend line is accurate if pressure difference is less than 20 psig. Further analysis is made by increasing the polynomial trend line to 3rd order.

Figure 4.58 shows a 3rd order polynomial trend line for Figure 4.51. When, the order is increased to 3rd order, the equation of polynomial trend line is changed to $y = 1\times10^{-5}x^3 - 0.0019x^2 + 0.2324x + 0.0137$, whilst the R-squared value has increased to 0.9589.

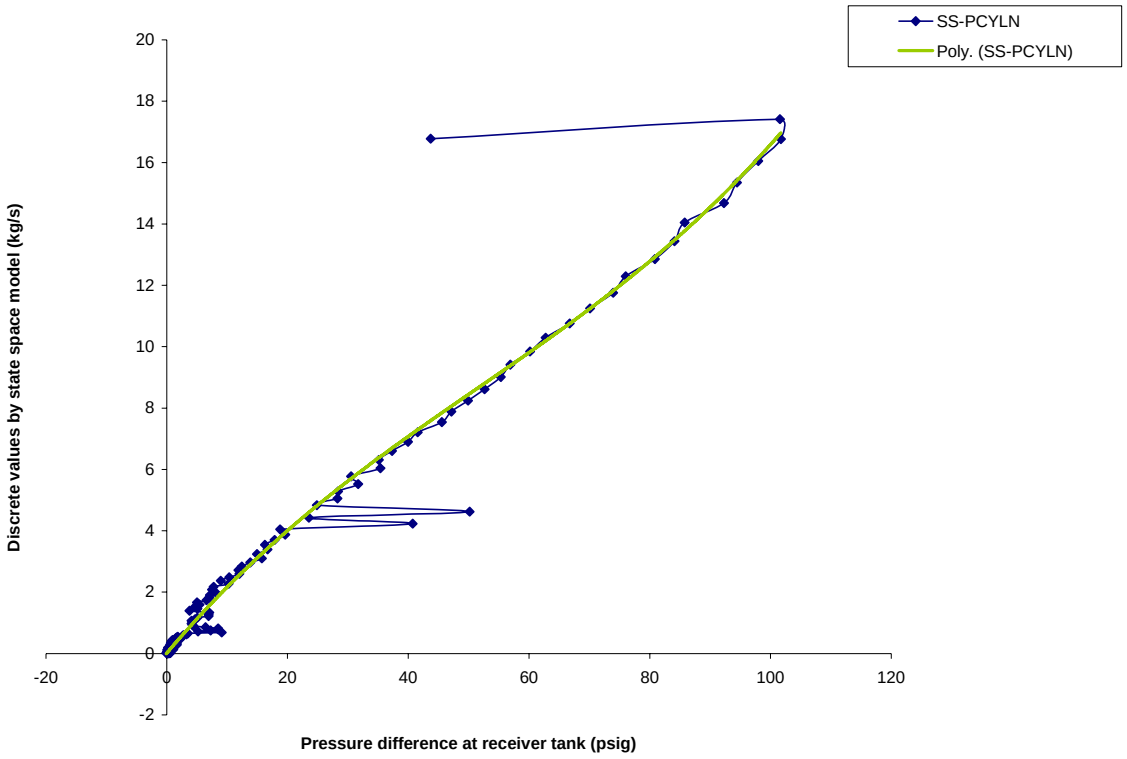

Figure 4.58: Non linear curve for SS-PCLYN using 3rd order polynomial trend line

Table 4.13: R-squared value for 3rd order polynomial trend line

Trend line	Equation	R-squared
Polynomial	$y = 1\times10^{-5}x^3 - 0.0019x^2 + 0.2324x + 0.0137$	0.9589

Based on Figure 4.58, both curves overlap when pressure difference is less than 20 psig, and separate when the pressure difference is between 20 to 40 psig, whilst, no major break occurs when the pressure difference is greater than 40 psig. The observation shows the polynomial trend line is accurate at all range of pressure differences, except at pressure difference 20 to 40 psig. Further analysis is made by increasing the polynomial trend line to 4th order.

Figure 4.59 shows a 4th order polynomial trend line for Figure 4.51. When the order is increased to 4th order, the equation of polynomial trend line is changed to $y = 6\times10^{-8}x^4 + 2\times10^{-6}x^3 + 0.0013x^2 + 0.2235x + 0.0256$, whilst the R-squared value has maintained at 0.9589.

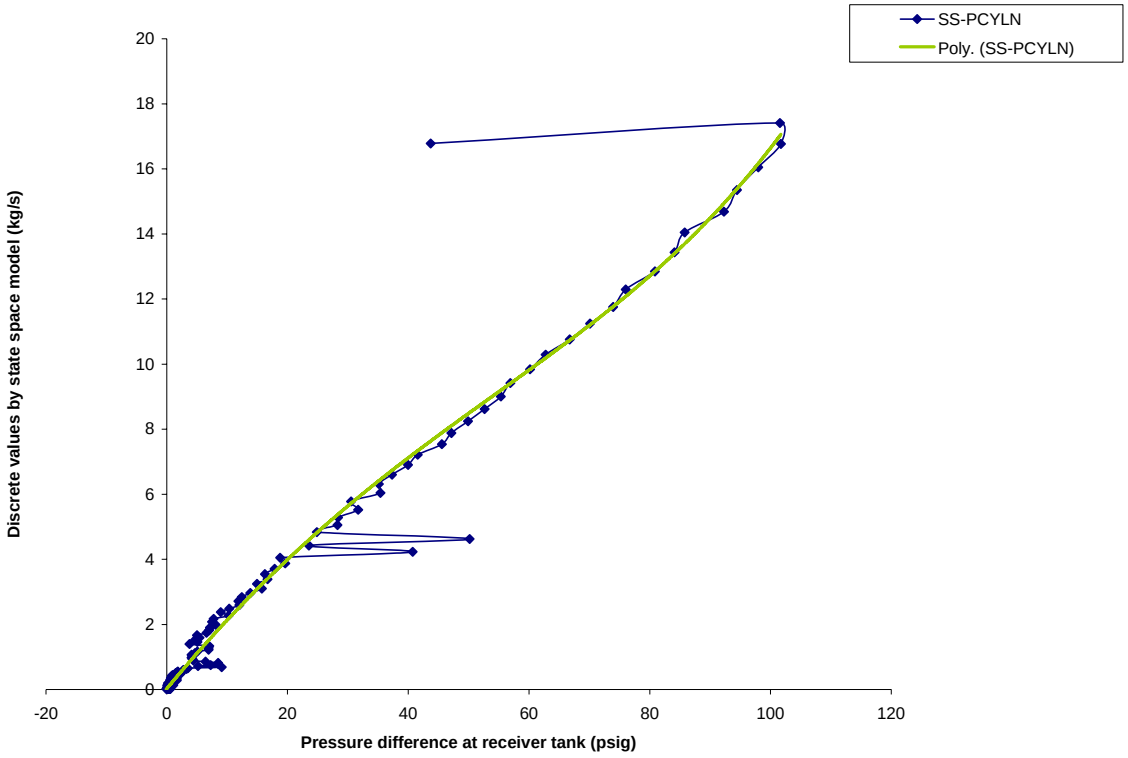

Figure 4.59: Non linear curve for SS-PCLYN using 4th order polynomial trend line

Table 4.14: R-squared value for 4th order polynomial trend line

Trend line	Equation	R-squared
Polynomial	$y = 6\times10^{-8}x^4 + 2\times10^{-6}x^3 + 0.0013x^2 + 0.2235x + 0.0256$	0.9589

Based on Figure 4.59, a similar description as shown in Figure 4.58 could be observed. Since the R-squared has maintained at similar value, the accuracy is similar to 3rd order polynomial trend line. Further observation is made by investigating the polynomial trend line using 5th and 6th order.

Figure 4.60 shows a 5th order polynomial trend line for Figure 4.51. When the order is increased to 5th order, the equation of polynomial trend line is changed to $y = -1\times10^{-9}x^5 + 3\times10^{-7}x^4 - 2\times10^{-5}x^3 - 0.0007x^2 + 0.2181x + 0.0303$, whilst the R-squared value has maintained to 0.9589. It shows the performance is similar as Figure 4.58 although higher order is tested.

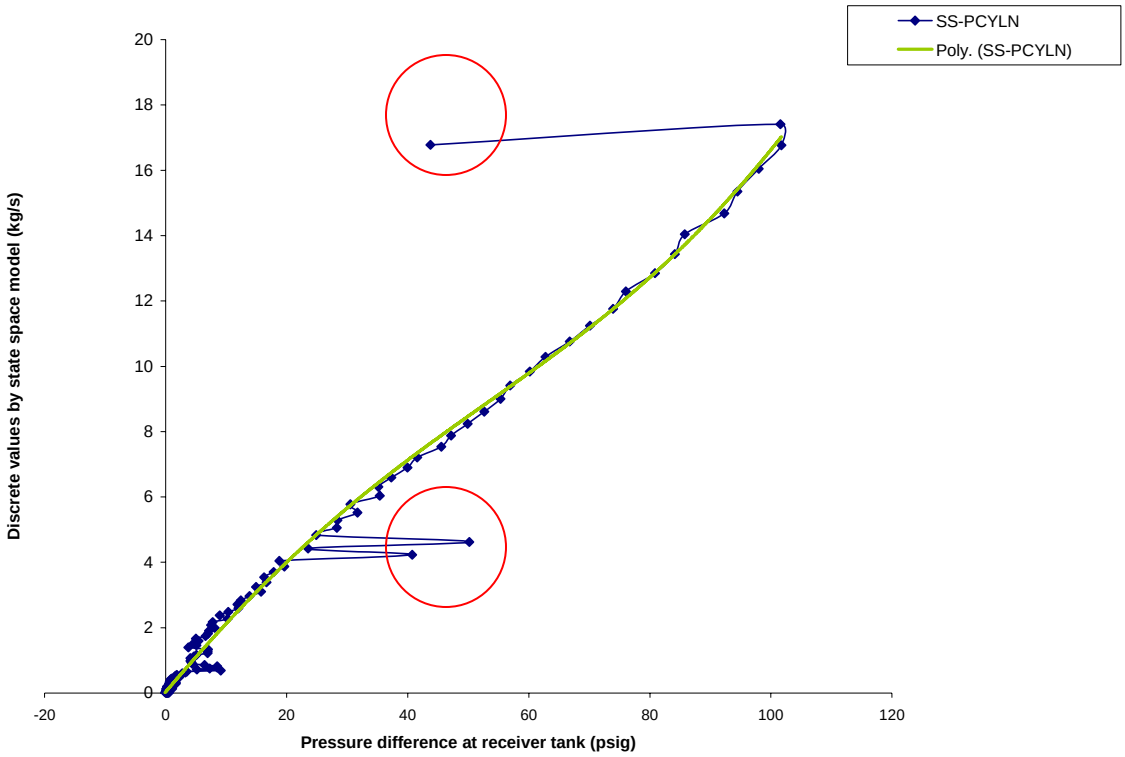

Figure 4.60: Non linear curve for SS-PCLYN using 5th order polynomial trend line

Table 4.15: R-squared value for 5th order polynomial trend line

Trend line	Equation	R-squared
Polynomial	$y = -1\times10^{-9}x^5 + 3\times10^{-7}x^4 - 2\times10^{-5}x^3 - 0.0007x^2 + 0.2181x + 0.0303$	0.9589

From Figure 4.60, there are two red circles shown. The circles are defined as abnormal pulses in the measurement which also appear at similar locations in Figure 4.57-4.59. The phenomenon is defined as an outlier or unexpected events due to temporary sensor failure which could not be removed although higher order is used [30]. Please refer Figure 4.61 for higher order such as the 6th order.

Figure 4.61 shows a 6th order polynomial trend line for Figure 4.51. When the order is increased to 6th order, the equation of polynomial trend line is changed to $y = -3\times10^{-11}x^6 + 8\times10^{-9}x^5 - 7\times10^{-7}x^4 + 3\times10^{-5}x^3 - 0.0017x^2 + 0.2245x + 0.0261$, whilst the R-squared value still maintains at value 0.9589. Notice that, the outlier still occurs although 6th order is used. Since it affects the accuracy of polynomial trend line, the observation shows the outlier must be filtered manually from the sample data. Please refer appendix I for example of Visual Basic program to remove outlier.

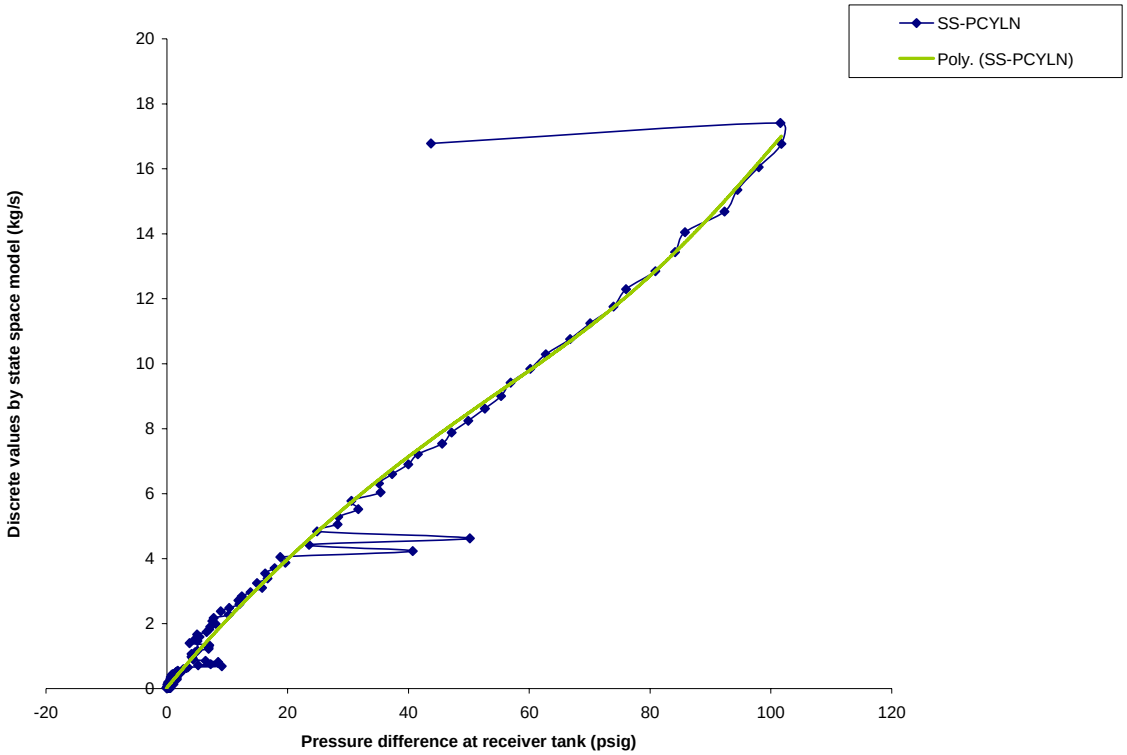

Figure 4.61: Non linear curve for SS-PCLYN using 6th order polynomial trend line

Table 4.16: R-squared value for 6th order polynomial trend line

Trend line	Equation	R-squared
Polynomial	$y = -3\times10^{-11}x^6 + 8\times10^{-9}x^5 - 7\times10^{-7}x^4 + 3\times10^{-5}x^3 - 0.0017x^2 + 0.2245x + 0.0261$	0.9589

In this section, various orders of polynomial trend lines have been investigated from 2nd to 6th order. Based on these order, a table of comparison is made in following section to determine a suitable order for inferential coriolis equation.

4.6.3 Finalizing trend line

Table 4.17 shows table of comparison to determine suitable order for inferential coriolis equation using polynomial trend line in Figure 4.57-4.61, respectively.

Table 4.17: R-squared value for 2nd to 6th order polynomial trend line

Order	Equation	R^2
2	$y = -0.0002x^2 + 0.1827x + 0.115$	0.9567
3	$y = 1\times10^{-5}x^3 - 0.0019x^2 + 0.2324x + 0.0137$	0.9589
4	$y = 6\times10^{-8}x^4 + 2\times10^{-6}x^3 + 0.0013x^2 + 0.2235x + 0.0256$	0.9589
5	$y = -1\times10^{-9}x^5 + 3\times10^{-7}x^4 - 2\times10^{-5}x^3 - 0.0007x^2 + 0.2181x + 0.0303$	0.9589
6	$y = -3\times10^{-11}x^6 + 8\times10^{-9}x^5 - 7\times10^{-7}x^4 + 3\times10^{-5}x^3 - 0.0017x^2 + 0.2245x + 0.0261$	0.9589
AVERAGE		0.9585

When the order increases from 2nd to 3rd order, the R-squared value would also increase from 0.9567 to 0.9589, respectively. The smallest R-squared value is equal to 0.9567 which is represented by 2nd order polynomial trend line, whilst the highest R-squared value is equal to 0.9589 which is represented by 3rd to 6th order polynomial trend lines, respectively. When 3rd order is used, the R-squared value would maintain at value of 0.9589 although higher order is used. This indicates the suitable order for the polynomial trend line is the 3rd order since it has the highest R-squared value with minimum order of coefficients. Whilst, from the average point of view, it shows the R-squared value has improved from 0.9550 (shown in Table 4.11) to 0.9585, if 3rd order is applied.

Section 4.6.2 has been to selecting 3rd order polynomial trend line for representing inferential coriolis equation. In following section, a similar procedure would be applied to determine the final inferential coriolis equation based on five samples of data sets that have been filtered from outlier values. During this work, there are numerous experiments and data sets that have been evaluated which affect final elements of inferential coriolis formula. However, the selected evaluations cases presented here represent the main issue on designing the accurate inferential coriolis equation that relates to the Micro Motion coriolis flowmeter.

Figure 4.62 shows a 3rd order polynomial trend line using the first sample of data sets. It is found that the equation of polynomial trend line is equal to $y = 1\times10^{-5}x^3 - 0.0023x^2 + 0.2592x + 0.1053$, whilst the R-squared value has improved to 0.9946.

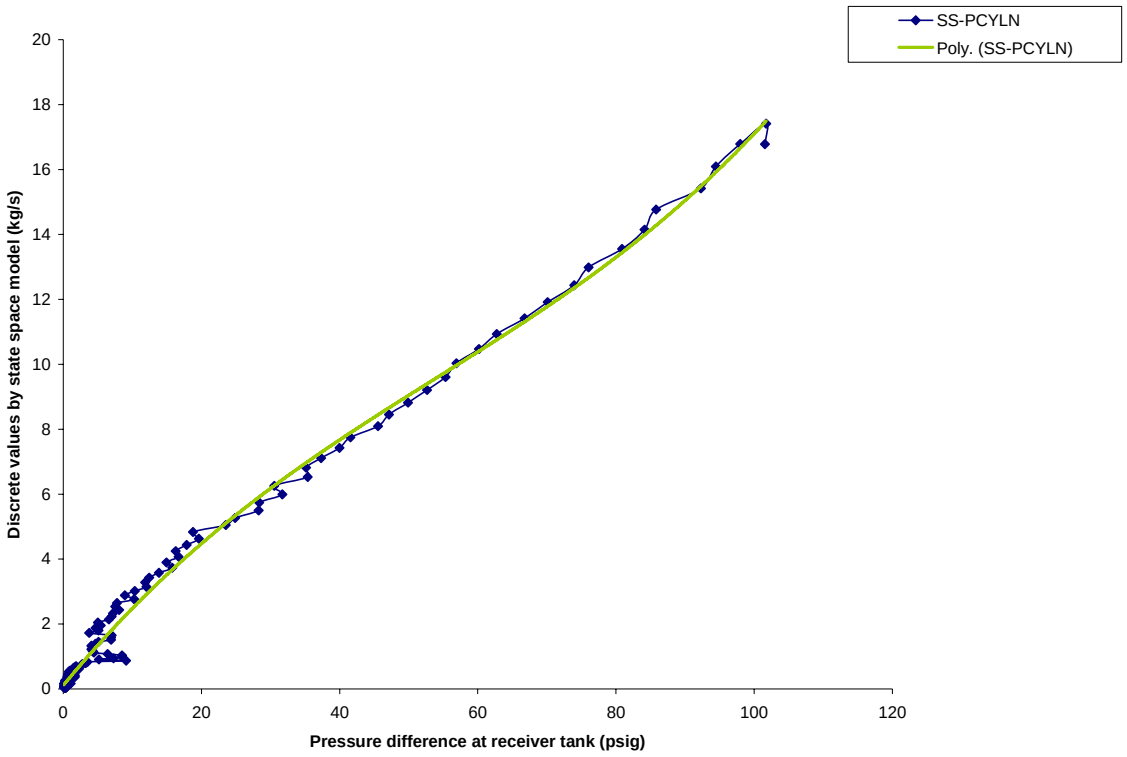

Figure 4.62: 3rd order polynomial trend line for first sample of data sets

Table 4.18: R-squared value of 3rd order polynomial trend line for first sample of data sets

Trend line	Equation	R-squared
Polynomial	$y = 1\times10^{-5}x^3 - 0.0023x^2 + 0.2592x + 0.1053$	0.9946

Based on Figure 4.62, major break occurs when the pressure difference is between 0 to 20 psig, whilst minor breaks occurs when the pressure difference is between 20 to 60 psig. However, both curves overlap each other when the pressure difference is between 60 to 120 psig. Based on this observation, it indicates that the inferential coriolis measurement is applicable if the pressure difference is between 60 to 120 psig. Further analysis is made using the second sample data.

Figure 4.63 shows a 3rd order polynomial trend line using the second sample of data sets. It is found that the equation of polynomial trend line is equal to $y = 1\times10^{-5}x^3 - 0.002x^2 + 0.2629x - 0.0144$, whilst the R-squared value is equal to 0.9714.

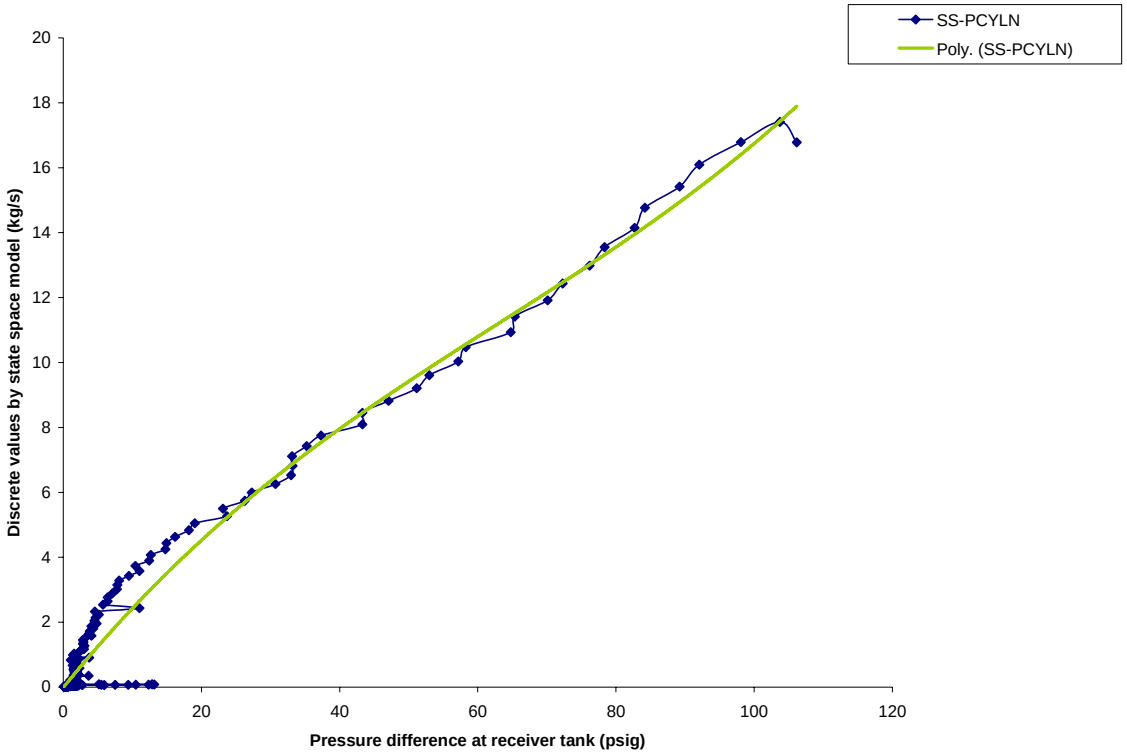

Figure 4.63: 3rd order polynomial trend line for second sample of data sets

Table 4.19: R-squared value of 3rd order polynomial trend line for second sample of data sets

Trend line	Equation	R-squared
Polynomial	$y = 1\times10^{-5}x^3 - 0.002x^2 + 0.2629x - 0.0144$	0.9714

Based on Figure 4.63, major break occurs when the pressure difference is between 0 to 20 psig, whilst minor break occurs when the pressure difference is between 20 to 80 psig. However, major break occurs again when the pressure difference is between 80 to 120 psig. Based on this observation, it indicates that the inferential coriolis measurement is applicable if the pressure difference is between 20 to 80 psig. Further analysis is made using the third sample data.

Figure 4.64 shows a 3rd order polynomial trend line using the third sample of data sets. It is found that the equation of polynomial trend line is equal to $y = 1\times10^{-5}x^3 - 0.0024x^2 + 0.2696x - 0.1372$, whilst the R-squared value has improved to 0.9949.

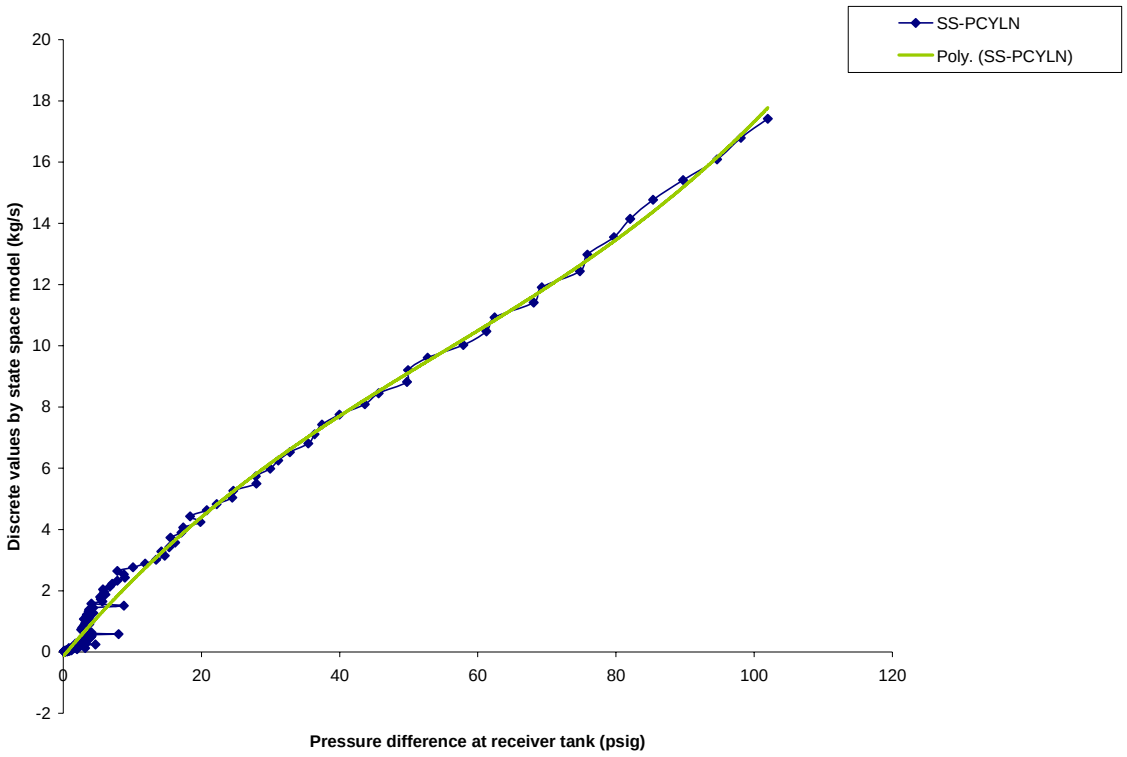

Figure 4.64: 3rd order polynomial trend line for third sample of data sets

Table 4.20: R-squared value of 3rd order polynomial trend line for third sample of data sets

Trend line	Equation	R-squared
Polynomial	$y = 1\times10^{-5}x^3 - 0.0024x^2 + 0.2696x - 0.1372$	0.9949

Based on Figure 4.64, major break occurs when the pressure difference is between 0 to 20 psig, whilst both curves overlap each other when the pressure difference is between 20 to 80 psig. However, only a minor break occurs when the pressure difference is between 80 to 120 psig. Based on this observation, it indicates that the inferential coriolis measurement is applicable if the pressure difference is between 20 to 120 psig. Further analysis is made using the forth sample data.

Figure 4.65 shows a 3rd order polynomial trend line using the forth sample of data sets. It is found that the equation of polynomial trend line is equal to $y = 3\times10^{-5}x^3 - 0.0049x^2 + 0.3746x + 0.365$, whilst the R-squared value is equal to 0.9699.

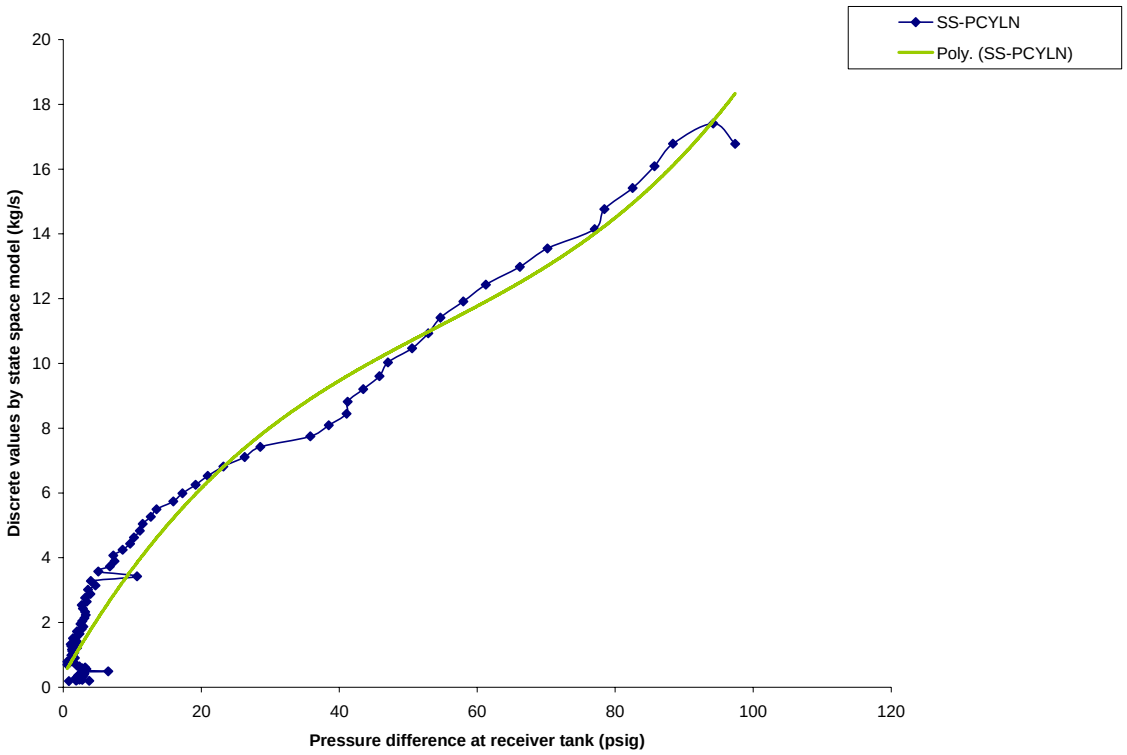

Figure 4.65: 3rd order polynomial trend line for forth sample of data sets

Table 4.21: R-squared value of 3rd order polynomial trend line for forth sample of data sets

Trend line	Equation	R-squared
Polynomial	$y = 1\times10^{-5}x^3 - 0.0024x^2 + 0.2696x - 0.1372$	0.9949

Based on Figure 4.65, major break occurs when the pressure difference is between 0 to 20 psig, 20 to 60 psig, and 60 to 120 psig, respectively. Based on this observation, it indicates that the forth sample of data sets is not applicable for inferential coriolis measurement. Further analysis is made using the fifth sample data.

Figure 4.66 shows a 3rd order polynomial trend line using the fifth sample of data sets. It is found that the equation of polynomial trend line is equal to $y = 3\times10^{-5}x^3 - 0.0043x^2 + 0.3419x - 0.1131$, whilst the R-squared value is equal to 0.9907.

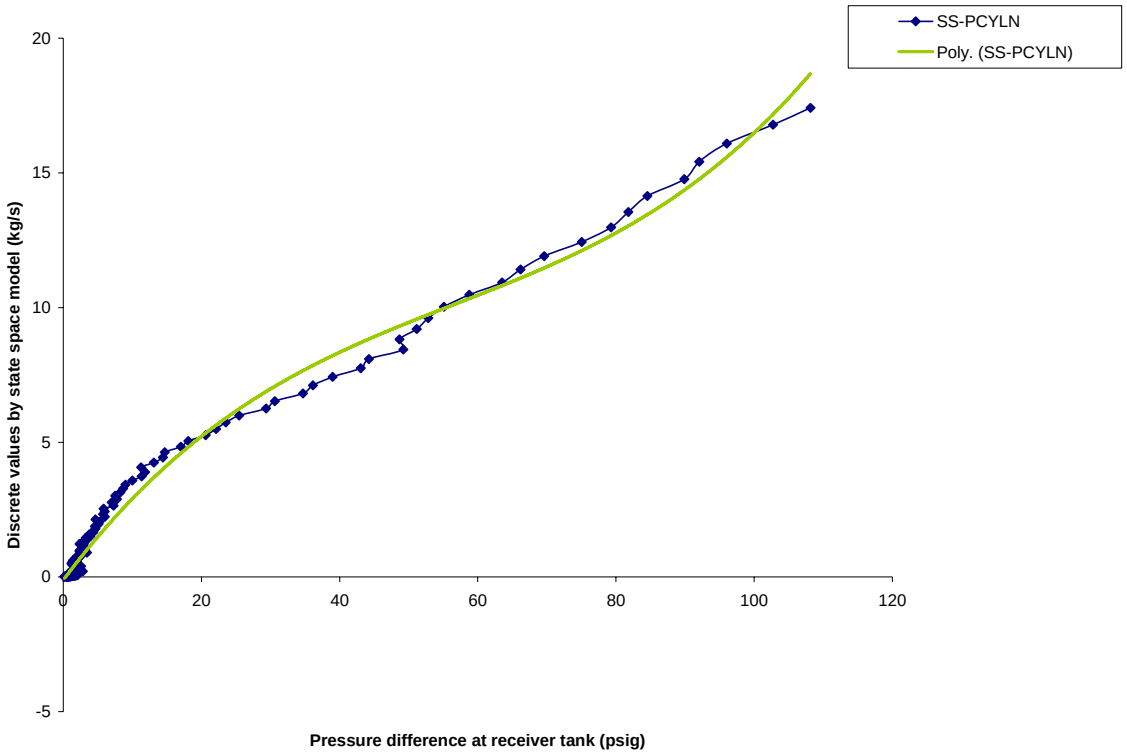

Figure 4.66: 3rd order polynomial trend line for fifth sample of data sets

Table 4.22: R-squared value of 3rd order polynomial trend line for fifth sample of data sets

Trend line	Equation	R-squared
Polynomial	$y = 3\times10^{-5}x^3 - 0.0043x^2 + 0.3419x - 0.1131$	0.9907

Based on figure 4.66, minor break occurs when the pressure difference is between 0 to 20 psig, whilst major break occurs when the pressure difference is between 20 to 60 psig and 60 to 120 psig. Based on this observation, it indicates that the inferential coriolis measurement is applicable if the pressure difference is between 0 to 20 psig. In this section, five sample of data sets have been tested using a 3rd order polynomial trend line, whilst, in following section, the suitable inferential coriolis equation would be chosen.

4.6.4 Implementing trend line

Table 4.23 shows table of comparison to determine the highest R-squared value for 3rd order polynomial trend line discussed in Figure 4.62-4.66, respectively.

Table 4.23: R-squared value using 3rd order polynomial trend line

Sample	Equation	R^2
1	$y = 1\times10^{-5}x^3 - 0.0023x^2 + 0.2592x + 0.1053$	0.9946
2	$y = 1\times10^{-5}x^3 - 0.002x^2 + 0.2629x - 0.0144$	0.9714
3	$y = 1\times10^{-5}x^3 - 0.0024x^2 + 0.2696x - 0.1372$	0.9949
4	$y = 3\times10^{-5}x^3 - 0.0049x^2 + 0.3746x + 0.365$	0.9699
5	$y = 3\times10^{-5}x^3 - 0.0043x^2 + 0.3419x - 0.1131$	0.9907
AVERAGE		0.9843

From Table 4.23, the smallest R-squared value is 0.9699 which is represented by $y = 3\times10^{-5}x^3 - 0.0043x^2 + 0.3419x - 0.1131$, whilst the highest R-squared value is 0.9949 which is represented by $y = 1\times10^{-5}x^3 - 0.0024x^2 + 0.2696x - 0.1372$, respectively. From the average point of view, it shows the R-squared value has improved from 0.9585 (shown in Table 4.17) and 0.9550 (shown in Table 4.11), to 0.9843 if outlier have been filtered from the sample data. Since the highest R-squared value is detected from the third sample, the suitable equation for inferential coriolis is

$$y = 1\times10^{-5}x^3 - 0.0024x^2 + 0.2696x - 0.1372 \qquad (4.56)$$

Based on this equation, a LabVIEW program for inferential coriolis is developed using FieldPoint. Since the third sample has the highest R-squared value, the respective equation is embedded in the FieldPoint and tested on the test rig. Please refer Figure 4.67-4.71 for sample of inferential coriolis programs using polynomial equations shown in Table 4.23.

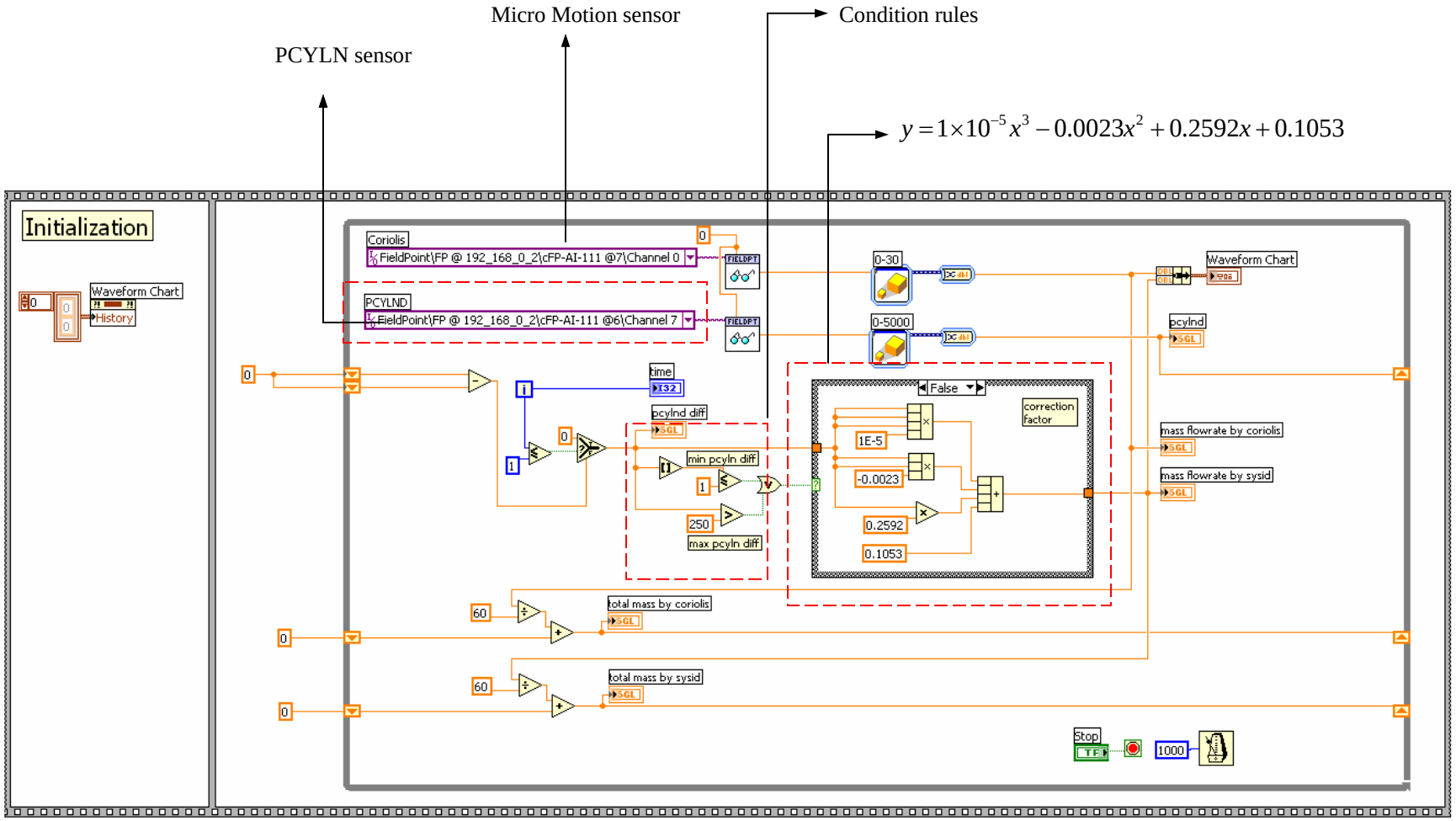

Figure 4.67: Inferential coriolis program based on $y = 1\times10^{-5}x^3 - 0.0023x^2 + 0.2592x + 0.1053$

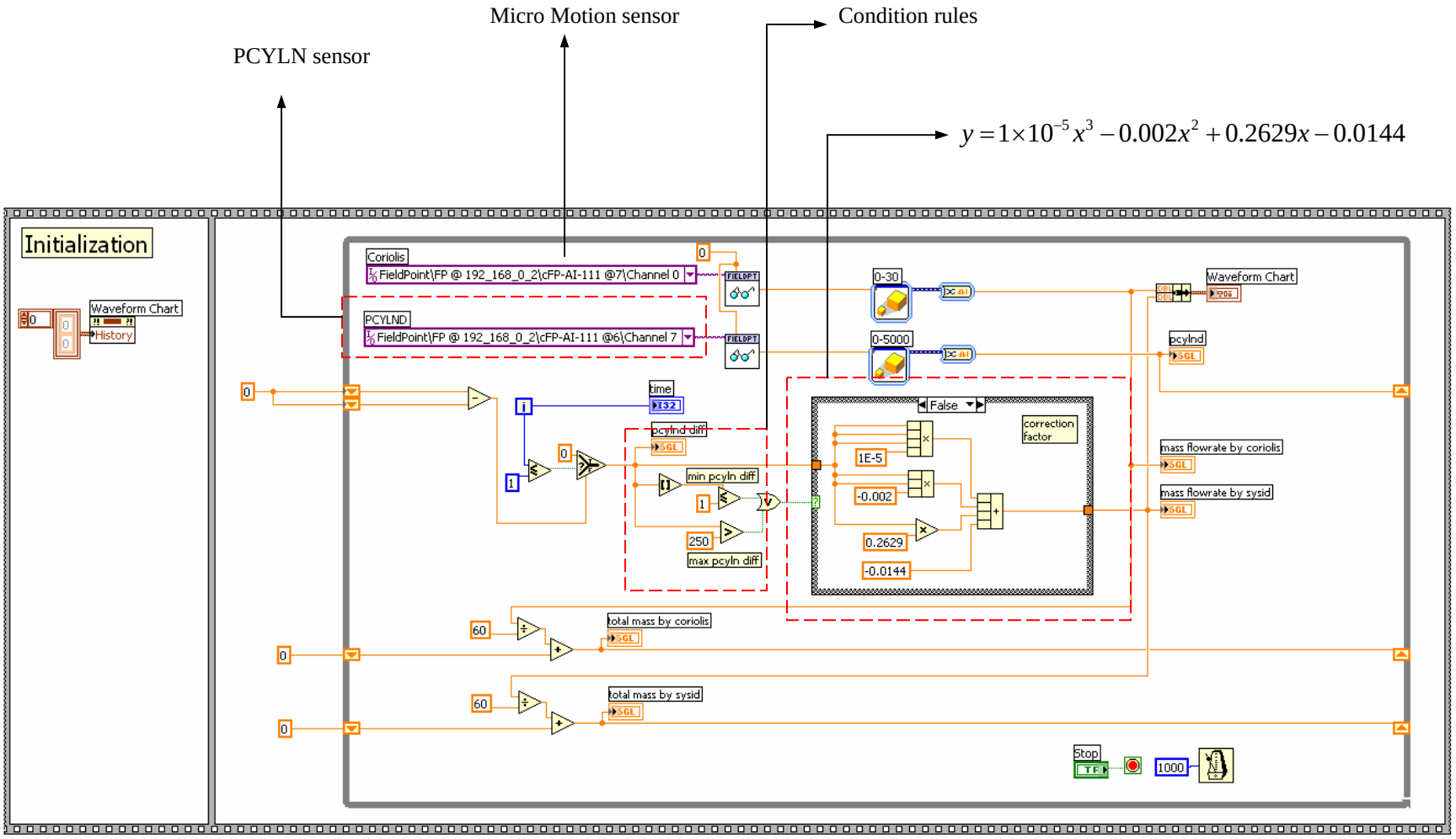

Figure 4.68: Inferential coriolis program based on $y = 1\times10^{-5}x^3 - 0.002x^2 + 0.2629x - 0.0144$

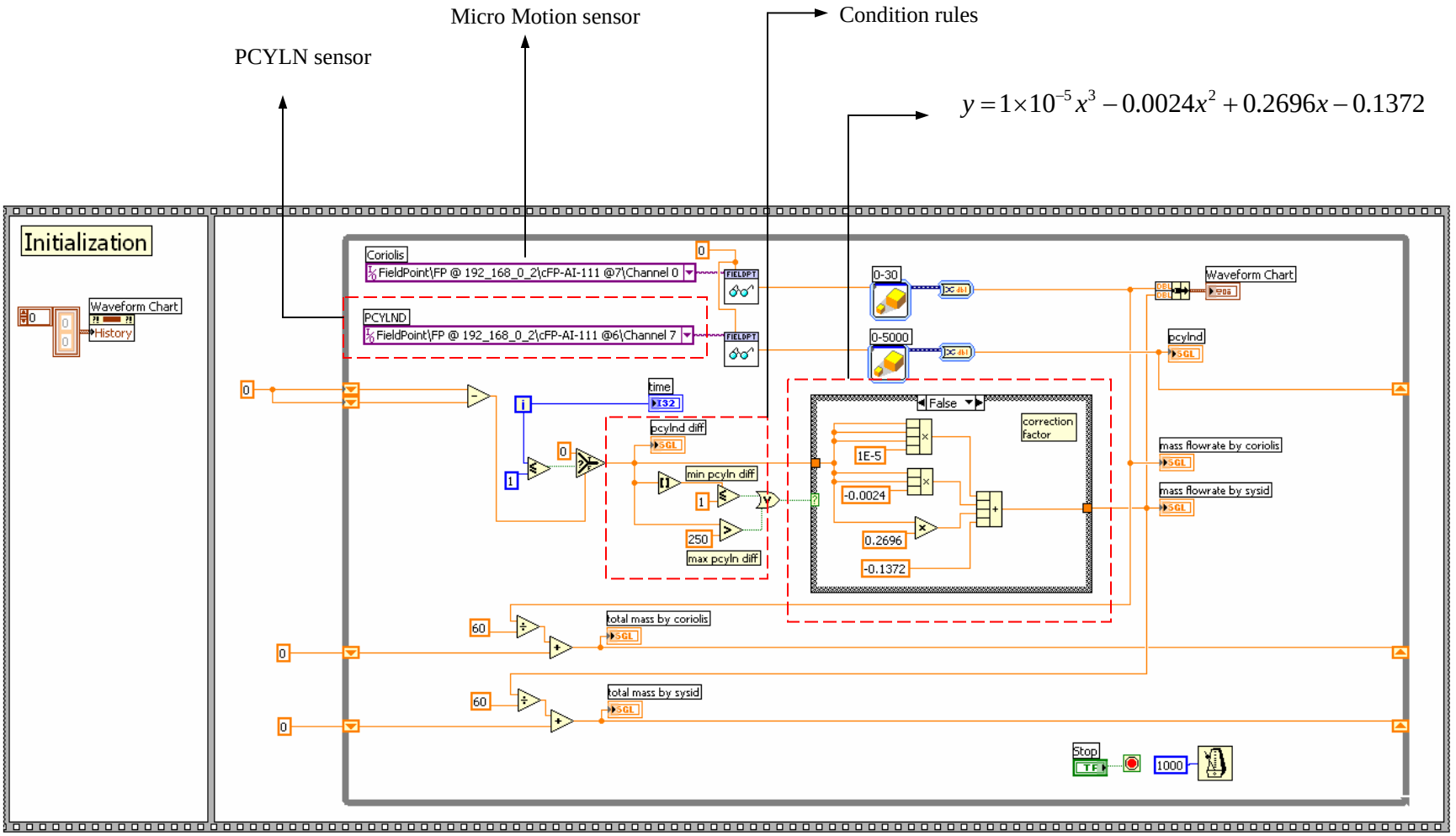

Figure 4.69: Inferential coriolis program based on $y = 1\times10^{-5}x^3 - 0.0024x^2 + 0.2696x - 0.1372$

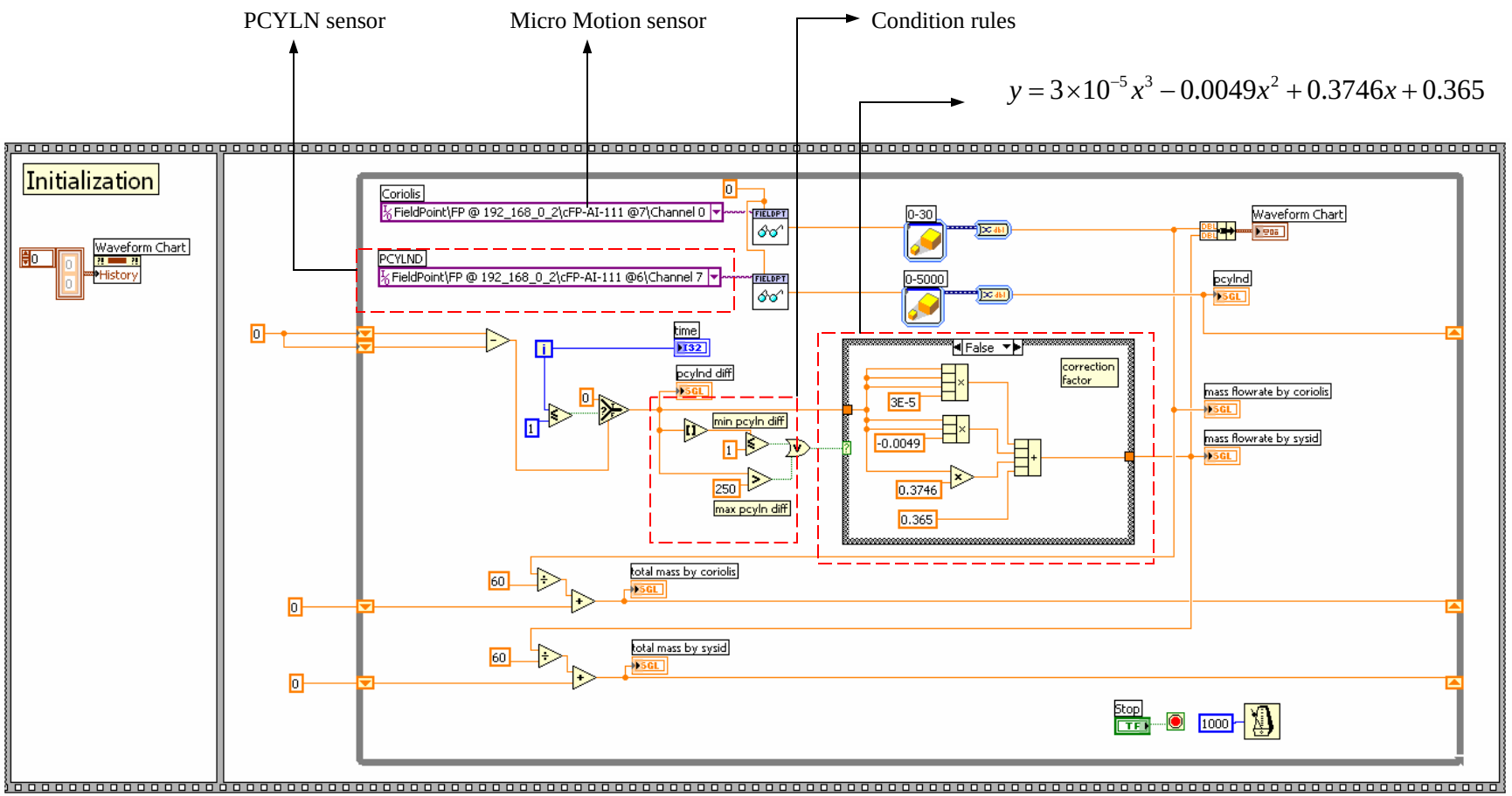

Figure 4.70: Inferential coriolis program based on $y = 3\times10^{-5}x^3 - 0.0049x^2 + 0.3746x + 0.365$

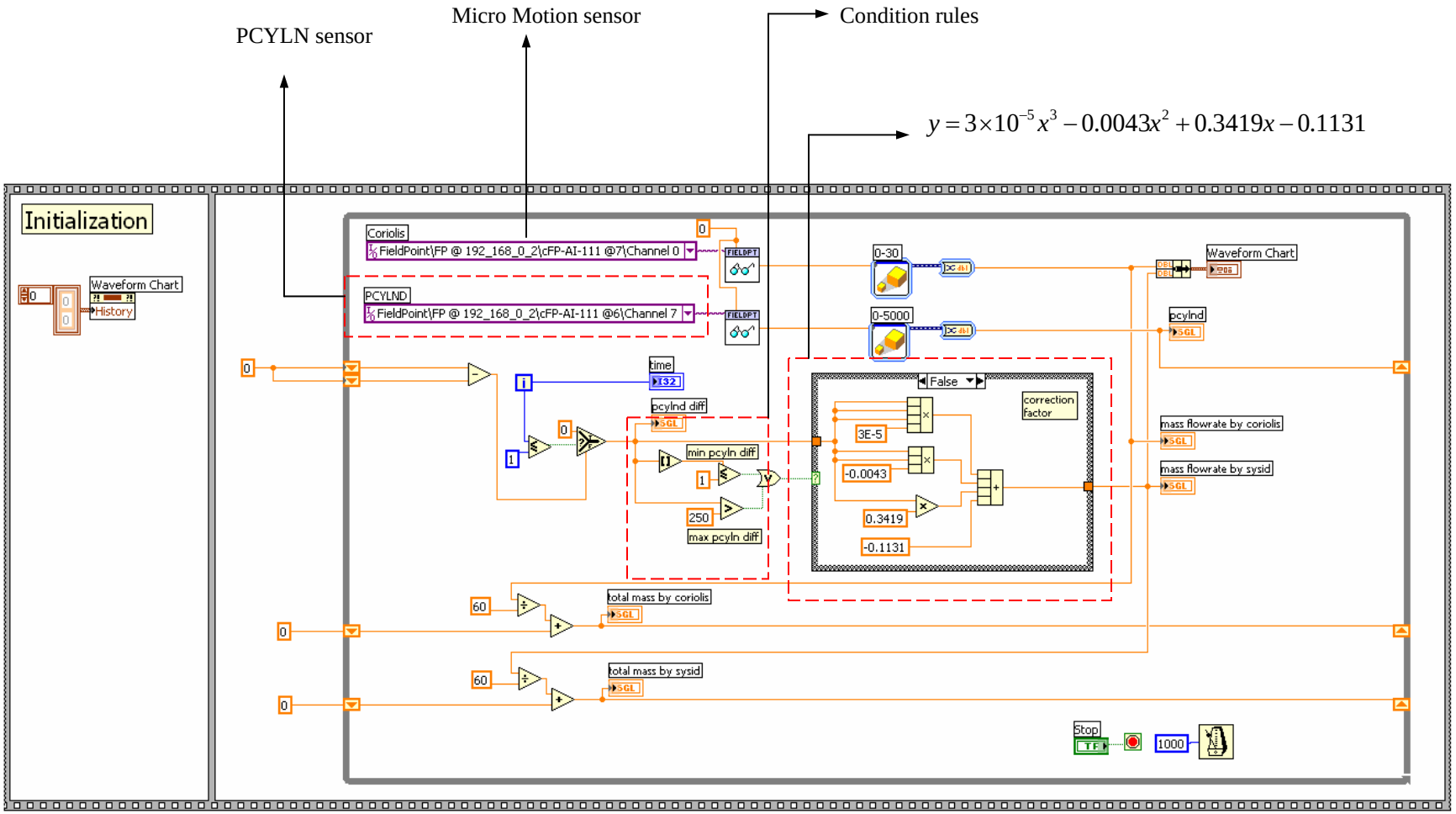

Figure 4.71: Inferential coriolis program based on $y = 3\times10^{-5}x^3 - 0.0043x^2 + 0.3419x - 0.1131$

Figure 4.72 and 4.73 are examples of LabVIEW front panels to display results of mass flowrate measurement from LabVIEW programs shown in Figure 4.67-4.71, respectively. Figure 4.72 shows a typical result for single bank refueling such as the low bank, whilst Figure 4.73 shows a typical result for three banks refueling such as the low bank, medium bank and high bank refueling, respectively. Please refer to Figure 4.24 for details descriptions on single and three banks refueling. Based on Figure 4.72 and 4.73, there are two graphs shown: mass flowrate graph from actual coriolis flowmeter and mass flowrate graph from inferential coriolis, represented in white and red color, respectively. Notice that, the graph developed by inferential coriolis follows the trend developed by actual coriolis although there are outlier occurrences. Based on this observation, some condition rules are added in the inferential coriolis program to filter unexpected occurrence values and to ensure total mass measured by inferential coriolis are within the limit of permissible error. The following section discusses on practical implementation of inferential coriolis using FieldPoint.

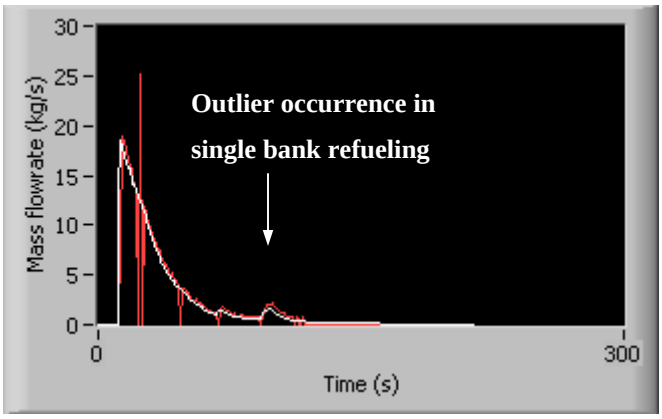

Figure 4.72: Mass flowrate measurement for single bank refueling

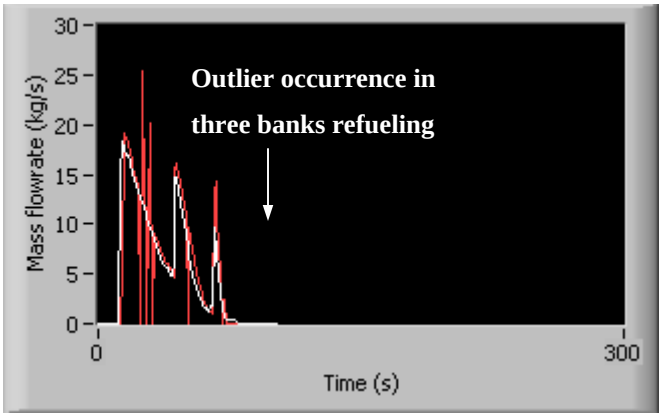

Figure 4.73: Mass flowrate measurement using three banks refueling

4.6.5 Practical implementation

Figure 4.74 is the final prototype for inferential coriolis. Based on Figure 4.74, the prototype could be divided into two parts: pressure sensor and FieldPoint system. The pressure sensor is from Endress-Hauser with pressure rating from 0 to 5000 psig, whilst the FieldPoint is from National Instruments, but is smaller than the one shown in Figure 4.8.

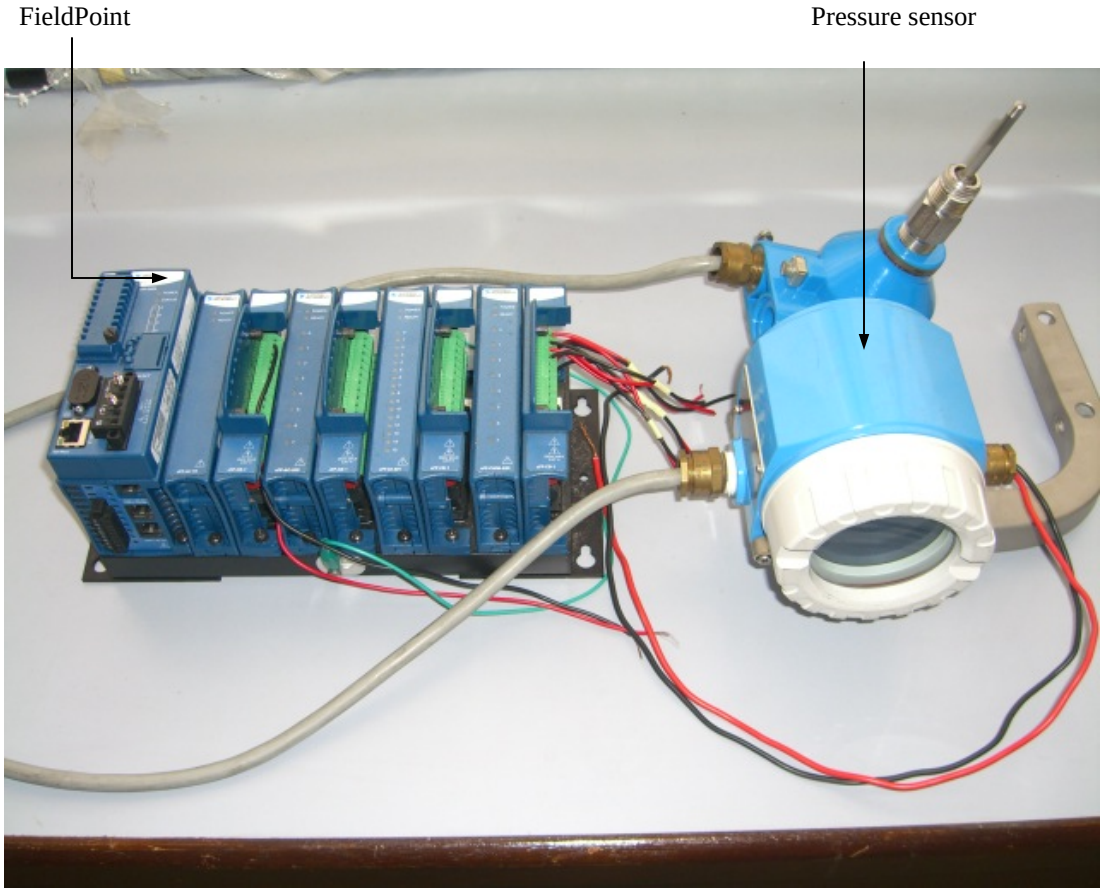

Figure 4.74: Prototype for inferential coriolis

Figure 4.75 are the components for the FieldPoint such as 4 modules backplane, 1 controller module, 8 channels digital input module, 8 channels relay module and 8 channels analog input module. The LabVIEW program developed in Figure 4.69 is the inferential coriolis program embedded in the FieldPoint, whilst the LabVIEW front panels discussed in Figure 4.72-4.73 is the monitoring program to observe the inferential coriolis performance. In this section, prototype of inferential coriolis has been discussed, whilst, in following section, single line diagram for the FieldPoint is presented.

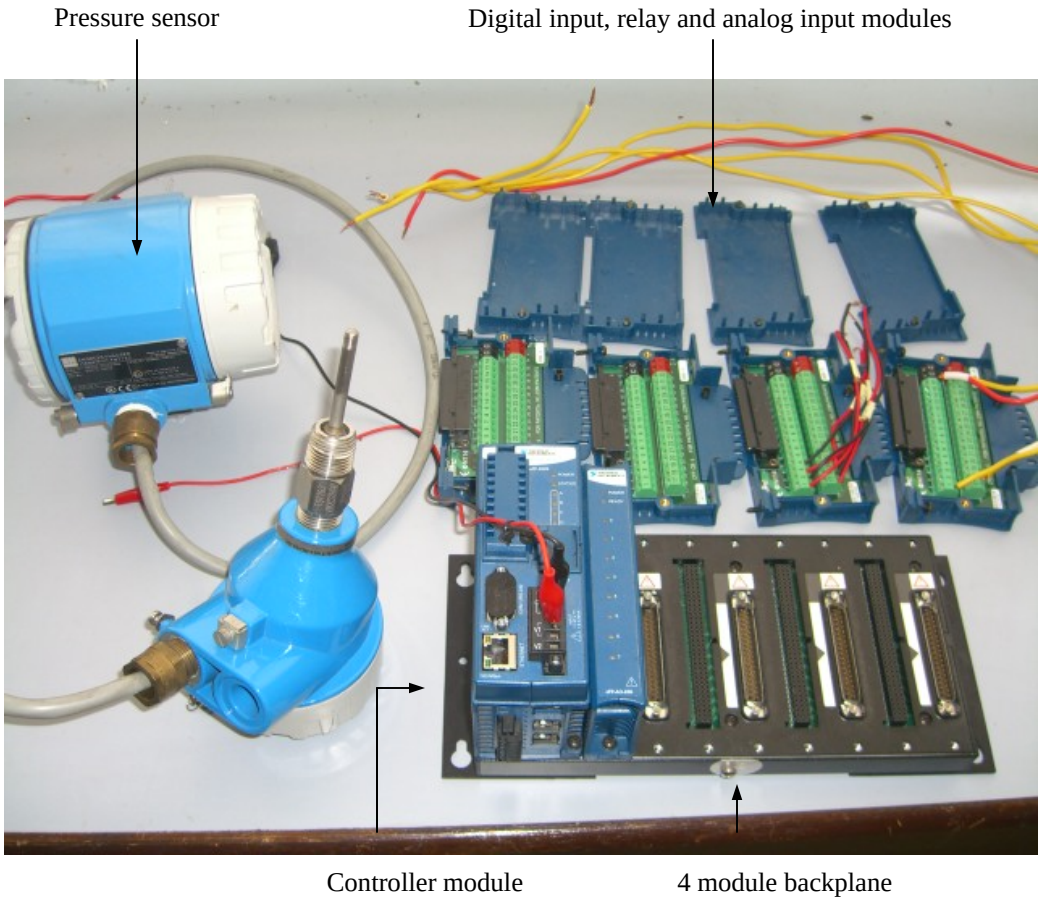

Figure 4.75: Components for inferential coriolis using FieldPoint

Figure 4.76 shows the single line diagram for FieldPoint system shown in Figure 4.75 respectively. Based on the figure, there are three sensors connected to analog input module which are PCYLN (pressure at receiver), coriolis flowmeter (Micro Motion flowmeter) and load cell signals. From the sensors, the mass flowrate from CNG refueling is measured since the total mass accumulated in the receiver tank is the performance measure to be compared with load cell measurement. From the figure also, there are three relay signals connected to relay module which are signals to open and close the solenoid valves for low bank, medium bank and high bank refueling. Different CNG flows and pressures could also be developed by switching the valves automatically, from the low bank to medium bank or high bank source. In this section, single line diagram for the inferential coriolis using FieldPoint has been discussed. The details descriptions on result of performance measure as compared to Micro Motion and load cell is discussed in the next chapter.

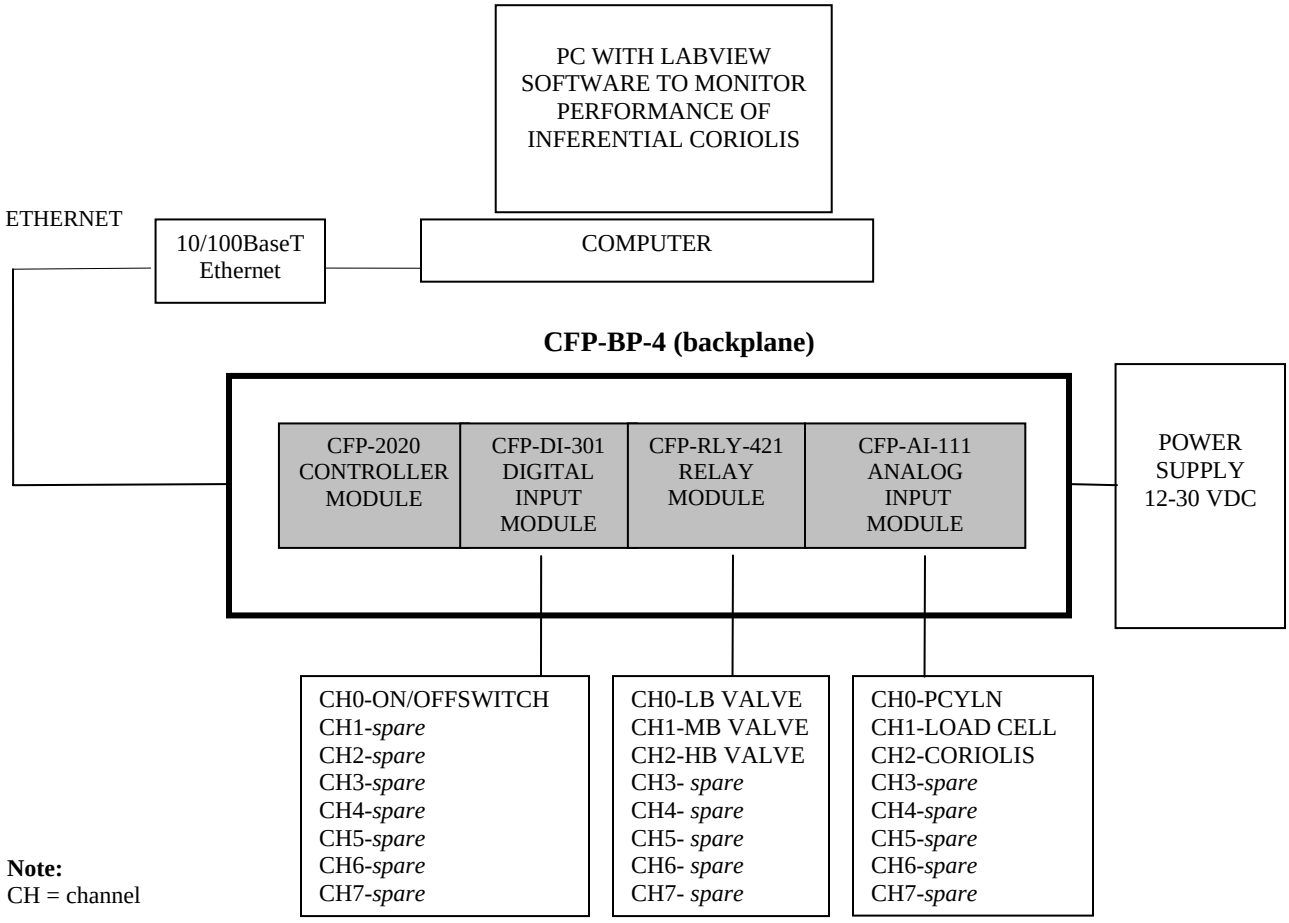

Figure 4.76: Single line diagram for inferential coriolis using FieldPoint

4.7 Summary

An experimental test rig designed for the SYSID modeling of the inferential coriolis includes three main parts: the natural gas test rig, the data acquisition & control system using FieldPoint, and the LabVIEW user interface application. The test rig is designed to be flexible i.e., the experimental data could be collected from various conditions using wide variety of initial pressures as required in the simulations and filling condition of an actual coriolis flowmeter. Since different mathematical theories and algorithms are required for SYSID, LabVIEW program is designed to simulate and analyze each model, where the state-space model is found to provide a realistic representation of (Coriolis Mass Flowrate) CMF system compares to other parametric models. A relationship between power series expansion of the estimated state-space model and the receiver pressure formed the function of the proclaimed inferential coriolis.

The next chapter illustrates with several examples the use of this inferential coriolis to measure the mass flowrate of CNG under different scenarios that are depending on the initial pressure of the receiver tanks, and to compare its performance over the actual coriolis meter manufactured by the Micro Motion.